Summer 2013

Characterization of Microwave Discharge Plasmas for Surface Processing

Milka Nikolic
Old Dominion University

CHARACTERIZATION OF MICROWAVE DISCHARGE PLASMAS FOR SURFACE PROCESSING

by

Milka Nikolić
BSc., University of Belgrade
MS, Old Dominion University

A Dissertation Submitted to the Faculty of
Old Dominion University in Partial Fulfillment of the
Requirements for the Degree of

DOCTOR OF PHILOSOPHY

PHYSICS

OLD DOMINION UNIVERSITY
August 2013

Approved by:

Leposava Vušković (Director)

Charles Sukenik (Member)

Gail Dodge (Member)

Alexander Godunov (Member)

Mileta Tomović (Member)

ABSTRACT

CHARACTERIZATION OF MICROWAVE DISCHARGE PLASMAS FOR SURFACE PROCESSING

Milka Nikolić
Old Dominion University, 2013
Director: Dr. Leposava Vušković

We have developed several diagnostic techniques to characterize two types of microwave (MW) discharge plasmas: a supersonic flowing argon MW discharge maintained in a cylindrical quartz cavity at frequency $f = 2.45$ GHz and a pulse repetitive MW discharge in air at $f = 9.5$ GHz. Low temperature MW discharges have been proven to posses attractive properties for plasma cleaning and etching of niobium surfaces of superconductive radio frequency (SRF) cavities. Plasma based surface modification technologies offer a promising alternative for etching and cleaning of SRF cavities. These technologies are low cost, environmentally friendly and easily controllable, and present a possible alternative to currently used acid based wet technologies, such as buffered chemical polishing (BCP), or electrochemical polishing (EP). In fact, weakly ionized, non-equilibrium, and low temperature gas discharges represent a powerful tool for surface processing due to the strong chemical reactivity of plasma radicals. Therefore, characterizing these discharges by applying non-perturbing, *in situ* measurement techniques is of vital importance.

Optical emission spectroscopy has been employed to analyze the molecular structure and evaluate rotational and vibrational temperatures in these discharges. The internal plasma structure was studied by applying a tomographic numerical method based on the two-dimensional Radon formula. An automated optical measurement system has been developed for reconstruction of local plasma parameters. It was found that excited argon states are concentrated near the tube walls, thus confirming the assumption that the post discharge plasma is dominantly sustained by a travelling surface wave. Employing a laser induced fluorescence technique in combination with the time synchronization device allowed us to obtain time-resolved population densities of some excited atomic levels in argon.

We have developed a technique for absolute measurements of electron density based

on the time-resolved absolute intensity of a Nitrogen spectral band belonging to the Second Positive System, the kinetic model and the detailed particle balance of the N_2 ($C^3\Pi_u$) state. Measured electron density waveforms are in fair agreement with electron densities obtained using the Stark broadening technique. In addition, time dependent population densities of Ar I metastable and resonant levels were obtained by employing a kinetic model developed based on analysis of population density rates of excited Ar I p levels. Both the experimental results and numerical models for both types of gas discharges indicate that multispecies chemistry of gases plays an important role in understanding the dynamics and characterizing the properties of these discharges.

ACKNOWLEDGMENTS

I would like to begin by thanking my advisor, Dr. Leposava Vušković for her patience, guidance, and support throughout my research. Her never ending enthusiasm and immense knowledge about physics inspired my work and helped me learn and grow. I would also like to thank Dr. Svetozar Popović for his guidance and invaluable input about every problem I had while working on this thesis. Thank you both for being great mentors and most of all friends for all these years.

I would like to express my sincere gratitude to Dr. Charles Sukenik and Dr. Alex Godunov, whose depth of knowledge never ceases to amaze me, for providing me with an opportunity to expand my research experience in both experimental and theoretical work. To the staff, faculty and graduate students at the department of physics at ODU, thank you for your support, encouragement and all the laughs for the last six years. I especially want to thank my lab mate Janardan Upadhyay, who as a good friend, was always willing to help and give his best suggestions making our lab a great place to work.

To my parents, my brother and my friends in Serbia, I want to thank you for your encouragement and support throughout this whole experience. I would especially like to thank my flat mates Filip, Mladen, Miloš, Ivan, Marija, and Nenad for creating great living atmosphere and for making me feel at home. Most importantly I want to thank Ana Samolov for being there for me as a fellow class mate, a colleague and above all a true friend for more than ten years.

I would like to acknowledge financial support received from Jefferson Laboratory through Graduate Student Research Assistantship [1]. The research was inspired and supported by the Office of the High Energy Physics, Office of Science, Department of Energy under Grant No. DE-SC0007879.

[1]Jefferson Laboratory is operated by Jefferson Science Associates under DOE No. Contract No. DE-AC05-06OR23177.

TABLE OF CONTENTS

LIST OF TABLES

LIST OF FIGURES

CHAPTER 1

INTRODUCTION

Over the last decade, there has been a growing interest in low temperature, non-equilibrium gas discharge plasmas for the processing of surfaces. Indeed, up until recent times much more attention has been directed toward thermonuclear fusion and space plasmas. This is understandable since space plasmas represent the dominant state in the whole visible universe (more than 99.99%). Our Sun, together with all the stars, plus interplanetary, interstellar, and intergalactic medium are in the plasma state. On the other hand, laboratory made fusion plasmas share a very important characteristics with space plasmas, both are hot plasmas in thermal equilibrium. This placed fusion plasmas to be a great candidate for a fusion fuel source on Earth. Most of the 20th century plasma research was dedicated to exploring a controlled thermo-nuclear fusion and new sources of energy [1].

However, the 21st century's need for environmentally friendly "green" technologies has brought the attention back to non-equilibrium, cold plasmas. Moreover, with the development of the semiconductor industry, non-equilibrium plasma processing using gas discharges has become an essential part of modern technology. There are many important applications of non-equilibrium gas discharges in the processing of semiconductors [2–5]. These include various film deposition technologies, such as sputtering and plasma enhanced chemical vapor deposition and film removal technologies, such as etching and cleaning. The main advantage of gas discharges comes from the fact that non-equilibrium is a consequence of strong chemical reactivity of plasma particles, meaning that weakly ionized gas discharges represent a powerful tool for surface processing. In addition, the use of plasma processing avoids chemical disposal problems associated with the acid-based wet processing technologies, such as buffered chemical polishing (BCP), or electrochemical polishing (EP).

It has been confirmed that low pressure, high density plasma sources generated using radio-frequency (RF) or microwave (MW) powers show the most attractive properties for plasma etching and cleaning purposes [6,7]. Particularly, MW discharge plasmas allow work at higher pressures and give higher plasma densities. Often, in order to obtain optimal plasma etching and cleaning, gas discharges consisting of a

combination of inert gases (argon) and reactive gases (chlorine) are used. Although, MW discharge plasmas are widely used, the knowledge of fundamental physical and chemical phenomena which determine the outcome of the plasma surface interactions is still mostly empirical. Therefore, research studies in the area of plasma surface interactions, plasma diagnostics and plasma modelling are greatly needed.

The first step in understanding surface modification processes is developing a kinetic model for all plasma particles (electrons, atoms/molecules, ions). This includes knowledge of the electron energy distribution function (EEDF) and reaction rates in various plasma reactions. There have been a number of approaches for plasma internal dynamics studies [6,8,9], especially in the case of Ar plasmas [10–13]. Nevertheless, this is still a widely researched field since there are still issues to be addressed.

Commonly used diagnostic methods, such as the Langmuir probe method, may not be applicable for the diagnostics of MW discharge plasmas because a metal object in the MW cavity affects field distribution and shifts resonant frequency. Therefore, most of the time it is necessary to apply non-intrusive, *in situ* spectroscopic techniques. Optical emission spectroscopy (OES) represents a natural choice due to its simplicity. It allows direct and indirect measurements of fundamental plasma parameters, such as densities, temperatures, population densities, etc. However, population densities of some excited atomic levels can not be determined using OES, so laser diagnostics, such as laser induced fluorescence (LIF), can also be employed. Moreover, applying LIF increases the overall precision of data collection.

Typical optical diagnostics on plasma discharges provides time averaged measurements at particular spatial points. While time averaged measurements of plasma parameters are adequate in determining the overall performance of these parameters, they can not resolve the full plasma dynamics. A time resolved plasma diagnostic is, therefore, desired for better understanding plasma properties. Furthermore, experimental, non intrusive, optical techniques available for plasma characterization allow us to measure only integrated effects of collective plasma behavior. In order to look into the internal dynamics of the discharge, the integrated data needs to be transformed into the spatial population distributions. A commonly used method for reconstructing an inner plasma structure is the Abel inversion, which requires the plasma to be axially symmetric [14]. As a rule, most plasmas of interest are non-stationary, inhomogeneous, and with strong radial and axial asymmetry. It follows that the discharge should be observed from at least two angles of observation. The

plasma tomography technique based on an inverse Radon transform is an excellent way to acquire insight into the internal plasma structure [15]. In previous years, extensive studies were conducted on the simplified case, where only two mutually perpendicular directions were used for tomography measurements [16, 17]. This approximation includes only the first two terms in the Fourier transform of the Radon integral, making it difficult to depict the entire angular distribution of plasma parameters. Therefore, a two dimensional plasma tomography based on the numerical solution of the inverse Radon transform integral is necessary for the complete description of the internal plasma structure.

In this work we have focused on two types of low temperature, non-equilibrium MW gas discharge plasmas: a supersonic flowing argon MW discharge maintained in a cylindrical quartz cavity at frequency $f = 2.45$ GHz and a pulse repetitive MW discharge in air at $f = 9.5$ GHz. In order to fully characterize these discharges we have developed kinetic models for all particles in the discharge (electrons, atoms, molecules and ions) and obtained important plasma parameters. Plasma parameters obtained in this research that are crucial for plasma diagnostics are: gas densities and temperatures, electron densities and temperatures, excitation temperatures, rotational and vibrational temperatures, and population densities of excited atoms and molecules. In addition, we have developed several diagnostic techniques (laser induced fluorescence and plasma tomography) to describe the desired parameters in both time and space.

This dissertation is organized as follows. Chapter 1 provides a brief introduction to the presented work, including the motivation for the project. Chapter 2 discusses theoretical principles of plasma physics, including characteristics of plasma parameters in gas discharges and fundamental plasma equations. An overview of existing models for electron energy distribution functions and associate electron transport coefficients is given along with mutual comparison of the models. Chapter 3 presents several experimental set-ups and measurement techniques used in the study. Two types of plasmas are described, atomic argon discharge and molecular air discharge. Chapter 4 describes diagnostic methods applied in the study required for time and space resolved measurements. Chapter 5 gives the results of the measurements of plasma parameters for both types of plasmas. Finally, chapter 6 provides conclusions and suggestions for future work.

CHAPTER 2

BASIC CONCEPTS OF PLASMA PHYSICS

The concept of plasma was first introduced by Irvin Langmuir back in early 1900s. The word "plasma" was coined from a Greek word for "mold", to depict the property of ionized gas (mostly positive column) to follow the shape of the vessel where it was generated. The term plasma was used to define the state of matter containing a significant number of electrically charged particles, sufficient to affect its electromagnetic properties. For that reason plasma has a reputation as a very complex system where collective effects between particles have a dominant role. Plasma particles interact with each other not only through collisions, but by long range electric and magnetic fields. This way the fields are modified by the plasma itself and plasma particles move to shield one another from imposed electric fields.

Although plasma is generally defined as an ionized gas, with the ionization degree ranging from 1 (fully ionized gas) to $10^{-4} - 10^{-6}$ (partially ionized gas), different groups of plasmas are distinguished depending on their origin and their properties. Based on their origin, we differentiate plasmas that can occur naturally in space from plasmas that are generated in laboratories. These laboratory plasmas can, further, divide into high-temperature or fusion plasmas, and low-temperature or gas discharges [6].

In addition, plasmas are classified as to whether they are in thermal equilibrium (TE) or not. Thermal equilibrium means that all plasma species (electrons, ions, and neutral particles) have the same temperature [18]. It is achieved by thermal heating of the plasma species, meaning that substantially high temperatures are required to form these equilibrium plasmas (more than 10000 K). Naturally, it follows that a large number of laboratory plasmas satisfy the TE condition.

Often, only localized regions of plasma satisfy the TE condition, and it is said that plasma is in local thermodynamic equilibrium (LTE). This means that the temperatures of all plasma particles are the same only in confined plasma volumes. If temperatures of plasma species are different everywhere, we have non-equilibrium plasmas, also known as "non-LTE" plasmas. In these plasmas the electrons, having

lower mass, accelerate easily and gain much higher kinetic energy than heavy, slow moving particles (ions and neutrals).

The classification, to LTE and non-LTE plasmas is also valid when describing low-temperature, gas discharges. Moreover, in the case of gas discharges, the equilibrium conditions are related to the working pressure of the plasma [19]. At high pressure, the number of collisions between particles increases, followed by the rise of their energy exchange. Efficient exchange of energy may lead to equilibrium states. At low pressure, there are fewer number of collisions and the energy transfer is less efficient. Consequently, the electron temperatures may reach several thousand Kelvins while heavy particles have temperatures similar to room temperature. There are "hot" electrons that collide with plasma species and are capable of exciting and ionizing atoms and molecules, generating in that way new electrons necessary to sustain plasma system and producing a chemically-rich environment. As a consequence, non-equilibrium gas discharges have a particular use in the plasma processing industry for applications to plasma cleaning and etching, or to the deposition of thin film layers. Hence, characterizing these discharges (i.e. describing the conditions for their generation, estimating parameters for optimal use, etc.) is of vital importance.

Low pressure discharges are characterized by electron temperatures $T_e \approx 1 - 10$ eV, ion temperatures $T_i \approx 300$ K $\ll T_e$, and electron densities $n_e \approx 10^8 - 10^{13}$ cm^{-3}. The gas pressure ranges from $p \approx 1$ mTorr to $p \approx 1$ Torr. Note, that high pressure discharges, such as arc discharge, can also be applied for surface modification to deliver heat to the system or to increase the surface reaction rates. Their electron temperatures are $T_e \approx 0.1 - 2$ eV, ion temperatures $T_i \leqslant T_e$, electron densities $n_e \approx 10^{14} - 10^{19}$ cm^{-3}, and operating pressure is usually near atmospheric pressure.

Based on this wide parameter range, a large variation of gas discharge plasmas can be employed as a tool for plasma processing. We will give a brief overview of the three commonly used types of plasmas, direct current glow discharges, capacitively coupled (CC) radio-frequency (RF), and microwave (MW) and RF induced plasmas.

The main objective of this study is to provide the complete analysis of the low temperature gas discharges. This includes determining conditions for sustaining these plasmas, providing theoretical background, and obtaining parameters, such as electron temperature and density, gas temperature and density, population densities of excited atoms and molecules, etc. which are all necessary in order to successfully apply these plasmas in the surface modification industry.

2.1 PLASMA PARAMETERS IN GAS DISCHARGES

Various plasma processes are used for surface modification of low temperature gas discharges. We will look into three most commonly employed.

a) Deposition of thin films [5]

- Sputter deposition consists of physical sputtering and chemical sputtering. In physical sputtering heavy plasma particles bombard a target and release atoms from the target material, which further, are deposited at a desired substrate. Chemical sputtering occurs when reactive gases are involved. In addition, physical sputtering atoms/molecules of the reactive gas also react with the target, meaning that the substrate will contain the material and the reactive gas substances.
- Plasma enhanced chemical vapor deposition (PE-CVD) is a consequence of the chemical reactions involving reactive gas species in the gas discharge. New plasma species (ions, radicals,...) produced in these reactions diffuse toward the substrate and are deposited by surface chemical reactions.

b) Plasma etching is a process where material is removed from the surface [3,4]. It is characterized with three properties: uniformity, anisotropy (material is removed only in vertical direction), and selectivity (only a specific type of material is removed). Designing plasma that satisfies the desired properties represents a great challenge to researchers. In most cases, one quality needs to be sacrificed in order to achieve the optimal plasma etching. During the etching process we distinguish four mechanisms: sputter etching, chemical etching, ion-enhanced energetic etching, and ion-enhanced inhibitor etching.

- Sputter etching mechanism is equivalent to the sputter deposition with the difference that material is removed from the surface instead deposited to it. This is a non-selective and anisotropic process that highly depends on an angle of incidence of the bombarding ions. Inert gases (Ar, He,...) are often used for sputter etching, which is often called "the physical etching."
- Chemical etching happens in discharges containing reactive gases. Reactive species (atoms, ions, radicals) chemically react with the surface of the target producing new molecules in the gas phase that are volatile under plasma conditions and free to leave the surface. The chemical etching is non-selective

and mostly isotropic process because the etching atoms arrive at the target surface with a nearly uniform angular distribution. The exceptions are reactions between etching atoms and crystals, where crystallographic orientation determines the etching rate.

- Ion-enhanced energetic etching arises when the combination of inert and reactive gases is used for etching purposes. Energetic ions determine the etching rate by bombarding the target surface, but reactive particles are probably responsible for etching chemically. In that way, the etching can be controlled by the inert gas properties (angle of incidence, pressure, temperature, ...) without an additional damage to the surface due to sputtering.
- Ion-enhanced inhibitor etching provides not only an anisotropy and increased etching rate by mixing the energetic and reactive gases but also a great selectivity by adding a protective layer of so-called inhibitor precursor molecules to the target material. Etching atoms will react only with the selected areas of the target which are not covered with the protective layer.

c) Plasma cleaning presents an alternative to conventional chemical (wet) cleaning where all the contaminants can be completely removed from the system. In the case of organic materials, plasma cleaning utilizes an oxidizing gas to convert the surface contaminants into volatile oxides that can be removed from the system. The removal of metallic surface contaminants requires two steps. First, metal is converted into metal complex, which is then volatilized by increasing the substrate temperature and reducing the pressure. Often, chlorine-based plasmas are used for plasma cleaning of metallic surfaces because chlorine reacts with nearly all contaminating metals.

An ongoing experiment in the Atomic and Plasma Physics Lab at the Department of Physics, Old Dominion University is focused on sustaining the ion-enhanced etching and studying its consequences. For that reason, we will describe, in the following subsections, different gas discharges suitable for obtaining ion-enhanced energetic etching. Moreover, in this study we provide a detailed description of the applied gas discharges. In particular, we focus on internal plasma dynamics and discuss different spectroscopic methods to characterize these discharges.

2.1.1 DIRECT CURRENT GLOW DISCHARGES

DC glow discharge provides a convenient example to describe the fundamental physics behind the gas discharges, due to its simplicity; it consists only of two electrodes placed inside a low pressure gas. Due to the cosmic radiation, a small number of free electrons emitted from electrodes is always present in the gas. When sufficiently high potential difference is applied between the electrodes, these free electrons are accelerated by the electric field and they start colliding with the heavy particles, elastically and inelastically. Inelastic collisions will lead to excitation and ionization of the heavy particles and the gas will break down into positive ions and electrons, forming a gas discharge.

Excitation collisions are responsible for the name "glow." Namely, excited species emit light when de-exciting making the discharge "glow." New electrons and ions are created in ionization collisions. Ions are then accelerated toward the cathode where they release new electrons by ion-induced secondary electron emission (SEE). Now, these electrons collide with plasma species producing new particles, and the process is repeated. When there is always a sufficient number of charged particles in the system, gas discharge is called a self-sustained plasma [19].

Glow discharge can be sustained over a wide range of pressures, starting from several mTorr to atmospheric pressure. It is, however, the product of pressure (or density) and distance between electrodes that is a true parameter of the glow discharge. Another true parameter is the reduced electric field, E/p or E/N_n. Discharges at low pressures and greater electrode distance show similar properties as discharges at high pressures when electrodes are closer to each other. The operating voltage ranges from 300 V to 1500 V, but glow discharge could operate at several kV for some applications [6]. Rare gases (Ar, He,...) together with reactive gases (N_2, O_2,...) are often used to sustain the glow discharge.

The most important process, where glow discharges are employed, is sputter deposition of dielectric films. However, during the deposition process electrodes become covered with the insulating material, due to the accumulation of positive and negative charges, and the glow discharge vanishes. A solution to this problem is to apply alternating voltage between electrodes, so they change polarity in a half cycle turn. That way, a charge accumulated in the first half cycle will be neutralized with the charge of the opposite sign when polarity of the electrode is changed. When the voltage applied alternates in the radio-frequency range (1 KHz - 10^3 MHz) the discharge

is called a radio-frequency (RF) discharge.

2.1.2 CAPACITIVELY COUPLED RF DISCHARGES

As it was already stated, RF discharges operate in RF frequency range, with the most common frequency of 13.56 MHz. The frequency should be high enough so that its half cycle time is less than the accumulation time of the insulation around the electrode. Otherwise the plasma will consist of series of short lived discharges instead of a quasi-continuous discharge. The name capacitively coupled (CC) comes from the way in which the input power is coupled into discharge by two parallel planar electrodes resembling a capacitor.

The capacitively coupled RF discharge operates in the following way. Fast electrons, due to their low mass, are able to follow the instantaneous electric field produced by the RF applied voltage and oscillate back and forth between electrodes. Massive ions, on the other hand, can only follow time averaged electric fields. The oscillation of the electrons will create a sheath region of positive charges near each electrode. As a consequence, a strong electric field directed from plasma to the electrode will be generated. This electric field will accelerate positive ions toward electrodes giving them enough energy for ion-enhanced energetic bombardment of the electrode. On the other hand, due to the electric field in plasma sheath, a force directed into plasma will act on the electrons reflecting them back to the plasma. This will secure the electron confinement in the plasma system.

Electrons oscillate with the frequency called an electron plasma frequency, which is given as

$$f_{pe} = \frac{\omega}{2\pi} = \frac{1}{2\pi}\sqrt{\frac{N_e \cdot e^2}{m \cdot \varepsilon_0}} \simeq 9000\sqrt{N_e} \ \ [\mathrm{Hz}], \tag{1}$$

where N_e is the electron density given in cm^{-3}, e is the elementary charge, m is the electron mass, and ε_0 is dielectric constant of vacuum. When plasma frequency is of the order of RF frequency, Eq. (1) leads to electron densities of the order of 10^9 - 10^{10} cm^{-3}. Capacitively coupled RF discharges typically operate in 10-100 mTorr pressure range by applying power densities of 0.1-1 $\mathrm{W/cm}^3$ [6].

The main disadvantage of CC RF discharges is that the ion-bombarding flux and bombarding energy cannot be controlled independently. In other words, in order to

obtain a reasonable (but low) ion flux, the sheath voltage at the electrode has to be high. High sheath voltage at the electrode could result in undesirable damage to the etching sample placed on the driven electrode. A number of attempts to achieve some control over ion-bombarding energy, such as dual frequency operation or adding magnetically enhanced diodes, have been conducted in the past years [6]. However, these solutions are either not very practical or can result in generating a highly non-uniform plasma. To overcome the limitations of the capacitively coupled RF discharges, a new generation of low pressure, high density plasma sources has been developed.

2.1.3 HIGH DENSITY RADIO-FREQUENCY AND MICROWAVE DISCHARGES

The low pressure, high density plasma sources are characterized with higher plasma densities (10^{10} - 10^{13} cm^{-3}) for lower pressures, which results in higher ion fluxes than in CC RF discharges of similar pressures. These plasmas can be generated using RF frequencies (1 to 100 MHz) or MW frequencies (300 MHz to 10 GHz). The common feature for RF and MW plasmas is that instead of dumping the power directly to electrodes, the RF and MW power is coupled to the plasma across a dielectric window. In that way electrodes are not required any more and can be removed from the system. It should be noted that microwaves allow us to work at higher pressures and generate higher plasma densities.

For all these reasons we have chosen in the present work to employ both RF and MW high density plasmas at wide range of pressures (10 mTorr to 10 Torr) for plasma etching and cleaning processes. However, this is just the first step in optimizing the process of surface modification. The next step is to fully characterize desired plasmas. This includes obtaining important plasma parameters (electron densities and temperatures, gas densities and temperatures, population densities of excited atoms/molecules, etc.), describing their time and spatial distribution, and maintaining the full control over the plasma system.

In the course of developing methods for plasma characterization, we have concentrated on electrodeless MW induced plasmas that operate at two different frequencies, 2.45 GHz and 9.5 GHz. Plasmas were sustained in argon and in air at pressure of 1-10 Torr. Since the Ar plasma contains atomic gas and air plasma contains mostly molecules (N_2, O_2, CO_2), both atomic and molecular structure of MW discharges

was analysed spectroscopically. In order to describe these plasmas without disturbing them we have applied only non intrusive optical techniques (optical emission spectroscopy and laser diagnostics).

2.2 FUNDAMENTAL PLASMA EQUATIONS

Collective plasma properties such as temperature and electron density, are dependent on the internal plasma dynamics. Plasma particles (electrons, atoms/molecules, and ions) collide under the action of the electromagnetic field and exchange energy and momentum in the process, thus changing plasma properties in time and space. Total energy and momentum are always conserved in the collision, i.e. total energy and total momentum of the colliding particles before collision are equal to that after collision.

Since electrons are the elementary particles they possess kinetic energy only, while atoms/molecules and ions have internal energy level structure (they can be excited or ionized and molecules can rotate and vibrate), which corresponds to potential energy change. The collision is called elastic when the total internal energy, and thus total kinetic energy remains unchanged. When total kinetic energy is not conserved, the collision is said to be inelastic. Inelastic collisions usually result in excitation

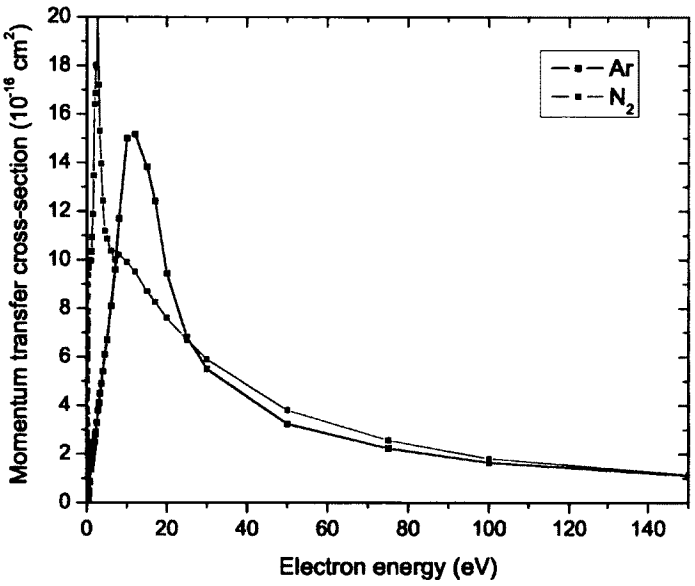

FIG. 1. Momentum transfer cross-sections for electron scattering in Ar and N_2 [20].

and ionization of atoms/molecules, but dissociation, recombination, attachment, etc.

can also occur when molecules are involved. In this section we will consider the fundamental quantities that characterize particle collisions (collisional cross-sections and rate coefficients) and basic equations that govern plasma particle dynamics.

To exemplify the different behaviour of argon and air plasmas we have shown in Fig. 1 a comparison between the Ar and N_2 momentum transfer cross-sections [20]. It could be seen from the figure that in the case of the atomic argon discharges the maximum probability for momentum transfer is shifted to the higher energies compared to the molecular N_2 discharges.

2.2.1 COLLISIONAL CROSS-SECTIONS

Collisional cross-section is the fundamental quantity to describe a collision. It is the probability for a given process to happen and is defined as the area around a particle where the center of another particle must be in order for a collision to occur. Therefore, the cross-section is given in the units of area [m^2]. Conventionally, the symbol for collisional cross-section is $\sigma(v_R, \theta)$, where v_R is the relative velocity between the particles before collision and θ is the scattering angle between the particles after the collision [6].

We can calculate integrated cross-sections by integrating the collisional cross-sections over the solid angle [6,21]

$$\sigma_I = 2\pi \int_0^{\pi} \sigma(v_R, \theta) \sin\theta \, d\theta. \tag{2}$$

It is often useful to define a momentum transfer or diffusion cross-section [6]

$$\sigma_M = 2\pi \int_0^{\pi} \sigma(v_R, \theta)(1 - \cos\theta) \sin\theta \, d\theta, \tag{3}$$

where the factor (1-cosθ) is the fraction of the initial momentum lost by the incident particle.

Depending on the type of collision outcome we distinguish cross-sections for elastic and inelastic collisions. Elastic collisions mostly happen between an electron and a heavy particle. An example of the elastic momentum transfer cross-section from Ref. [20], for electron scattering in Ar and N_2 is given in Fig. 1.

Under the most common plasma conditions, inelastic collisions involve excitation of the neutral atom/molecule by an electron impact. In this study, we will consider

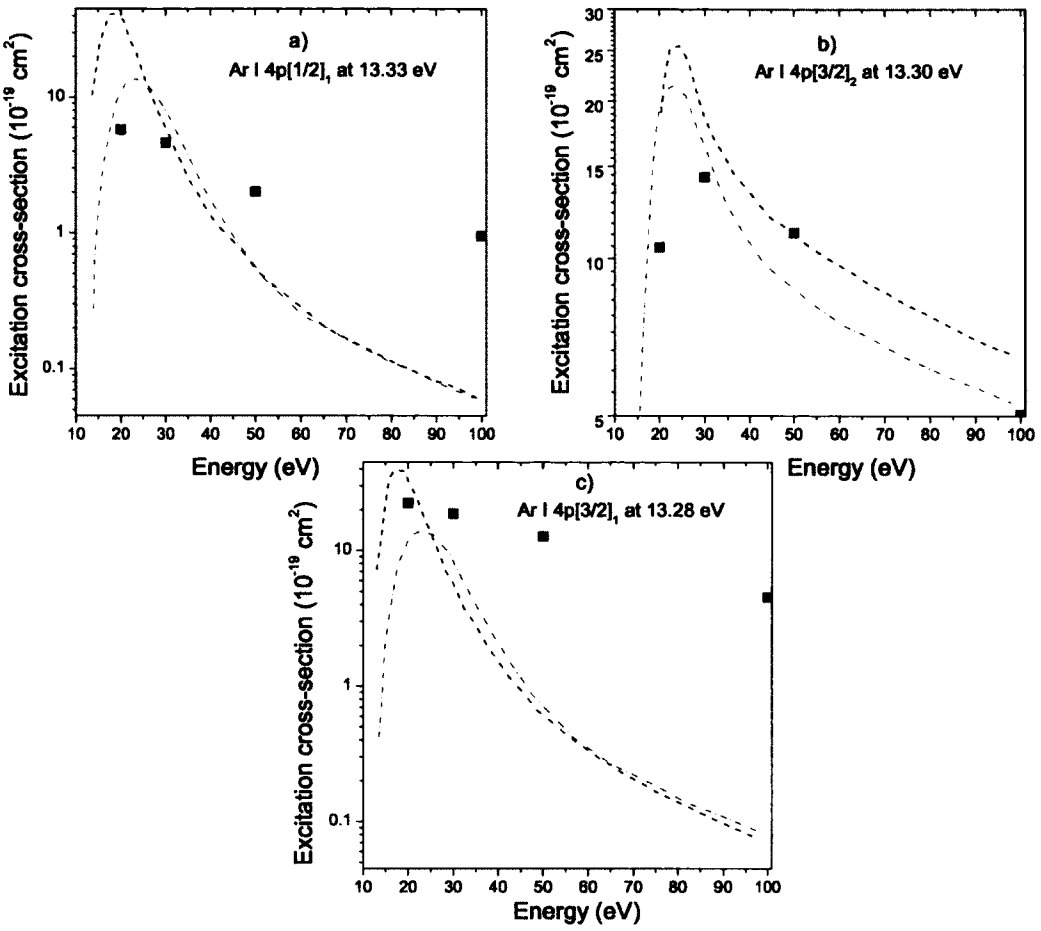

FIG. 2. Electron impact excitation cross-sections from Ar I ground state to Ar I a) $4p\ [1/2]_1$, b) $4p\ [3/2]_2$, and c) $4p\ [3/2]_1$ states. Dashed lines present theoretical predictions from Ref. [24], and dots present theoretical predictions from Ref. [25]. Experimental results from Ref. [22,23] are connected with straight lines for better visualisation.

only inelastic integrated cross-sections for electron impact collisions. In the case of atomic argon we will show electron impact excitation cross-sections from ground and lowest $4s[3/2]_2$, $J = 2$ state at 11.55 eV to three p states:

- $4p\ [1/2]_1$, $J = 1$ Ar state at 13.33 eV
- $4p\ [3/2]_2$, $J = 2$ Ar state at 13.30 eV

- $4p\ [3/2]_1$, $J = 1$ Ar state at 13.28 eV,

Figure 2 shows comparison between measured [22,23] and calculated [24,25] electron impact excitation cross-sections from ground state to p states of argon. It can be seen from the figure that there is a disagreement by factor 2-4 between the results, implying that both measured and calculated cross-sections should be taken with caution. It should be noted that electron argon excitation presented in experimentally obtained results has also a threshold, but it was not measured.

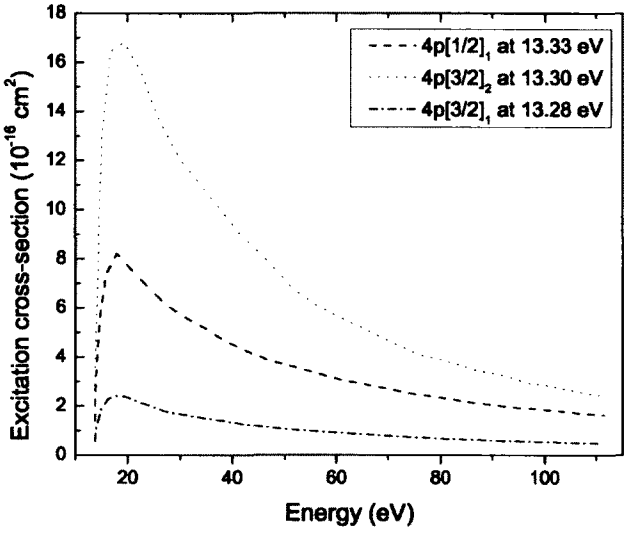

FIG. 3. Calculated electron impact excitation cross-sections from Ar I metastable $4s[3/2]_2$ state to Ar I a) $4p\ [1/2]_1$, b) $4p\ [3/2]_2$, and c) $4p\ [3/2]_1$ states [25].

Available experimental and theoretical cross-sections from the Ar I metastable levels are very sparse. In Fig. 3 are presented calculated electron impact excitation cross-sections from metastable $4s[3/2]_2$ state [25]. As can be seen, the peak values of the excitation cross-sections from the metastable state are almost three orders of magnitude higher than peak values of the excitation-cross sections from the ground states implying that the distribution of the argon metastable levels plays more important role in understanding plasma kinetics than the distribution of the ground state.

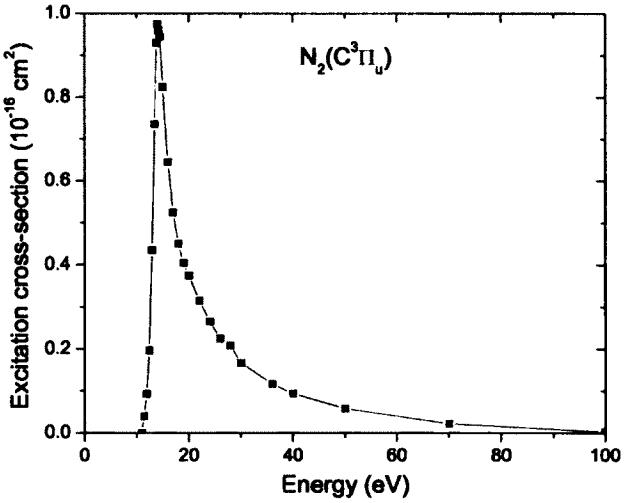

FIG. 4. Electron impact excitation cross-sections from N_2 ground state to $N_2(C^3\Pi_u)$ state [20]. Experimental results are connected with straight lines for better visualisation.

In addition, as an example of molecular plasma structure, experimentally obtained electron impact excitation cross-section from the ground state of nitrogen to the excited $C^3\Pi_u$ state [20] is presented in Fig. 4.

2.2.2 BOLTZMANN EQUATION

Various collective effects of particle interactions, such as ionization and excitation of atoms by electron impact, quenching of neutral atoms, for example, can be described only by knowing the particle distribution function. The form of the distribution function can be obtained from the Boltzmann kinetic equation. The general kinetic Boltzmann equation for the distribution function of particles in gas gives the balancing of the number of particles in an elementary volume in phase space.

For a given species, we introduce a distribution function $f(\vec{r}, \vec{v}, t)$ in the six dimensional phase space. Let us illustrate an elementary volume in three dimensional space coordinate system, shown in Fig. 5 [8]. The cubic volume $d\Gamma = dxdydzdv_xdv_ydv_z$ contains $fd\Gamma$ particles. The number of particles per second entering the area through xy surface at distance z is $(fv_z)_z dxdydv_xdv_ydv_z$. The number of particles per second leaving through the opposite surface at distance $z + dz$ is $(fv_z)_{z+dz}dxdydv_xdv_ydv_z$.

The difference is then,

$$[(fv_z)_z - (fv_z)_{z+dz}]dxdydv_xdv_ydv_z = -\Big[\partial(fv_z)/\partial z\Big]d\Gamma, \tag{4}$$

and it contributes to the rate of particle accumulation in the tube, $(\partial f/\partial t)d\Gamma$. The similar procedure can be applied to the other five cube surfaces. After collecting all the terms, the balancing equation for the number of particles due to the collisions between particles becomes

$$\frac{\partial f}{\partial t} + \Big[\frac{\partial}{\partial x}(fv_x) + ... + \frac{\partial}{\partial v_x}(fa_x) + ...\Big] = \Big(\frac{df}{dt}\Big)_C, \tag{5}$$

where $\vec{a} = d\vec{v}/dt$ and $\left(\frac{df}{dt}\right)_C$ is the rate of change of the distribution function in time and space due to collisions.

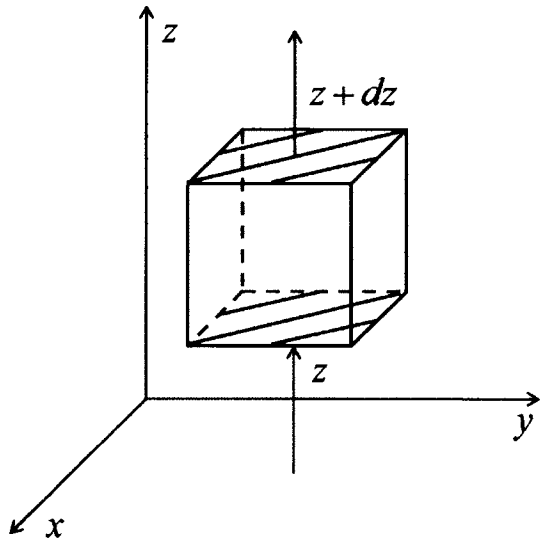

FIG. 5. A cube in three dimensional space illustrating the derivation of the Boltzmann equation.

If we compare this to the derivative $\partial f/\partial t$,

$$\begin{aligned} \frac{df}{dt} &= \frac{\partial f}{\partial t} + \frac{\partial f}{\partial x}\frac{dx}{dt} + ... + \frac{\partial f}{\partial v_x}\frac{dv_x}{dt} + ... \\ &= \frac{\partial f}{\partial t} + v_x\frac{\partial f}{\partial x} + ... + a_x\frac{\partial f}{\partial v_x} + ..., \end{aligned} \tag{6}$$

we obtain

$$\frac{df}{dt} + f\Big[\frac{\partial v_x}{\partial x} + ... + \frac{\partial a_x}{\partial v_x} + ...\Big] = \Big(\frac{df}{dt}\Big)_C. \tag{7}$$

The quantities x, v_x, a_x,... are independent coordinates in phase-space. Therefore, the term $\Big[\frac{\partial v_x}{\partial x} + ... + \frac{\partial a_x}{\partial v_x} + ...\Big]$ vanishes and

$$\frac{df}{dt} = \Big(\frac{df}{dt}\Big)_C. \tag{8}$$

This means that in the absence of collisions, the particle number density does not change with time even though particles are moving along the trajectory in the phase-space.

Equation (5) can be rewritten as

$$\frac{\partial f}{\partial t} + v_x\frac{\partial f}{\partial x} + v_y\frac{\partial f}{\partial y} + ... + a_x\frac{\partial f}{\partial v_x} + a_y\frac{\partial f}{\partial v_y} + ... = \Big(\frac{df}{dt}\Big)_C, \tag{9}$$

or

$$\frac{\partial f}{\partial t} + \vec{v}\cdot\nabla f + \vec{a}\cdot\nabla_v f = \Big(\frac{df}{dt}\Big)_C, \tag{10}$$

where ∇_v is gradient in velocity space. This represents the general form of Boltzmann kinetic equation to be used for transport of charged particles in a plasma.

In this study we will mainly investigate electrons moving in electromagnetic field such that magnetic force is negligible comparing to the electric force. Hence, the Lorentz force vanishes in the acceleration term. The Boltzmann equation (10) then becomes

$$\frac{\partial f}{\partial t} + \vec{v}\cdot\nabla f - \frac{e\vec{E}}{m}\cdot\nabla_v f = \Big(\frac{df}{dt}\Big)_C, \tag{11}$$

where e is the elementary charge, m is the electron mass and $\vec{E}$ is the electric field.

In order to solve Eq. (11) we consider only spatially uniform fields which is true either in case of constant or in case of high frequency electromagnetic fields because the amplitude of electronic oscillations is small compared to the EM wavelength. The electron distribution function is then symmetric in velocity space around the electric field direction. Thus,

$$\vec{v}\cdot\nabla f = v\cdot\frac{\partial f}{\partial r} = v\frac{\partial f}{\partial z}\frac{\partial z}{\partial r} = vcos\theta\frac{\partial f}{\partial z}, \tag{12}$$

where $z = rcos\theta$.

If we assume electric field in z direction, $\vec{E} = E\vec{e_z}$, in cylindrical coordinates in velocity space, $\vec{e_z} = \vec{e_v}cos\theta - \vec{e_\theta}sin\theta$, we get

$$\vec{E}\cdot\nabla_v f = E\frac{\partial f}{\partial v}cos\theta - E\frac{1}{v}\frac{\partial f}{\partial\theta}sin\theta = E\Big(cos\theta\frac{\partial f}{\partial v} + \frac{sin^2\theta}{v}\frac{\partial f}{\partial(cos\theta)}\Big), \tag{13}$$

where we employed

$$\frac{\partial f}{\partial \theta} = \frac{\partial f}{\partial (cos\theta)} \frac{\partial (cos\theta)}{\partial \theta}. \tag{14}$$

Boltzmann equation gets the form of

$$\frac{\partial f}{\partial t} + vcos\theta \frac{\partial f}{\partial z} - \frac{e}{m} E\Big(cos\theta \frac{\partial f}{\partial v} + \frac{sin^2\theta}{v} \frac{\partial f}{\partial (cos\theta)}\Big) = \Big(\frac{df}{dt}\Big)_C. \tag{15}$$

Equation (15) can not be solved analytically without making some drastic simplifications. In the following sections, we will discuss different approaches for obtaining the electron distribution function from Eq. (15).

It can be seen from Eq. (15) that Boltzmann equation strongly depends on electric field amplitude. Depending on the electric field strength two characteristic situations can be distinguished

- Moderate electric fields
- Strong electric fields

Moderate electric fields

The common approach to solve the Eq. (15) is by expanding electron distribution in terms of Legendre polynomials of $cos\theta$ (spherical harmonics expansion). For most applications it is enough to use only the first two expansion terms

$$f(v, cos\theta, z, t) = f_0(v, z, t) + f_1(v, z, t) cos\theta, \tag{16}$$

where f_0 represents a symmetric, isotropic part of distribution function which determines the electron energy spectrum, and f_1 is a small anisotropic perturbation. Hence, the approximation is valid when the collisions are dominantly elastic and will fail for high values of electric field when most of the collisions are inelastic and the anisotropic part becomes dominant. However, a small inelastic contribution will be still present in the collision term on the right hand side

We then substitute Eq. (16) into Eq. (15), multiply by the respective Legendre polynomials (1 and $cos\theta$) and integrate over all angles $\int 2\pi sin\theta d\theta$,

$$\frac{\partial f_0}{\partial t} + \frac{v}{3} \frac{\partial f_1}{\partial z} - \frac{eE}{m} \frac{1}{3v^2} \frac{\partial (v^2 f_1)}{\partial v} = C_0, \tag{17}$$

$$\frac{\partial f_1}{\partial t} + v \frac{\partial f_0}{\partial z} - \frac{eE}{m} \frac{\partial (f_0)}{\partial v} = -N_n \sigma_m v f_1, \tag{18}$$

where C_0 represents the change in f_0 due to collisions, N_n is population density of neutrals, and σ_m is total momentum-transfer cross-section consisting of contributions from all possible collisions processes k

$$\sigma_m = \sum_k x_k \sigma_k \tag{19}$$

where k is the mole fraction of the target species of the collision process. In the case of elastic collisions, σ_k represents the effective momentum-transfer cross-section, as described in previous subsection, while in the case of inelastic collisions, σ_k is the inelastic integrated cross-section where all momentum is lost in the collision.

Collision term, C_0, consists of two terms:

- Elastic collisions [9]

$$C_{el} = \frac{m}{M}\frac{1}{v^2}\frac{\partial}{\partial v}\Big[v^3 N_n \sigma_m v\Big(f_0 + \frac{eT_g}{mv}\frac{\partial f_0}{\partial v}\Big)\Big], \tag{20}$$

  where M is the mass of target particle.

  The first term on the right hand side of the equation is due to the elastic scattering energy losses, while the second term is due to energy diffusion from the non zero temperature. The second term is very small and can be neglected in most cases.

- Inelastic collision

$$C_{inel} = -N_n \sigma_{inel} v f_0(v) + \frac{v'}{v} N_n \sigma_{inel} v f_0(v'), \tag{21}$$

  where $v'^2 = v^2 + 2e\varepsilon_{inel}/m$ and ε_{inel} is the electron energy lost in an inelastic collision [9].

Equations (17) and (18) are further simplified by separating velocity dependence from space-time dependence of electron distribution function as

$$f_{0,1}(v, z, t) = F_{0,1}(v) N_e(z, t), \tag{22}$$

where N_e is the electron number density. The electron distribution function is normalized over velocity space as

$$\int_0^\infty f(v, cos\theta, z, t) d\vec{v} = 4\pi \int_0^\infty N_e(z, t) F_0(v) v^2 dv = N_e(z, t), \tag{23}$$

Before going to the general solution we will describe several simplified approaches. In the simple case of steady-state plasmas where only elastic collisions take place, equations (17) and (18) become

$$-\frac{eE}{3m}\frac{\partial(v^2F_1(v))}{\partial v} = \frac{m}{M}\frac{\partial(v^3N_n\sigma_m(v)vF_0(v))}{\partial v}, \tag{24}$$

$$\frac{eE}{mN_n\sigma_m(v)v}\frac{\partial(F_0(v))}{\partial v} = F_1(v), \tag{25}$$

Integrating Eq. (24) and equating it with Eq. (25) we obtain

$$-\frac{e^2E^2}{3m^2}\frac{1}{N_n\sigma_m(v)v}\frac{\partial(F_0(v))}{\partial v} = \frac{m}{M}vN_n\sigma_m(v)vF_0(v). \tag{26}$$

It is often useful to introduce a collision frequency defined as

$$\nu_m(v) = N_n\sigma_m(v)v, \tag{27}$$

which transforms Eq. (26) into

$$\frac{\partial(F_0(v))}{\partial v} = -\frac{3m^3}{e^2E^2M}v\nu_m^2(v)F_0(v). \tag{28}$$

Hence,

$$F_0(v) = Aexp\Big[-\frac{3m^3}{e^2E^2M}\int_0^v v'\nu_m^2(v')dv'\Big], \tag{29}$$

where A is a normalization constant.

Maxwell-Boltzmann distribution

At the thermodynamic equilibrium, where particles do not constantly interact with each other but move freely between short collisions, collision frequency ν_m is velocity independent and Eq. (29) becomes

$$F(v) = \Big(\frac{m}{2\pi T_e}\Big)^{3/2}e^{-mv^2/2T_e}, \tag{30}$$

where the electron temperature T_e, is measured in energy units.

It is sometimes useful to express electron distribution function in terms of energy rather than velocity coordinates. Using the identity that the number of electrons with velocities between $\vec{v}$ and $\vec{v}+d\vec{v}$ equals to the number of electrons with energies between ε and $\varepsilon+d\varepsilon$

$$F(\varepsilon)d\varepsilon = F(\vec{v})d\vec{v} = 4\pi F(v)v^2dv, \tag{31}$$

and $e\varepsilon = mv^2/2$ we observe

$$F(\varepsilon) = 4\pi F(v)v^2\frac{dv}{d\varepsilon} = 2\pi\left(\frac{2e}{m}\right)^{3/2}\varepsilon^{1/2}F(v(\varepsilon)). \tag{32}$$

The function, $f(\varepsilon)$, is called the electron energy distribution function (EEDF) and has the units of eV^{-1}. Energy normalization of the electron energy distribution function is deduced from Eq. (23)

$$\int_0^\infty F(\varepsilon)d\varepsilon = \int_0^\infty Fd\vec{v} = N_e. \tag{33}$$

Beside EEDF we will also introduce another function named electron energy probability function (EEPF) that is related to the EEDF as

$$G(\varepsilon) = \varepsilon^{-1/2}F(\varepsilon). \tag{34}$$

Electron energy probability function has the units of $eV^{-3/2}$ and normalized over all energies gives unity

$$\int_0^\infty G(\varepsilon)d\varepsilon = \int_0^\infty \varepsilon^{-1/2}F(\varepsilon)d\varepsilon = 1. \tag{35}$$

Equation (30) in energy units has the form of

$$F_M(\varepsilon) = \frac{2}{\sqrt{\pi}}T_e^{-3/2}\sqrt{\varepsilon}e^{-\varepsilon/T_e}. \tag{36}$$

At the end of the nineteenth century, Maxwell discovered this relation purely empirically. It was much later when Ludwig Boltzmann came out with the rigorous proof and the function, F_M is known as Maxwell-Boltzmann distribution.

Druyvesteyn distribution

Generally, the EEDF is assumed to be Maxwellian at very low pressures (less than 50 mTorr) where the electron-electron collisions dominate. For higher pressures the energy distribution function of the electrons is often better approximated by another function which is nowadays well-known as the Druyvesteyn distribution function. Back in 1930, Druyvesteyn showed that this distribution may be considered an adequate description of the EEDF when electrons satisfy following assumptions [26]:

- only elastic collisions between electrons and heavy particles (ions and neutrals) are taken into account (inelastic processes, ionization and excitation, are neglected)

- electron-electron collisions are neglected
- total cross-sections for electron-neutral collisions do not depend on electron energy
- electron temperature is much greater than the ion and neutral temperature ($T_e \gg T_g$)

For an isotropic distribution, the Druyvesteyn distribution [26] may be written as

$$F_D(\varepsilon) = 0.568 \cdot T_e^{-3/2} \sqrt{\varepsilon} e^{-0.243(\varepsilon/T_e)^2} \tag{37}$$

Physically, Maxwellian distribution function is applicable when the electron collision frequency is velocity independent, while Druyvesteyn distribution dominates when the mean free path is velocity independent. Graphical comparison between Maxwellian and Druyvesteyn distribution function is given in Fig. 6.

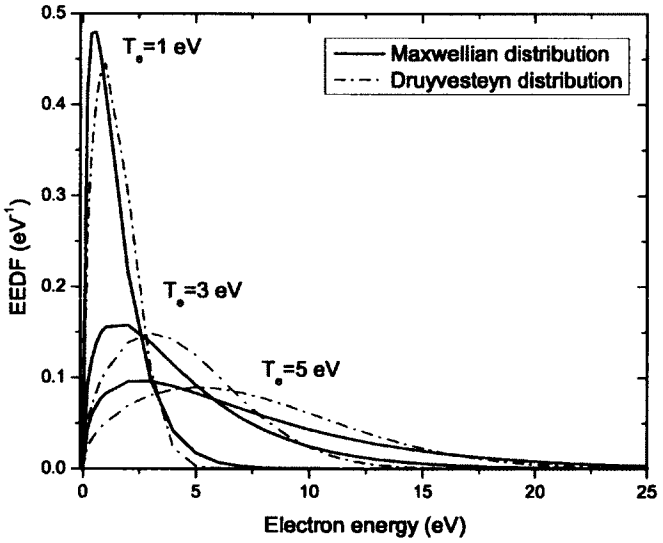

FIG. 6. Comparison of Maxwellian and Druyvesteyn distribution functions.

In comparison with Maxwellian distribution, Druveysteyn distribution contains much fewer high energy electrons and is characterized by a shift of the maximum towards a higher energy. Therefore, Druveysteyn electron energy distribution can be used as an approximation for the EEDF that is depleted at high energy.

Two-parameter distribution

Recently, studies were conducted on a global model that would cover the region of electron energy distribution as it is varied from being Maxwellian to become Druveysteyn like. Such a distribution is called a two-parameter distribution and its general form is [11]

$$F_x(\varepsilon) = C_1 T_x^{-3/2} \sqrt{\varepsilon} e^{-C_2(\varepsilon/T_x)^x}, \tag{38}$$

where

$$C_1 = x\Big(\frac{2}{3}\Big)^{3/2} \frac{[\Gamma(5/2x)]^{3/2}}{[\Gamma(3/2x)]^{5/2}}, \tag{39}$$

$$C_2 = \Big(\frac{2}{3}\Big)^x \Big[\frac{\Gamma(5/2x)}{\Gamma(3/2x)}\Big]^x, \tag{40}$$

with $\Gamma(\psi)$ being a Gamma function of ψ and T_x representing the effective electron temperature defined as 2/3 of the averaged electron energy. When $x = 1$ with $C_1 = 2/\sqrt{\pi}$ and $C_2 = 1$ Eq. (38) becomes Maxwellian. Similarly, when $x = 2$ with $C_1 = 0.568$ and $C_2 = 0.234$ we get Druveysteyn energy distribution. The case of $x = 4$ corresponds to Rutscher's type distributions [13], and should be the best fit for Ar discharges according to [13]. Figure 7 shows electron energy distribution functions derived from the Eq. (38) for different x with the same value of $T_x = 3$ eV (Fig. 7a) and $T_x = 0.5$ eV (Fig. 7b).

Solution of Boltzmann equation: BOLSIG+ solver

All the approximations described above assume steady-state plasmas where only elastic collisions occur between particles. The real case scenario is more complex and can not be explained fully with these simplified models. In general, when the electron distribution function depends on time and distance we still can separate velocity-dependence from time-dependence

$$f_{0,1}(v, z, t) = F_{0,1}(v) N_e(z, t), \tag{41}$$

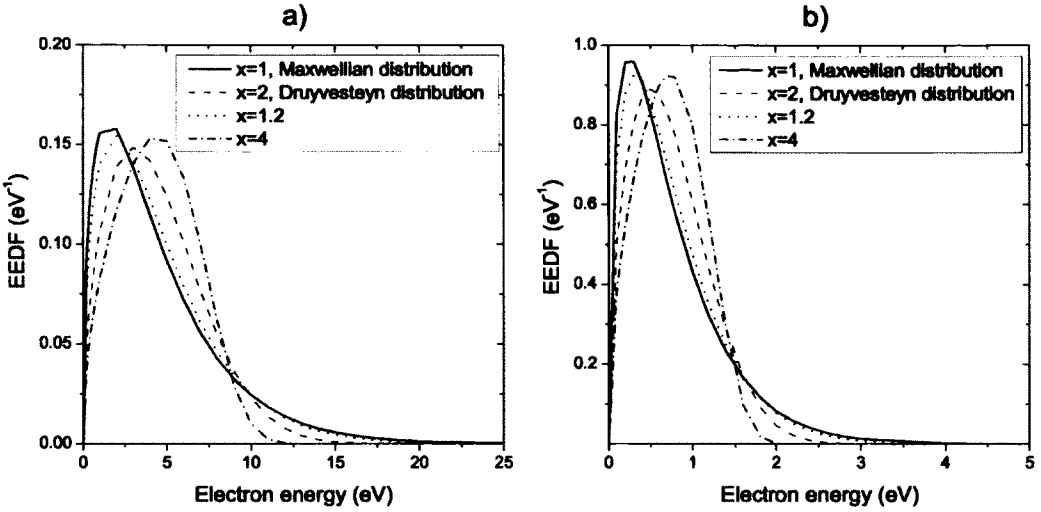

FIG. 7. EEDF calculated for four different distributions: $x = 1$ Maxwellian, $x = 2$ Druveysteyn, $x = 1.2$, and $x = 4$ for sample electron temperatures a) $T_x = 3$ eV and b) $T_x = 0.5$ eV.

Also, we are assuming that electric field either remains constant on the time scale of the collisions or is oscillating with high frequency ω, such that $\omega \gg \nu_m$, and

$$f(v, cos\theta, z, t) = f_0(v, z, t) + f_1(v, z, t) cos\theta e^{i\omega t}. \tag{42}$$

where the time variation of f_0 and f_1 is slow comparing to the E field oscillations. Equation (42) is applicable in microwave discharges where field oscillations are in the gigahertz range and beyond.

Our experiment was conducted in pure argon but some measurements of nitrogen molecular bands were performed in air discharge too. For that reason, in Figs. 8 and 9 we are showing the examples of electron energy probability functions in both argon and air plasma at gas temperature T_g=300 K using the two-term approach in free software BOLSIG+ [9]. As an input data we have employed gas temperature and reduced electric field together with the corresponding collision cross-sections. Note that EEPF in the two-term approach is calculated for given reduced electric field, E/N_n, unlike the other approaches where EEPF (or corresponding EEDF) is shown for different electron temperatures. To be able to compare these approaches we need to express T_e in terms of E/N_n. By employing the properties of distribution

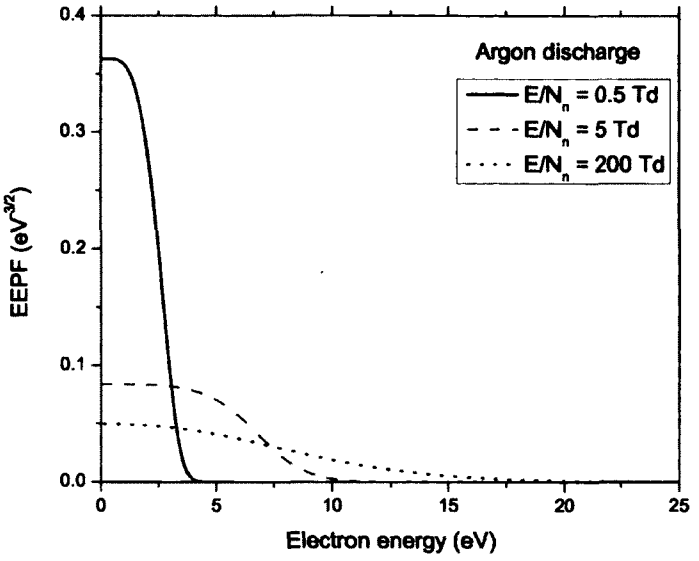

FIG. 8. EEPF for T_g=300 K in argon discharge for three different values of reduced electric field, 0.5 Td, 5 Td, and 200 Td.

functions and the relation $\varepsilon = \frac{3}{2}T_e$, average electron temperature can be expressed as

$$T_e = \frac{2}{3}\int_0^\infty \varepsilon F(\varepsilon)d\varepsilon, \tag{43}$$

or in terms of EEPF

$$T_e = \frac{2}{3}\int_0^\infty \varepsilon^{3/2} G(\varepsilon)d\varepsilon. \tag{44}$$

Figure 10a shows the electron temperature as a function of the reduced electric field in both Ar and air discharges at $T_g = 300$ K. It turns out that the change in gas temperature influences only weakly the T_e dependence on E/N_n, as it is presented in Fig. 10b. The similar results were observed in air.

It can be seen from the Fig. 10 that in argon discharge $T_e = 3$ eV corresponds to $E/N_n = 5$ Td and $T_e = 0.5$ eV corresponds to $E/N_n = 0.1$ Td. After scaling electron distributions to the same electron temperatures we compared EEDFs using two parameter approach and BOLSIG+ solver for Ar discharge. Results for $T_e = 3$ eV and $T_e = 0.5$ eV are shown in Fig. 11. It seems that the case $x = 4$ in two

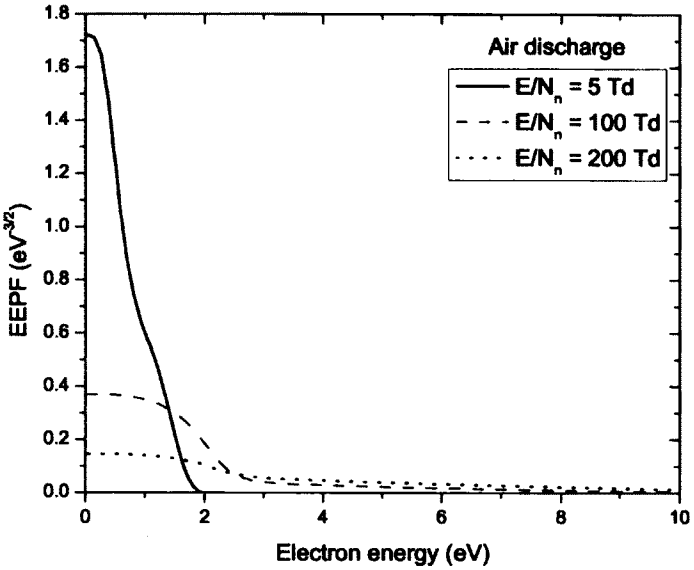

FIG. 9. EEPF for T_g=300 K in air discharge for three different values of reduced electric field, 5 Td, 100 Td, and 200 Td.

parameter approach is the best fit for Ar discharges, where there are more electrons with small energies but with high energy depletion in the tail of distribution.

In case of air discharge, it seems that electron temperature is smaller, due to the quenching processes for the same values of reduced electric field, compared to argon discharge. Moreover, at $E/N_n = 100$ Td which corresponds to $T_e = 1.8$ eV it is not even possible to compare different approaches. Figure 12a indicates that according to the two-term approach the electron energy distribution is much narrower than two parameter approach. When $E/N_n = 400$ Td or $T_e = 5.7$ eV the two approaches are comparable when $x = 1.2$, close to Maxwellian distribution, shown in Fig. 12b.

In this study, we concentrate on the kinetics of supersonic flowing MW discharge in argon operating at electron temperature $T_e = 0.5$ eV and gas temperature $T_g = 1500$ K. Since the change of gas temperature influences very weakly $T_e = f(E/N_n)$ dependence (shown in Fig. 10b), we can estimate reduced electric field to $E/N_n = 0.1$ Td (shown in Fig. 10a). From Fig. 11b can be concluded that either two parameter approach when $x = 4$ or BOLSIG+ solver can be employed for obtaining kinetic plasma properties (collision frequencies and rate coefficients) in argon.

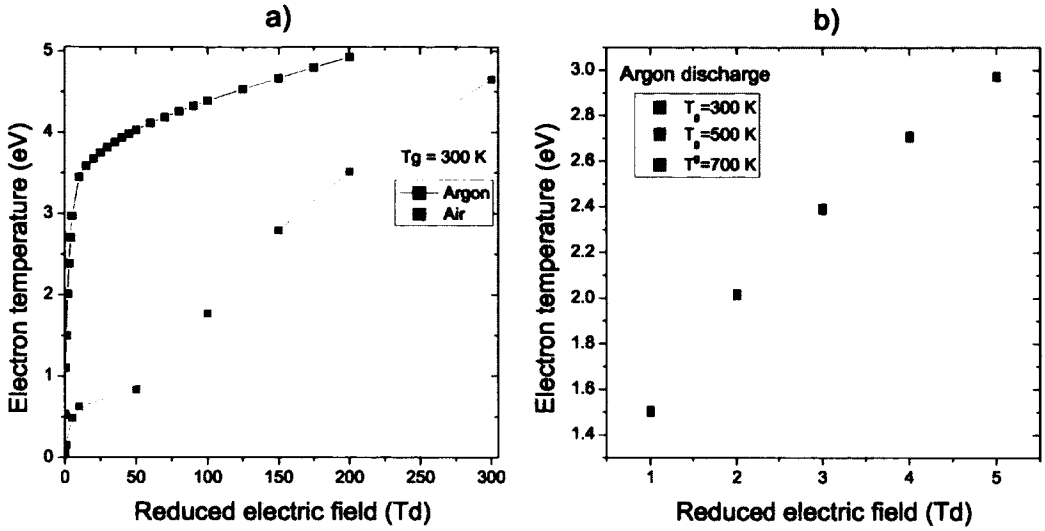

FIG. 10. Electron temperature as a function of reduced electric field at a) $T_g = 300$ K for Ar and air discharges and b) different gas temperatures, 300 K, 500 K, and 700 K in argon discharge.

In addition, we will study the kinetics of the pulse repetitive MW discharge in air with average electron temperature $T_e = 1.8$ eV and gas temperature ranging from $T_g = 600$ to 800 K. Similarly, as in the case of argon discharge, average reduced electric field was estimated to be $E/N_n = 100$ Td (shown in Fig. 10a). As can be seen from Fig. 12a, electron energy distribution function evaluated by employing two parameter approach when $x = 1.2$ differs in both shape and maximum intensity. Therefore, we have employed only BOLSIG+ solver based on two-term approach to characterize kinetic structure of the discharge.

Strong electric field

We were assuming previously that the EEDF was spherically symmetric. This assumption is valid only for electric field amplitudes that are not too large. As E increases, the energy of electrons oscillating in the field is increasing rapidly in time, and the ionization rate, ν_i is larger than the average electron collision rate. At very strong electric field amplitudes the electron energy distribution function is determined primarily by the ionization processes. As a consequence most of the electrons are

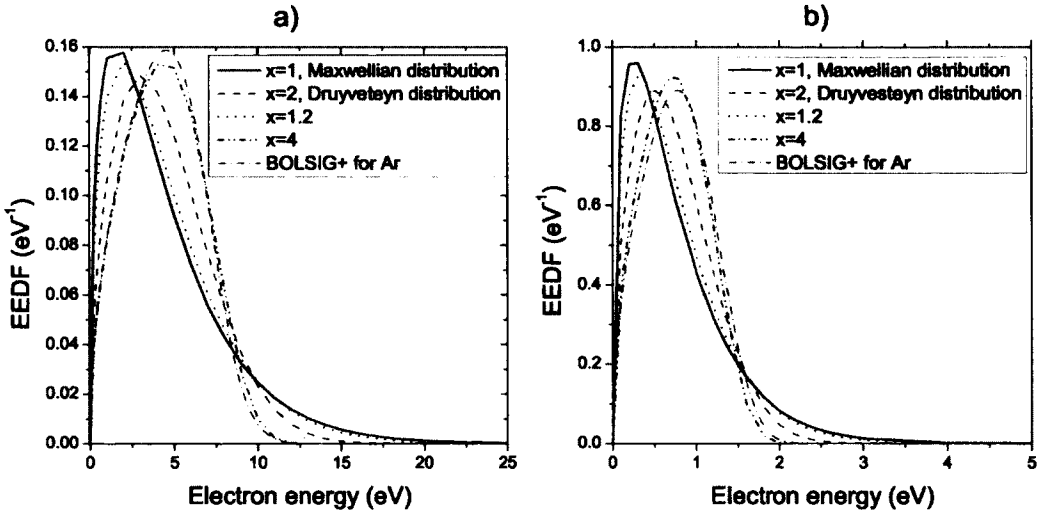

FIG. 11. Electron energy distribution function calculated using the two-parameter approach and the BOLSIG+ solver in argon for sample electron temperatures a) $T_e = 3$ eV and b) $T_e = 0.5$ eV.

slow and are picked up by the electric field while moving in the field direction. The EEDF, then, takes form of delta function [27]

$$f_G(\vec{v},t) = N_e F(\vec{v}) = N_e \delta(\vec{v} - \vec{v}_0 cos\omega t), \tag{45}$$

where ω the oscillation frequency of the field $\vec{E}(t) = \vec{E}_0(t) sin\omega t$ and

$$\vec{v}_0 = \frac{e\vec{E}_0}{m\omega}. \tag{46}$$

This approximation is valid in case of extremely high reduced electric fields ($E/N_n \geqslant 1000$ Td) when the form of electron energy distribution function is determined primarily by the ionization processes. Hence, the ionization rate coefficient is the dominant quantity that describes these discharges. However, for the purpose of comparison with the moderate field approximation, we will apply this approach to obtain rate coefficients for excitation processes.

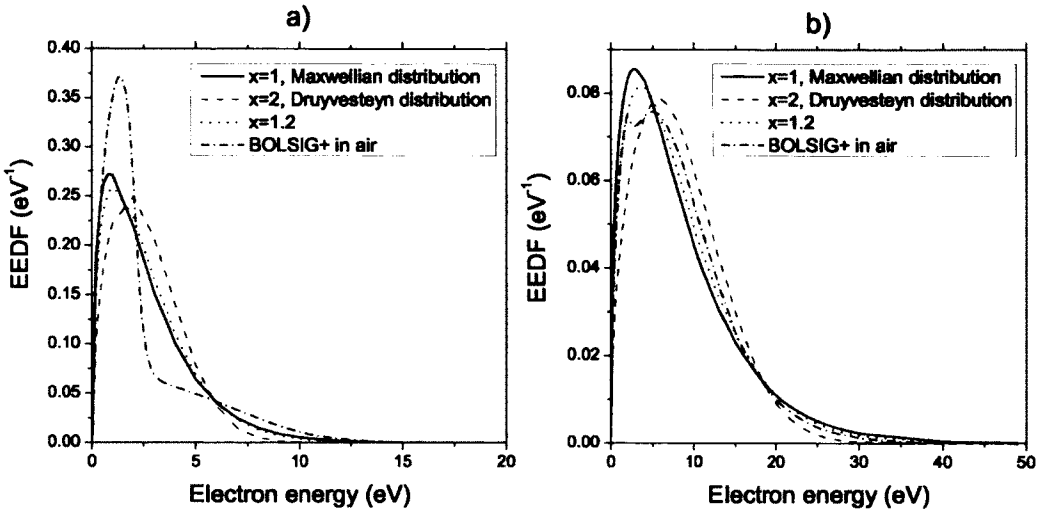

FIG. 12. Electron energy distribution function calculated using two parameter approach and BOLSIG+ solver for sample electron temperatures a) $T_e = 1.8$ eV and b) $T_e = 5.7$ eV in air discharge.

2.2.3 RATE COEFFICIENTS

One of the fundamental properties that characterize plasma system is the collision frequency defined as the number of interactions per second between two colliding particles (electrons and heavy atoms/ions in most cases)

$$\nu \equiv N_g \sigma(v_R) v_R \tag{47}$$

where v_R is the relative velocity and N_g is the gas density. In weakly ionized plasmas gas density can be estimated with the density of the neutral particles, $N_g = N_n$. Collision frequency per unit density is called the rate coefficient and is defined as

$$k = \sigma(v_R) v_R. \tag{48}$$

We will determine rate coefficients for both moderate and strong electric fields using the distributions functions and cross-sections described in previous subsections.

Electron impact collision rates

a) Moderate fields

We start by defining rate coefficients for inelastic collisions between an electron and a heavy atom/ion which can result in excitation or ionization of heavy particle. To obtain rate coefficients we integrate over the velocity distribution functions of the colliding particles

$$k = < \sigma(v)v > = \int_0^\infty \sigma(v_R)v_R F_1(\vec{v}_1)F_2(\vec{v}_2)d\vec{v}_1 d\vec{v}_2. \tag{49}$$

Heavy atoms/ions are assumed to be stationary ($\vec{v}_2 = 0$ and $F_2(\vec{v}_2) = 0$) and only electron motion is taken into account ($v_R = v_1 = v$ and $F_1(\vec{v}_1) = F(v)$).

Using the identity that the number of electrons with speeds between v and $v + dv$ equals to the number of electrons with energies between ε and $\varepsilon + d\varepsilon$

$$F(v)dv = F(\varepsilon)d\varepsilon, \tag{50}$$

and $\varepsilon = m_e v^2/2$ we observe

$$k = \left(\frac{2e}{m_e}\right)^{1/2} \int_0^\infty \sigma(\varepsilon)\sqrt{\varepsilon}F(\varepsilon)d\varepsilon. \tag{51}$$

The rate coefficient expressed in terms of $g(\varepsilon)$ is

$$k = \left(\frac{2e}{m_e}\right)^{1/2} \int_0^\infty \sigma(\varepsilon)\varepsilon G(\varepsilon)d\varepsilon. \tag{52}$$

Based on electron impact cross-sections for excitations from ground state to $4p$ levels of Ar I and electron energy distribution function, Eq. (51) gives the rate coefficients for electron impact excitation as functions of E/N_n, as shown in Fig. 14a. It should be noted that we have employed experimentally obtained cross-sections from Refs. [22,23]. These coefficients differed slightly (less than factor of 2) from the rate coefficients obtained by employing theoretically predicted cross-sections [24,25] that are not presented in this study.

Since experimentally obtained cross-sections for excitation from metastable $4s$ state to $4p$ states of Ar I were not available in literature, we have employed theoretically calculated cross-sections [25] together with EEDF in Eq. (51) to determine rate

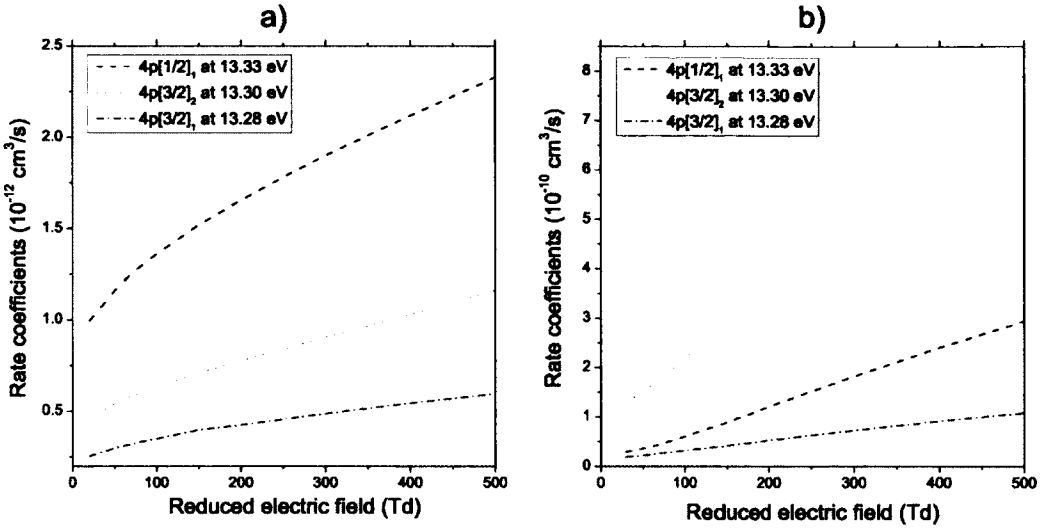

FIG. 13. Rate coefficient for electron impact excitation to Ar I $4p\ [1/2]_1$, $4p\ [3/2]_2$, and $4p\ [3/2]_1$ states from Ar I a) ground state and b) metastable $4s$ state dependence on reduced electric field using moderate field approximation.

coefficients for electron impact excitations from Ar I metastable state as functions of E/N_n, as shown in Fig. 14b. It could be seen from the figure that peak values of the excitation rate coefficients from the metastable state are almost three orders of magnitude higher than peak values of the excitation rate coefficients from the ground state confirming our assumption of Ar I metastable level significance in plasma kinetics. Although, it appears in Fig. 14b that values of excitation rate coefficients to $4p\ [3/2]_2$ state are higher than values of rate coefficients to $4p\ [1/2]_1$ state, this is probably due to the very poor accuracy in calculating required cross-sections and should be taken with caution.

We have also calculated rate coefficients for electron impact excitation from nitrogen ground state $N_2(X^1\Sigma^+)$ to excited $N_2(C^3\Pi_u)$ state, as shown in Fig. 14a. In addition, an example of vibrational excitation from $v = 0$ N_2 ground state to $v = 1-3$ states is presented in 14b. It can be deduced that the values of rate coefficients for vibrational excitation are comparable to the values of excitation rate coefficients to $N_2(C^3\Pi_u)$ state and should be included in defining nitrogen kinetic structure.

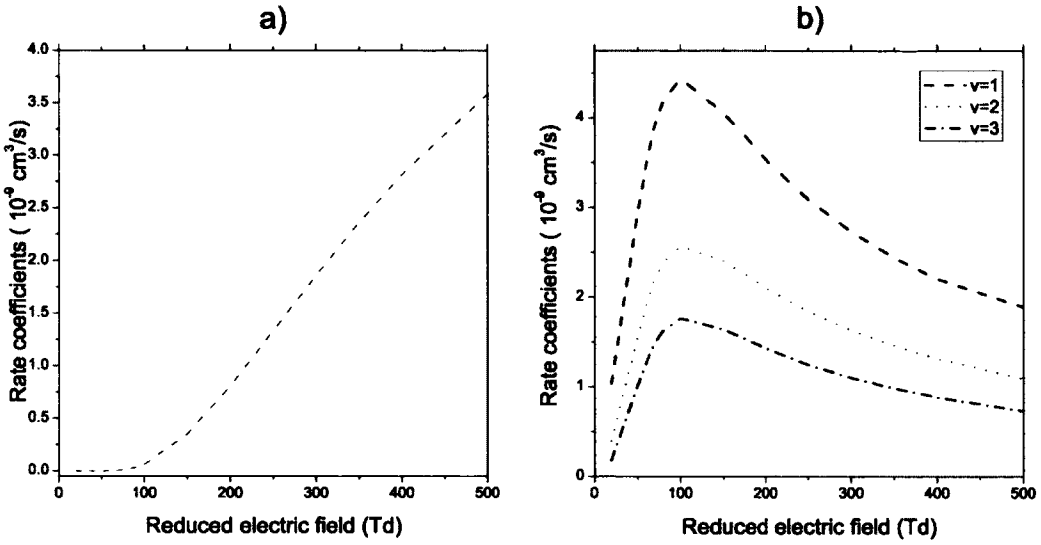

FIG. 14. Rate coefficient for electron impact excitation from ground state to a) $N_2(C^3\Pi_u)$ state and b) vibrationally excited ground state $v = 1 - 3$ dependence on reduced electric field in air discharge using moderate field approximation.

b) Strong electric fields

We start by writing the rate coefficient defined in Eq. (48) as

$$k(t) = < \sigma(v)v > = \int_0^\infty \sigma(v)vF(\vec{v})d\vec{v}. \tag{53}$$

In the large electric field approximation, we apply Eq. (45) for EEDF and the rate coefficient becomes

$$k(t) = \int_0^\infty \sigma(v)v\delta(\vec{v} - \vec{v}_0\cos\omega t)d\vec{v}. \tag{54}$$

By applying the identity

$$\int f(x)\delta(x - x_0)dx = f(x_0), \tag{55}$$

we get

$$k(t) = v_0 cos\omega t \cdot \sigma(v_0\cos\omega t). \tag{56}$$

To find the mean rate coefficient we average Eq. (56) in time

$$< k >= \frac{1}{T}\int_0^T k(t)dt, \tag{57}$$

where $T = \pi/\omega$ is a period of oscillation. Hence,

$$< k >= v_m\sigma_m\frac{\omega}{\pi}\int_0^{\pi/\omega}\frac{v_0}{v_m}\frac{\sigma(\frac{v_0}{v_m}cos\omega t)}{\sigma_m}cos\omega t dt, \tag{58}$$

where σ_m is the maximum collision cross section and v_m is the electron velocity corresponding to the maximum collision energy ε_m. By substituting $cos\omega t = \tau$ we derive

$$< k >= v_m\sigma_m\frac{2}{\pi}\int_0^1\frac{v_0}{v_m}\frac{\sigma(\frac{v_0}{v_m}\tau)}{\sigma_m}\frac{\tau d\tau}{\sqrt{1-\tau^2}}. \tag{59}$$

If we substitute $\frac{v_0}{v_m} = x$ and $\tau x = z = \frac{\varepsilon}{\varepsilon_m}$ Eq. (59) is transformed into

$$< k >= v_m\sigma_m\frac{2x}{\pi}\int_0^x\frac{\sigma(z)}{\sigma_m}\frac{zdz}{\sqrt{x^2-z^2}}. \tag{60}$$

Note that x

$$x = \frac{v_0}{v_m} = \frac{1}{v_m}\frac{eE_0}{m\omega} \tag{61}$$

depends linearly on electric field.

In order to estimate excitation rate coefficients as functions of reduced electric field by applying Eq. (60), oscillation frequency ω and gas density N_n need to be known. To exemplify Ar discharge, we present in Fig. 15a rate coefficients for electron impact excitation from ground state to $4p$ states at frequency $f = 2.45$ GHz and gas density $N_n = 2 \cdot 10^{16}$ cm^{-3}. Similarly, as an example of molecular N_2 structure, Fig. 15b shows rate coefficients for electron impact excitation from ground state of N_2 to excited $N_2(C^3\Pi_u)$ state at $f = 9.5$ GHz and $N_n = 2 \cdot 10^{17}$ cm^{-3}. We have chosen these frequencies and gas densities to simulate conditions of experimental systems described in following chapters. Figure 15a shows that in the strong electric field approximation ($E/N_n > 1000$ Td) values of excitation rate coefficients for Ar $4p$ states have increased in almost two orders of magnitude comparing to the values of the same coefficients in moderate electric fields ($E/N_n < 500$ Td). On the other hand, rate coefficient for electron excitation to N_2 ($C^3\Pi_u$) state varies very weakly when E/N_n increases, as shown in Fig. 15b.

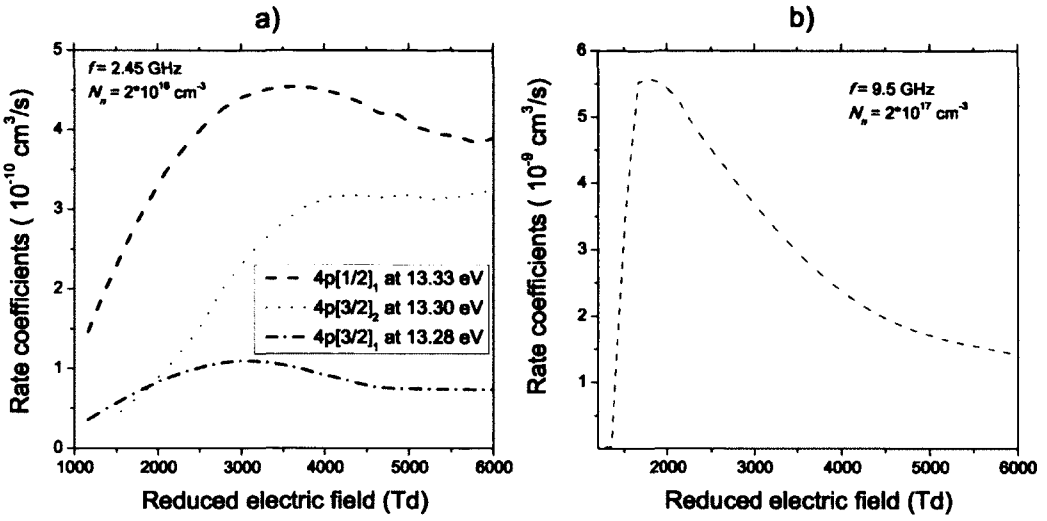

FIG. 15. Rate coefficient for electron impact excitation from ground state to excited a) $4p$ levels of Ar I and b) $(N_2(C^3\Pi_u))$ level dependence on reduced electric field using strong field approximation.

Collisional deactivation rate coefficients

Although they are less probable, collisions between heavy particles (atoms/ions) play significant role in gas discharge kinetics. These processes are also called quenching collisional deactivations. The general approach in obtaining quenching rate coefficients is to apply Eq. 49 which assumes the knowledge of distribution functions of colliding particles. It's proved to be fairly difficult to calculate heavy particles distribution functions so we applied the simple but effective methods for obtaining the collisional rate coefficients.

First, we describe method for obtaining collisional rate coefficients in argon discharge. The dominant quenching collision process includes population transfer processes between ground state $Ar(N_n)$ and $4p$ states $Ar(N_{px})$ of argon [28–30]:

$$\mathrm{Ar}(N_n) + \mathrm{Ar}(N_{px}) \rightarrow \mathrm{Ar}(N_n) + \mathrm{Ar}(N_{sm}), \tag{62}$$

where $Ar(N_{sm})$ describes metastable $4s$ state state of argon. Detailed description of the notation system used in kinetic analysis is given in Section 4.3.

Zhu and Pu [30] have combined available experimentally obtained and theoretically predicted rate coefficients for collisional quenching and presented them as functions of gas temperature T_g (given in Kelvins), as presented in Table 1.

TABLE 1. Collisional quenching rate coefficients for Ar I $4p$ states

	Processes	Rate coefficients (cm^3/s)
1	$Ar(N_n) + Ar(N_{p2}) \rightarrow Ar(N_n) + Ar(N_{1s})$	$1 \times 10^{-11}(T_g/300)^{0.5}$
2	$Ar(N_n) + Ar(N_{p3}) \rightarrow Ar(N_n) + Ar(N_{1s})$	$3 \times 10^{-11}(T_g/300)^{0.5}$
3	$Ar(N_n) + Ar(N_{p4}) \rightarrow Ar(N_n) + Ar(N_{1s})$	$3 \times 10^{-11}(T_g/300)^{0.5}$

Second, we employ the results of Brocklechurst and Downing [31] to obtain collisional rate coefficients in molecular nitrogen. Brocklechurst and Downing [31] have measured the ratio between collisional rate coefficient, $k_c^{X(0),C(0)}$, for process

$$N_2(C^3\Pi_u) + N_2(X^1\Sigma^+) \rightarrow 2N_2(X^1\Sigma^+), \tag{63}$$

and rate coefficient, $k_r^{C(0),B(0)}$, for radiative decay of $N_2(C^3\Pi_u)$ state to $N_2(B^3\Pi_g)$.

They have shown that this ratio depends on pressure and has a form

$$k = \frac{1}{p}\frac{k_c^{X(0),C(0)}}{k_r^{C(0),B(0)}}. \tag{64}$$

The experimental values for k taken from [31] are given in Table 2.

TABLE 2. Collisional quenching ratio for the second positive system of nitrogen by its ground state.

$N_2(C^3\Pi_u)$				
v	0	1	2	3
k (mm Hg)$^{-1}$	0.017±0.002	0.039±0.004	0.051±0.006	0.06±0.01

In the first approximation the rate coefficient for radiative decay is assumed to be inversely proportional to the radiative lifetime, τ_{CB}, of $N_2(C^3\Pi_u)$ level and gas

population density

$$k_r^{C(0),B(0)} = \frac{1}{\tau_{CB} N_n}. \tag{65}$$

By substituting Eq. (65) in the Eq. (64) we obtain rate coefficient for collisional deactivation

$$k_c^{X(0),C(0)} = \frac{kp}{\tau_{CB} N_n}. \tag{66}$$

Since pressure to gas density ratio depends linearly on gas temperature (ideal gas equation), it could be concluded that collisional rate coefficients in nitrogen are also functions of gas temperature similarly as collisional rate coefficients in argon.

CHAPTER 3

EXPERIMENTAL SYSTEMS

Our broader task is to fully characterize high density gas discharges required for plasma etching and cleaning purposes. Since these plasmas are non-equilibrium, non-stationary, fast moving, and chemically reactive it may be very challenging to obtain desired plasma parameters. One needs to verify some of the basic concepts outlined in Chapter 2 in well controlled experiments and develop plasma diagnostic techniques in generic geometries. We have conducted experiments in electrodeless microwave induced plasmas operating in the S-band (2.45 GHz, 200-400 W) and X-band (9.5 GHz, 210 kW) spectral range. Conventional diagnostic techniques, such as Langmuir probes, have the operating range up to 10^{11} - 10^{12} cm^{-3}, at least an order of magnitude lower than found in gas discharges at high densities [32]. Moreover, this method is both expensive and obtrusive. Therefore, we have chosen to apply optical emission spectroscopy along with laser diagnostics as our diagnostics tools since they are non-intrusive, *in situ*, and can accurately determine plasma parameters.

This chapter consists of two parts organized in the following order. The first part describes a supersonic flowing MW discharge in pure Ar sustained in a cylindrical resonant cavity, while the second part focuses on the surface MW discharge generated at the aperture of a horn antenna in air.

3.1 SUPERSONIC FLOWING MW DISCHARGE

3.1.1 EXPERIMENTAL SET-UP

The experiment was conducted in a supersonic flowing tube, radius $R = 1.6$ cm, combined with microwave cavity discharge, shown in Fig. 16. A commercial microwave generator, operating in the S-band at 2.45 GHz, was used to sustain a cylindrical cavity discharge at power density of up to 4 W/cm^3. The working pressure in the evacuated quartz tube was kept between 1 and 3 Torr. A Mach 2, cylindrical convergent-divergent De Laval nozzle was used to sustain the supersonic flowing discharge downstream of the microwave cavity, which operated in the TE_{111} mode. The measurements were performed in pure argon that was fed into the stagnation chamber through a gas manifold. Gas flow was established by a roots blower (Pfeiffer Okta 500 A), which was supported by two roughing pumps (Varian SD-700). The capacity of the pumping system allowed for generation of supersonic flow at static pressures of 1 to 20 Torr.

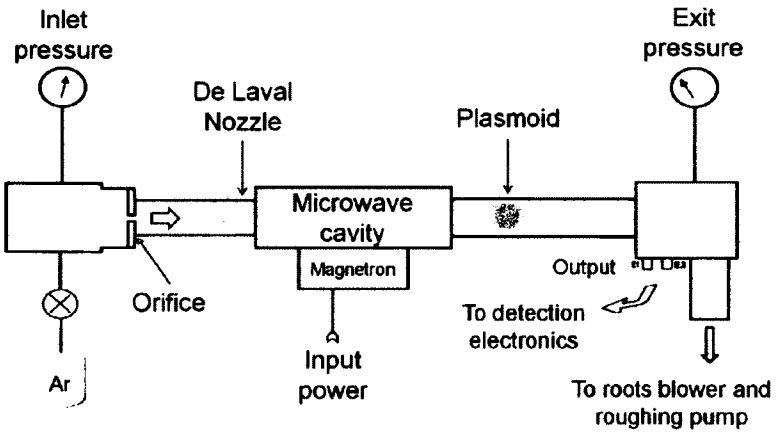

FIG. 16. Scheme of the supersonic flowing microwave discharge.

In the afterglow region of the pure Ar discharge, a plasmoid-like formation was observed as a secondary downstream phenomenon coupled to the microwave cavity. The plasmoid appears to be sustained by a low power surface wave, which propagates along its surface and the surface of the quartz tube. Our initial analysis led to the conclusion that plasmoid formation may be caused by aerodynamic effects in the supersonic flow. The full interpretation of the plasmoid discharge requires knowledge of all effects causing its formation. In addition, we have concluded that the plasmoid

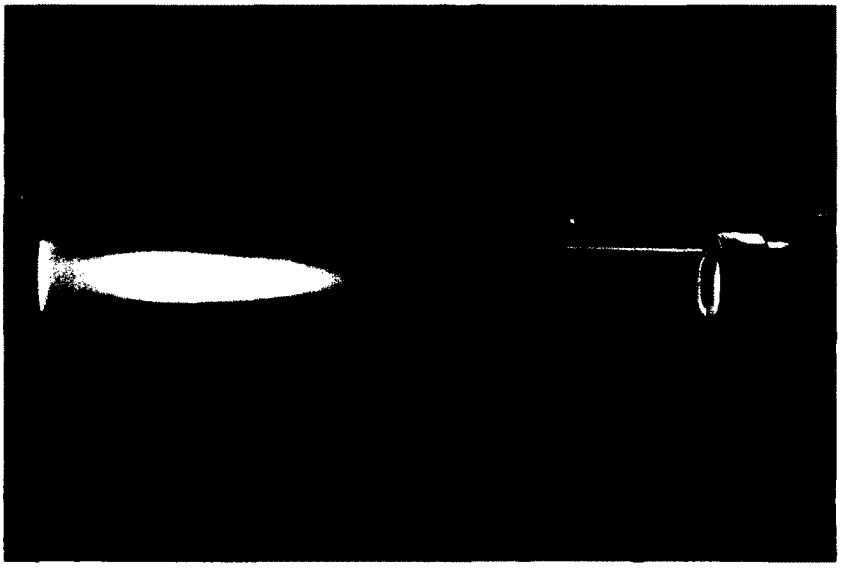

FIG. 17. Picture of the plasmoid in the afterglow region of an Ar discharge.

is a convenient object to develop techniques for diagnostics of inhomogeneous plasmas with limited symmetry. This geometric configuration is a usual feature of plasmas generated in the curved-shaped resonant SRF cavities. Therefore, the plasmoid may serve as a useful test bed for diagnostic and validation study of asymmetric plasma object.

Microwave resonant cavity

In this experiment a cylindrical resonant cavity was used to sustain a pulsed repetitive discharge. The main property of cylindrical resonant cavities is that Maxwell equations for electric (E) and magnetic (B) field together with the boundary conditions on E and B at the surface of the cylinder pose a constraint on the EM frequencies with respect to the cavity dimensions [33]. In other words, for a given cavity dimensions only a certain resonant frequencies will be allowed. Furthermore, resonant cavities with discrete frequencies of oscillation have a definite field configuration for each resonant frequency. This implies that, in order to excite a particular mode of oscillation in a cavity, the exciting frequency has to be exactly equal to the resonant frequency. Otherwise, no EM fields could be built up.

For the cavity operating in TE mode this relationship is

$$\omega_{mnp} = \frac{1}{\sqrt{\mu\epsilon}}\sqrt{\frac{x_{mn}^2}{r^2} + \frac{p^2\pi^2}{d^2}}, \tag{67}$$

where $m, p = 0, 1, 2, ...$, $n = 1, 2, 3, ...$, μ is the permeability of the material, ϵ is the permittivity of the material, r is the inner radius of the cavity, d is the length of the cavity, x_{mn} is the n^{th} root of the equation $J_m(x) = 0$, and $J_m(x)$ is the m^{th} order Bessel function that satisfies the boundary conditions for the cavity.

This cavity was designed to operate in the lowest TE mode, TE_{111} mode. This means that the first root of the first order Bessel function $J_1(x) = 0$, is $x_{11} = 1.84$. The inner radius of the cavity was $r = 0.037$ m. The cavity length was about $d = 0.25$ m with possibility for fine adjustments by using the detuning rods positioned at the end walls of the cavity. After placing these values into the right hand side of the Eq. (67) we get the resonant frequency $\omega_{111} = 2.45$ GHz, the exact match with the MW S-band exciting frequency.

Since the cavity is an imperfect conductor, the microwave energy can be dissipated in the cavity walls in a number of ways, as discussed in [34]. The most common loss mechanism in the MW cavity is heat transfer. A measure of the rate at which a vibrating system dissipates its energy into heat is called a quality factor or a Q factor. In an optical resonance cavity, the Q factor is defined as the ratio of the energy stored in the cavity (U) to the power dissipated by the cavity (P) times the resonance frequency,

$$Q = \omega_{111}\frac{U}{P}. \tag{68}$$

The complete derivation of the Q factor for the cylindrical resonant cavity is given in [33] and has the form of

$$Q = \frac{\mu_0}{\mu_c}\frac{d}{\delta}\frac{1}{2(1+\epsilon_\lambda\frac{Cd}{4A})}. \tag{69}$$

Here μ_0 is the permeability of free space, μ_c is the permeability of the cavity walls, A is the cross sectional area of the cavity, C is the circumference of the cavity, ϵ_λ is a dimensionless number on the order of unity for TE modes, and δ is the skin depth defined as

$$\delta = \sqrt{\frac{\rho}{\pi\omega_{111}\mu_c}} = 1.6\,\mu\text{m}, \tag{70}$$

where ρ is the resistivity of the cavity wall material. The cavity in our experiment was constructed from aluminium with resistivity $\rho = 2.65\ \mu\Omega\cdot$cm and permeability $\mu_c = \mu_0 = 4\pi \times 10^{-7}$ H/m.

In the case of cylindrical cavity $C = 2r\pi$, $A = r^2\pi$, and Eq. (69) becomes

$$Q = \frac{d}{\delta}\frac{1}{2(1+\epsilon_\lambda\frac{d}{2r})} = 1.1 \times 10^4. \tag{71}$$

In the case of normal conducting microwave cavities, quality factor of $Q \sim 10^4$ provides good stability and high power range of the cavity.

Supersonic flow

Supersonic flow in this experiment was sustained by a cylindrical convergent-divergent De Laval nozzle, as shown in Fig. 18. This is an optimally shaped nozzle that produces a flow at the exit with a constant Mach number, providing in that way the constant gas density and temperature at all post-nozzle points [35].

The working mechanism of the De Laval nozzle is based on the continuity equation for fluids which connects the density ρ, the cross-sectional area A, and the velocity v of the flow at two different points,

$$\rho_1 A_1 v_1 = \rho_2 A_2 v_2. \tag{72}$$

In most cases gas density varies very slowly throughout the flow. As the area decreases in the first convergent part of the nozzle, the velocity must increase at a similar rate causing the flow to accelerate to a Mach speed at the nozzle throat. After leaving the throat of the nozzle, the diameter of the divergent section of the nozzle increases very rapidly causing the sufficient pressure drop across the nozzle making

FIG. 18. Scheme of the cylindrical convergent-divergent nozzle.

a supersonic flow (Mach>1) possible. In order to maintain the acceleration in both parts of the nozzle, the flow at the nozzle throat needs to be equal to Mach 1.

The Mach number (M) is defined as

$$M = \frac{v}{v_s}, \tag{73}$$

where v is the speed of the flow and v_s is the speed of sound. By assuming that the gas flow is close to an ideal gas with no heat exchange with the nozzle walls, the speed of sound is defined as [36]

$$v_s = \sqrt{\gamma \frac{p}{\rho}} = \sqrt{\gamma RT}, \tag{74}$$

where p is the pressure, R is the specific gas constant, T is the temperature, and $\gamma = C_p/C_v$ is the specific heat ratio given as the ratio between the specific heat at constant pressure (C_p) and specific heat at constant volume (C_v).

The convergent-divergent nozzle used in this study was manufactured from unfired Hydrous Aluminum Silicate (Grade "A" Lava) since Lava is MW transparent. The gas inside the nozzle was pure Ar with characteristics: $R = 208$ J K^{-1}mol^{-1} and $\gamma = 1.67$ and at temperature of approximatively $T = 300$ K, thus leading to $v_s \cong 320$ m/s.

Also, after combining Eq. (72), the ideal gas equation, and the energy equation with constant heat transfer a very useful relationship between the ratio of total to static pressure and a Mach number at a given point is obtained,

$$\frac{p_0}{p} = \left(1 + \frac{\gamma - 1}{2} M^2\right)^{\gamma/(\gamma-1)}, \tag{75}$$

where static pressure (p_0) is the pressure of the stationary gas and total pressure (p) is the pressure a flowing gas exerts as it is brought to a stop.

The argon gas in our experiment is considered to be nearly stationary in the pre-nozzle section, allowing us to assume that inlet pressure is equal to static pressure, $p_{in} = p_0$. Hence, Eq. (75) can be rewritten as

$$M = \sqrt{\frac{\left(\frac{p_{in}}{p_{out}}\right)^{(\gamma-1)/\gamma} - 1}{(\gamma - 1)/2}}, \tag{76}$$

where p_{out} is total pressure measured at the exit pressure point in the experiment.

Figure 19 shows the Mach number dependance on the exit pressure in a pure argon flow. It seems that as the exit pressure increases, the Mach number also increases until it reaches a steady state at pressure values above 3.5 Torr. The average Mach number above 3.5 Torr is determined to be 2.30±0.07. The error reflects the uncertainty in measuring the inlet and exit pressures.

The fact that the gas flow is Mach 1 at the throat of the De Laval nozzle can be used to obtain the ratio of exit-to-nozzle throat cross-sectional area as a function of the Mach number

$$\frac{A_{out}}{A_{th}} = \frac{1}{M}\left[\frac{2}{\gamma + 1}\left(1 + \frac{\gamma - 1}{2} M^2\right)\right]^{(\gamma+1)/2(\gamma-1)}, \tag{77}$$

where A_{out} is the exit and A_{th} is the nozzle throat cross-sectional area. The inner radius at the throat of our nozzle was $r_{th} = 3.5$ mm and at the exit was $r_{out} = 14.05$ mm meaning that $A_{th} = 27.1$ mm^2 and $A_{out} = 619.8$ mm^2. Based on this nozzle geometry and the Eq. (77) we have calculated Mach number to be $M = 6$. The difference between the theoretical prediction (77) and the experimentally obtained Mach number values (76) is most likely due to the fact that Eq. (77) is valid only in the case of laminar gas flow. It seems that the argon in our experiment exerts turbulent gas flow due to the surface imperfections of the nozzle. Moreover, there is a good possibility that the sonic flow of Mach 1 was achieved beyond the nozzle

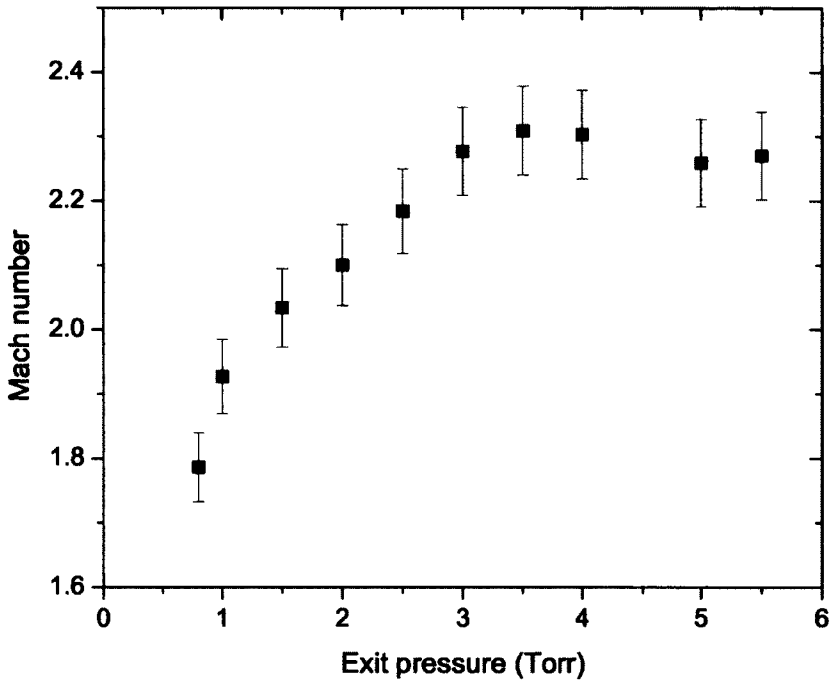

FIG. 19. Mach number as a function of the exit pressure in the MW cavity in a pure Ar flow measured in this work.

throat, implying that the convergent-divergent nozzle used in our experiment differs from the De Laval nozzle. Thus, applying Eq. (77) for Mach number determination would introduce additional error.

3.1.2 MEASUREMENT METHODS

We have employed optical emission spectroscopy (OES) since it is simple, non-intrusive, and *in situ*. We have also employed laser induced fluorescence (LIF) in order to obtain information on the plasma system and to increase the overall measurement precision.

Optical emission spectroscopy

We used OES as our primary diagnostic tool to observe the spectra of the Ar excited states by measuring photons emitted from the plasma. Data were collected

in two regimes: time averaged, spatially resolved regime and time resolved, spatially averaged regime. Spatially resolved emission spectra were recorded using two different detection systems, an imaging spectrograph (Acton SpectraPro) connected to the charged-coupled device (CCD) camera (Apogee, Hamamatsu, Back-Illum) and a compact wide range spectrometer (Ocean Optics HR4000CG) with the in-built CCD array detector (Toshiba). All measurements were conducted over the 500 ms exposure time, making it very difficult to depict the effects of the turbulent gas flow.

As a consequence, we collected data in the time resolved regime by employing an imaging spectrograph (Acton SP2750) in conjunction with the high precision intensified CCD camera (Princeton Instruments, PI MAX3) which allowed us to resolve spectra from the plasma on the microsecond time scale.

The observed spectra were calibrated using a Newport/Oriel absolute black body irradiance source which has predefined relationship between the wavelength (λ) and the spectral irradiance (I) given as,

$$I = \lambda^{-5} e^{A+\frac{B}{\lambda}} (C + \frac{D}{\lambda} + \frac{E}{\lambda^2} + \frac{F}{\lambda^3} + \frac{G}{\lambda^4}), \tag{78}$$

where the coefficients are provided by the manufacturer

$$\text{A} = 41.485337541901$$

$$\text{B} = -4899.978599767823$$

$$\text{C} = 0.821306420331086$$

$$\text{D} = 428.610013779565$$

$$\text{E} = -317020.290823792$$

$$\text{F} = 85820275.9042372$$

$$\text{G} = -8493841443.25663.$$

Spectral irradiance represents the power of electromagnetic radiation per unit area incident on a surface at a specific frequency, and has the units of [$\text{Wm}^{-2}\text{nm}^{-1}$]. Irradiance per count of the black body radiation is estimated by dividing the irradiance calculated using Eq. (78) with the number of counts measured with the CCD camera. We evaluated the calibration graphs of spectral irradiance per count versus wavelength in the spectral range between 200-1100 nm. Using these graphs we have

determined the population of particular Ar excited state transitions in the following way.

First, we have obtained spectral irradiance of a desired spectral line by multiplying the intensity of the measured spectral line by the irradiance per count of the black body radiation for corresponding wavelength. Then, we have introduced the length of plasma region and expressed the spectral irradiance in the terms of radiometric quantities (P_λ) with units of [$\mathrm{Wcm^{-3}nm^{-1}}$]. This was achieved by dividing the irradiance by the plasma length. The next step was to convert radiometric to photon quantities by calculating the number of photons in a joule of monochromatic light of wavelength λ given as,

$$N_{p,\lambda} = \frac{1}{E} = \frac{\lambda}{hc} = \lambda \times 5.03 \times 10^{15} \left[\frac{\mathrm{ph}}{\mathrm{J^{-1}}}\right], \tag{79}$$

where E is the energy of one photon, $h = 6.26 \times 10^{-34}$ J·s is the Planck's constant, and $c = 3 \times 10^8$ m/s is the speed of light. Consequently, we have determined the $N_{p,\lambda}$ photons per second which corresponded to one Watt of radiation at λ employing the general expression,

$$\frac{\mathrm{d}N_{p,\lambda}}{\mathrm{d}t} = P_\lambda \cdot \lambda \cdot 5.03 \times 10^{15} \left[\frac{\mathrm{ph}}{\mathrm{cm^3 \cdot s}}\right]. \tag{80}$$

Finally, the population density of the upper energy level (N_u) could be expressed as

$$N_u = \frac{\mathrm{d}N_{p,\lambda}/\mathrm{d}t}{A_{ul} \cdot g_u} \left[\frac{1}{\mathrm{cm^3}}\right], \tag{81}$$

where A_{ul} is the transition probability expressed in $\mathrm{s^{-1}}$ and g_u is the statistical weight of the upper excited state.

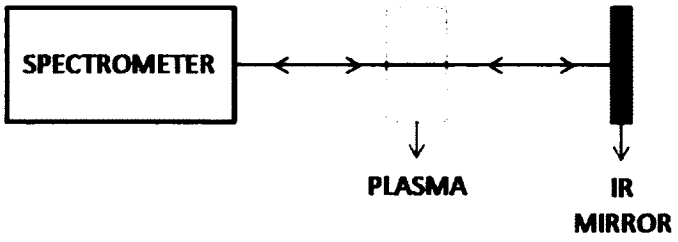

FIG. 20. Experimental setup for test of optical thickness.

By using a standard back reflector procedure we have eliminated the possibility that the optical thickness of measured spectral line intensity was interfering with our measurements [37]. If the optical thickness is increased, a part of the spontaneously emitted radiation is likely to be reabsorbed inside the plasma region. The decrease in the effective radiative decay due to the repeated absorption and emission of photons is referred as radiation trapping. To confirm that there was no presence of self

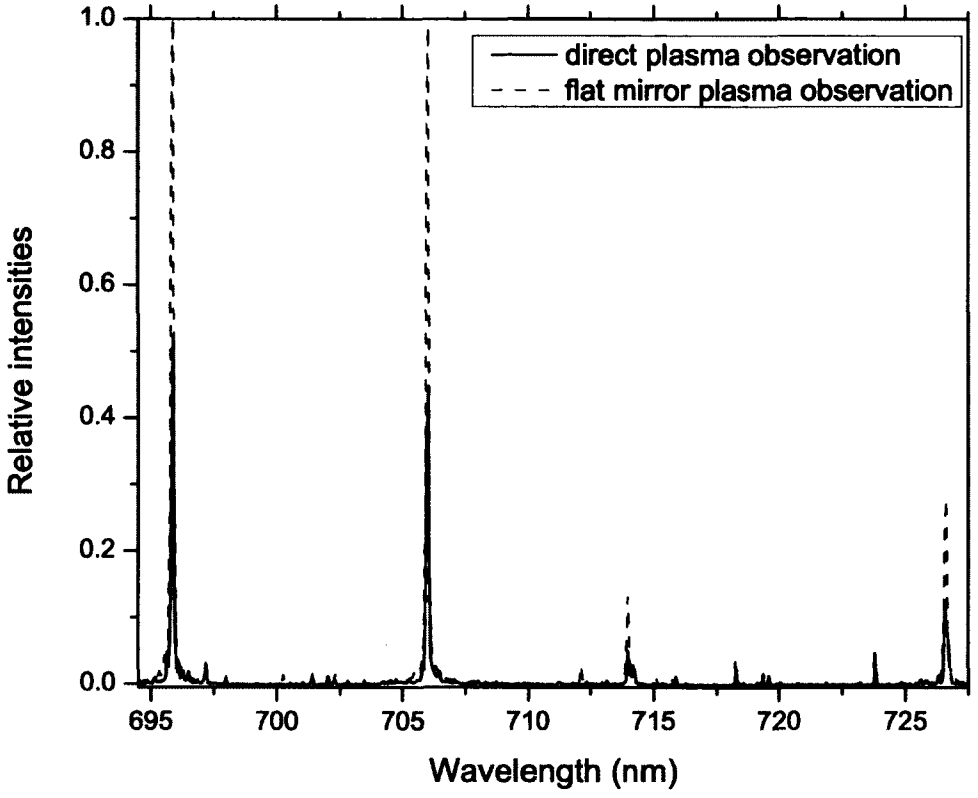

FIG. 21. Spectral line intensities measured using a direct plasma observation and using a flat reflective mirror.

absorption of spectral lines due to the radiation trapping, we have placed a flat mirror that reflects infra-red (IR) light at 180^0 in the spectrometer's line of sight, see Fig. 20. The optical thickness of the spectral line could be measured by comparing line intensities with and without a mirror. If optical depth of plasma is small, emitted

light from plasma reflects from the mirror and passes through plasma with negligible absorption on its way back. The spectrometer then detects twice the line intensity. It can be seen from Fig. 21 that in our case all spectral line intensities were higher by a factor of two in comparison to the direct plasma observation. Therefore, we declared that plasma was optically thin and the radiation trapping along the observation path could be neglected.

All spectral measurements were performed side-on with respect to the direction of the discharge flow. A detailed description on how a spatial and time resolution were obtained is given in the following sections.

a) Spatial resolution - Plasma tomography

We have employed plasma tomography method, described in the following chapter, to obtain the spatial distributions of plasma parameters (population densities, excitation temperatures). In order to apply this technique, plasma needs to be observed from every angle all around. The common approach to achieve this is to rotate the detecting system around plasma object and collect data at different angles. The field of medical diagnostics adopted this approach and has been the driving force behind this research area for many decades now. However, in laboratory conditions it is more convenient to keep the detecting system (spectrometer with camera) fixed at one position, and to collect light emitted from plasma at different angles by using a rotating mirror instead.

This is achieved by applying simple rules of trigonometry, as shown in Fig. 22. It could be seen that in order to collect light emitted from plasma at an angle α, the mirror needs to be a distance d from plasma, such that

$$\tan\alpha = \frac{h}{d} \Rightarrow d = \frac{h}{\tan\alpha}, \tag{82}$$

where mirror is at height h from the center of the plasma object and $\alpha < 90^0$, see Fig. 22a. Also, it could be deduced from the figure that the mirror should be inclined at an angle $\theta = \alpha/2$ with respect to the observation axis of the detector. Thus,

$$d = \frac{h}{\tan 2\theta}. \tag{83}$$

In Fig. 22b is illustrated the case with $\alpha > 90^0$. In this case mirror should be at

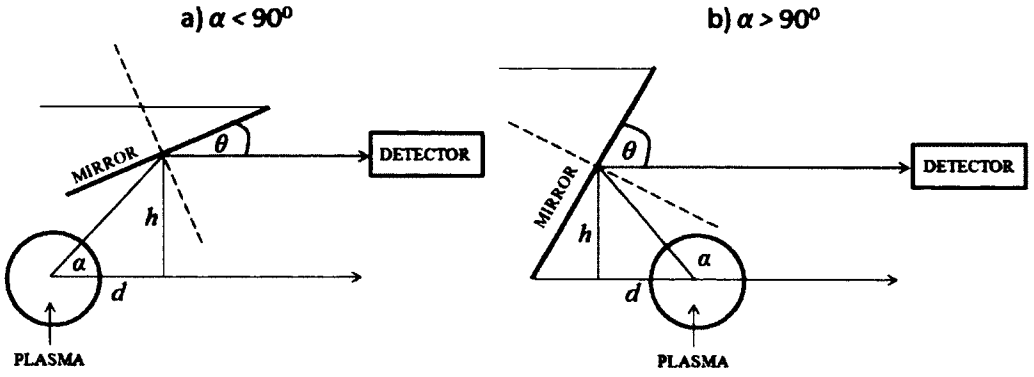

FIG. 22. Scheme of a set-up used for spatial measurements: a) $\alpha < 90^0$ and b) $\alpha > 90^0$.

distance

$$d = \frac{h}{\tan(\pi - \alpha)} = -\frac{h}{\tan 2\theta}. \tag{84}$$

To achieve scanning of the plasma, we have built an automated measurement system (AMS). It consists of a flat mirror and a set of feedback sensors connected to two high-precision stepper motors driven by a microcontroller-based system, as shown in Fig. 23. The precision of the selected bi-polar stepper motors, with up to 400 steps per revolution, allowed for a position sub-millimeter and angular sub-degree control of the mirror's orientation with respect to the plasmoid. Each motor was connected to a rotational encoder wheel, which provided rotational-position feedback to the controller. Additionally, the distance of the mirror from the quartz tube was measured by a linear sliding potentiometer, and the absolute angle of the mirror was measured by a triple axis accelerometer (Analog Devices ADXL335). Once the motors and sensors were connected to the rotational and translational knobs of the mirror platform they were calibrated by visual inspection using a laser set-up. The motors were driven by a Microstepping Driver with Translator (Allegro MicroSystems A3967SLB), connected to an 8-bit microcontroller (Atmel AVR ATmega328). The microcontroller was connected, as a master, to a host computer via a USB serially emulated interface. The host computer was programmed to manage the microcontroller, motors, and sensors, and to automate the measuring tasks.

By changing the angle and the position of the mirror we were able to reflect

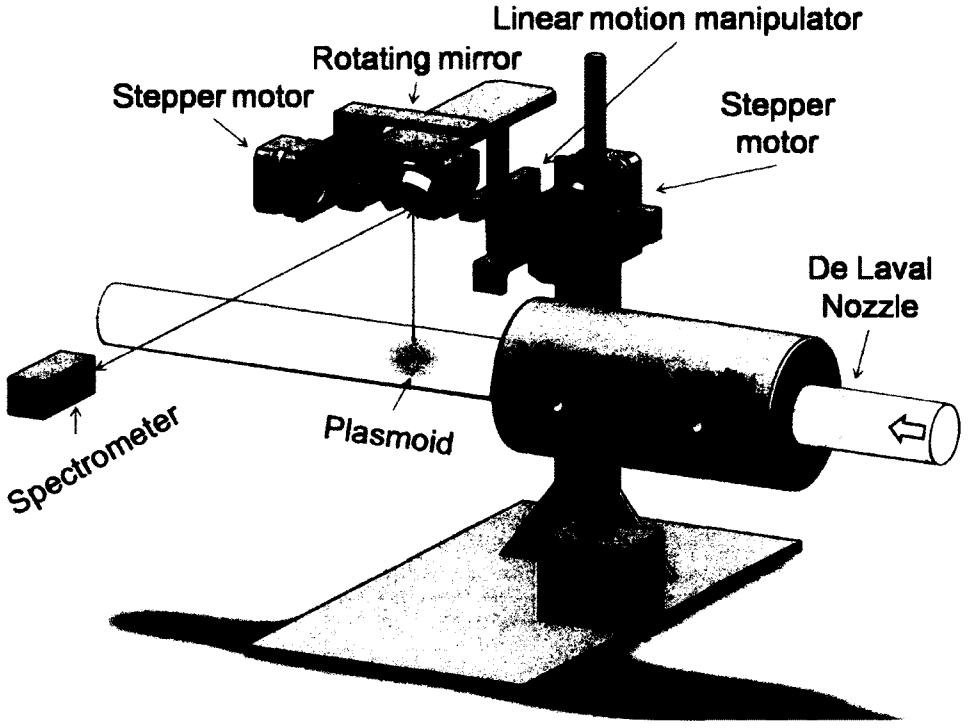

FIG. 23. Scheme of automated measurement system.

the emitted light perpendicular to the spectrometer, which allowed us to keep the detecting system at a fixed position. The measurements were taken at three different positions from the cylindrical cavity, which corresponded to both ends and the mid section of the plasmoid. This experimental set-up allowed us to record projections at 21 angles in the range from 48 to 168 degrees and 17 projections for each angle, with the sampling rate of 0.2 cm across the diameter of the quartz tube.

b) Time resolution

As it was already stated at the beginning of the chapter, the supersonic discharge in this experiment was sustained by using the commercial MW generator powered on the US power electrical grid. The power signal was a 120 volts RMS (root mean square) sine wave operating at $\nu = 60$ Hz frequency, shown in Fig. 24a. In order to obtain time-resolved Ar I spectra, it was necessary to synchronize the detecting

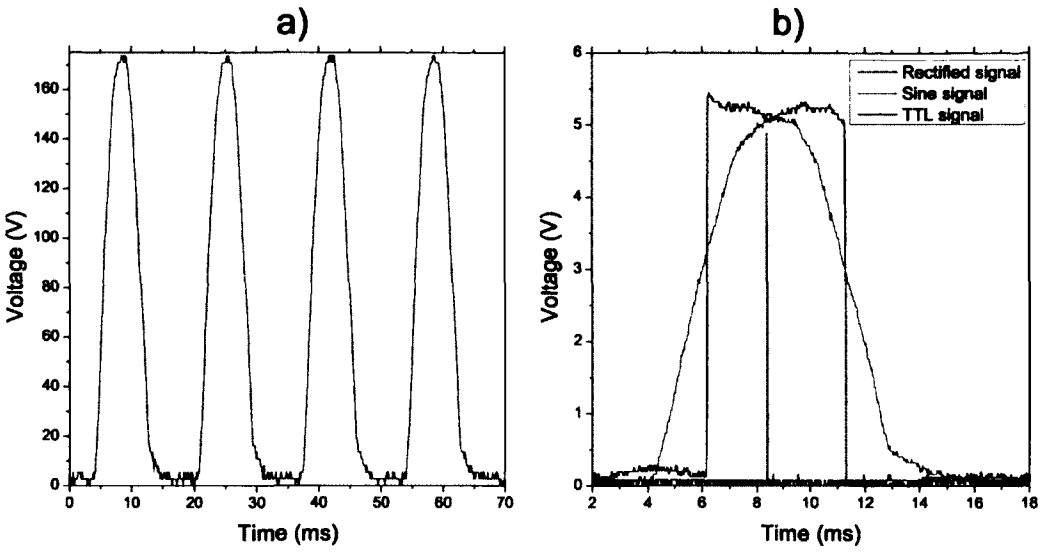

FIG. 24. Power signal: a) at 120 V RMS (169.7 V peak value) and at frequency of 60 Hz that is equivalent to period $T = \frac{1}{\nu} = 16$ ms and b) time synchronization between the input power signal and the detecting system.

system (CCD camera) with the sine power signal using a transistor-transistor logic (TTL) pulse wave, as shown in Fig. 24b. We have also synchronized the pulse of a tunable dye laser with this device to perform time-resolved laser induced fluorescence.

We observed the time change of the Ar I population densities by measuring the spectral line intensities at different times during the sine signal. For that purpose, we have built a time synchronizing device, shown in Fig. 25, by following these steps. First, we reduced the signal voltage from $V = 120$ V to $V_2 = 5$ V by using two resistors, $R_1 = 1$ MΩ and $R_2 = 40$ kΩ connected in series. Employing Ohm's law for electrical circuits we derived

$$V_2 = V\frac{R_2}{R_1 + R_2} \approx 5\text{V}. \tag{85}$$

Second, we have employed a signal inverter (74LS04) in parallel with a microcontroller (Arduino) to invert and rectify the sine signal. Finally, the Arduino microcontroler emitted a transistor-transistor logic (TTL) 15 μs pulse wave to trigger the ICCD camera at a proper time, shown in Fig. 24b. The ICCD camera was then used to collect data during the 20 μs time frame. In order to reduce the signal-to-noise

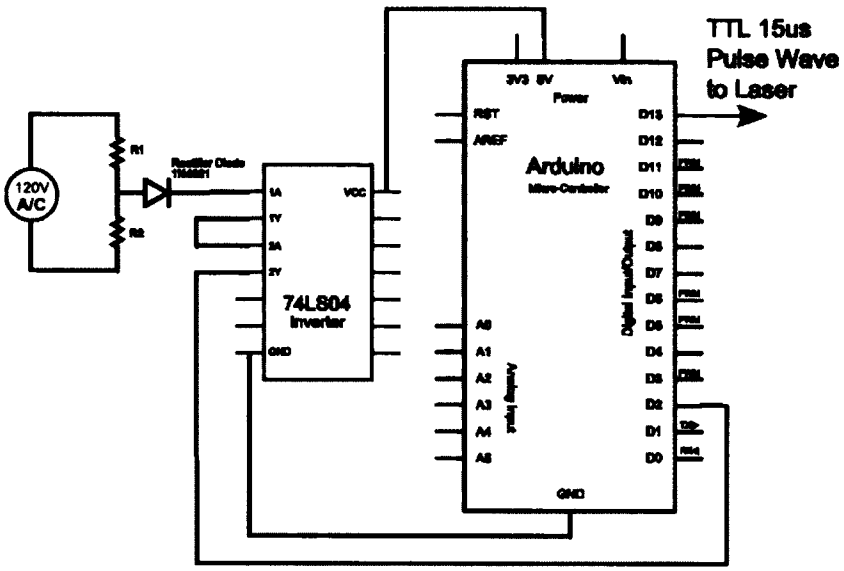

FIG. 25. Scheme of time synchronization device.

ratio we have recorded 200 spectra per each exposure time.

Laser diagnostics

Optical emission spectroscopy allowed us to determine a number of plasma parameters, most importantly population densities of Ar I $4p$ levels. However, obtaining population densities of the lowest energy excited Ar I $4s$ levels requires a different optical measurement technique based on laser photon spectroscopy. A good candidate is a laser induced fluorescence since the difference in spectral line intensities when the system is pumped by a laser and without a laser is directly proportional to the population densities of the $4s$ states.

The first step in the development of laser diagnostics is the laser itself. Therefore, we have built a tunable dye laser. Dye lasers were discovered independently by P. P. Sorokin and F. P. Schäfer in 1966 [38, 39], and they represented a dream come true in laser science: to have a laser easily tunable over the range of frequencies and wavelengths. A dye laser is a laser that consists of a dye mixed with a dye solvent, which may be circulated through a dye cell. The dye solution is usually circulated at high speeds to avoid the degradation of the dye. Besides the dye cell, the basic laser

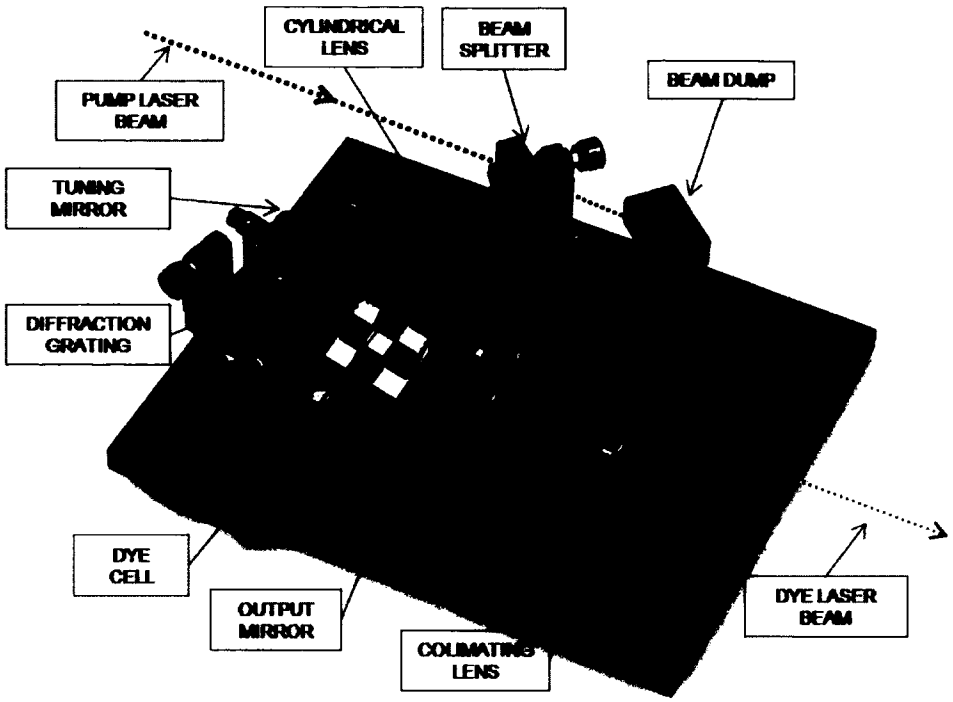

FIG. 26. 3D scheme of the tunable dye laser used in our experiment.

cavity often includes a diffraction grating, a tuning reflective mirror, and an output mirror. The laser system is generally radiation pumped either by a flash lamp or by another laser. We have chosen laser pumping since it provides better beam quality and spectral characteristics.

In Fig. 26 the schematics of optical components of the dye laser are presented. For better understanding of the laser design in Fig. 27 we show a top view diagram of the laser optical path. As can be seen, the dye laser is pumped by a pulsed NdYag laser (Continuum, Minilite Series) operating at 532 nm (green light). The laser light is vertically polarized with the beam diameter of 3 mm and 3-5 ns pulse width. Repetition rate of the laser is set to $f = 10$ Hz and the average power is $P = 45$ mW, leading to single pulse energy of $J = 4.5$ mJ.

The green light intensity is reduced by dividing the beam by a glass beam splitter.

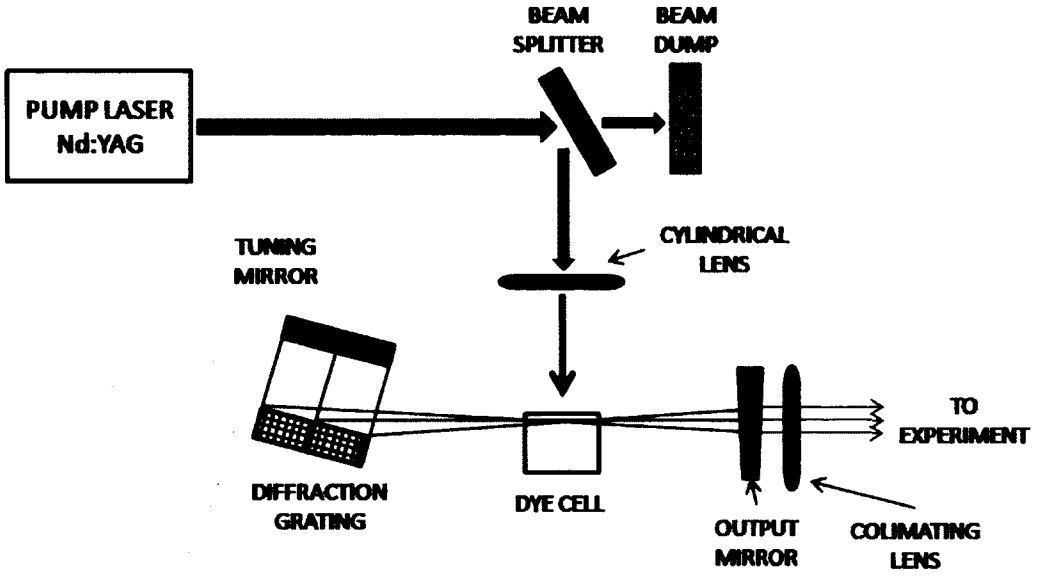

FIG. 27. 2D scheme of the tunable dye laser used in our experiment.

One component of the beam is directed to the beam dump, while the other component is focused to a narrow strip by a 50 mm plano-convex cylindrical lens. A laser dye (LDS 722 also called a PYRIDINE 2) with molecular formula $C_{19}H_{23}N_2ClO_4$ and molecular mass $M = 378.86$ g/mol is used to tune the laser light in the wavelength range 686-795 nm with a center wavelength at $\lambda = 722$ nm. Methanol is used as a solvent for the dye. The laser dye is placed in a dye cell (NSG Precision Cells) that is pumped by a Micropump motor combined with a TF series filter (Dibert Valve & Fitting Co).

The laser light is then fine-tuned by employing a wavelength-selective resonator. In this study we have used a diffraction grating at grazing incidence in combination with a maximum reflectivity mirror [38,40], as shown in Fig. 27. Grazing incidence is a simple and inexpensive optical configuration developed by Littman and Metcalf [40], where a diffraction grating is positioned so that laser radiation strikes the grating almost perpendicular to the grating normal. In this arrangement a relatively large area of the grating is illuminated by the laser beam, increasing angular dispersion and resolving laser power significantly. Furthermore, the damage of the grating by high power lasers is prevented without using additional beam expanding devices.

The laser cavity is closed with a 8% reflecting wedged output coupler combined with a 1 m collimating lens that focuses the laser beam in front of the quartz tube containing MW discharge. The distance between output coupler and dye cell does not affect the laser efficiency significantly. On the other hand, the tuning mirror should be placed close to the cell (1-5 cm) for better laser operation [40].

In our experiment, the power output of the tunable dye laser was $P_{laser} = 300$ μW which implied the laser energy of $J_{laser} = 30$ μJ. The laser beam was 5 mm in diameter. Thus, the energy density was

$$I_{\omega} = \frac{J_{laser}}{d_{laser}^2 \pi} = 1.5 \cdot 10^{-4} \text{ J/cm}^2, \tag{86}$$

small enough not to disturb plasma and modify plasma properties while taking data.

It should be noted that the pump laser was synchronized with the power supply and the ICCD camera using the synchronization device described in the previous section. At a specific time the TTL signal from the synchronization device was sent to the pump laser. After laser shot was fired toward plasma, another TTL signal directed from laser ignited the ICCD camera which in turn recorded spectral data in 20 μs exposure time.

3.2 PULSE-REPETITIVE MICROWAVE DISCHARGE IN AIR

Supersonic MW discharge in Ar, described above, provides information on atomic plasma structure. Separately, a pulse-repetitive microwave discharge in air was used to study the behaviour of molecular structures in MW plasmas. Experiment was conducted in a static plasma cell, shown in Fig. 28, evacuated to the background air pressure of the order of 100 mTorr. A surface plasma was generated at the aperture of a rectangular horn antenna with a pulsed microwave source operating in the X-band (9.5 GHz, 210 KW) spectral range. The microwave discharge was obtained in air at pressures above 10 Torr. A detailed description of the microwave plasma experiment is given in Ref. [41].

FIG. 28. Photography of laboratory cell showing the microwave horn with the ceramic aperture cover plate.

Spectral data were taken both end-on and side-on, as shown schematically in Fig.

29. This approach was necessary due to the possible existence of self-absorption effects when discharge was observed only side-on. The surface discharge at the aperture of the horn antenna was patterned in bright and dark patches, reflecting the mode structure of the microwave beam at the aperture of the horn [41]. Due to the mode structure, the electric field distribution was undulatory, with four periods covering the E-field side of the horn.

Emission spectra were recorded using a 0.5-m Acton Research Corporation imaging spectrograph connected to the Apogee spectral imaging cameras with Hamamatsu CCD and Tektronix CCD detectors. Another camera, from Stanford Computer Optics, Inc., was used to observe the discharge in gated format with time resolution of 50 ns. Alternatively, transient signals at fixed wavelengths were recorded using a photomultiplier tube.

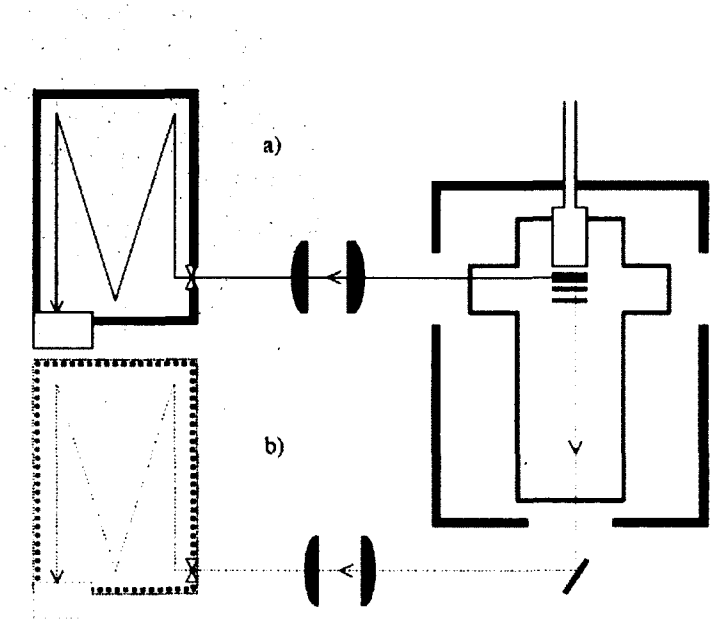

FIG. 29. Scheme of imaging spectrometer arrangement: a) side-on and b) end-on observations.

The observed spectra were calibrated using an absolute Edgerton, Germeshausen, and Grier, Inc. (EEG) black body irradiance source. Calibration graphs of spectral

irradiance per count versus wavelength were evaluated for the wavelengths between 250-1000 nm for three spectrometer gratings. We determined the populations of the upper level from particular excited state transitions by using these graphs. The statistical error was only 10% due to low temperature of the calibration source for the spectral range used in present work.

Time-resolved emission from the microwave discharge plasma was recorded at a specific wavelength with a photomultiplier tube attached to the second exit slit of the spectrograph and connected to a digital oscilloscope. Waveforms from 1-3 pulses in a sequence could be recorded on a single oscilloscope data file. It allowed us to record the waveforms of population density of a particular N_2 ($C^3\Pi_u$) state. We were also able to record the waveforms of forward and reflected power signal. To calculate the total input power we relied on the nominal peak power of P_{peak} = 210 kW and assumed a homogeneous distribution over the horn aperture area. This decision was made because the actual variation of the electric field around the breakdown is relatively small and does not affect the amplitude of the reduced electric field. The X-band pyramidal horn (Z) aperture [42] was (5.9×7.8) cm^2. Averaged peak power density at the aperture was therefore

$$P_{ave} = \frac{210\,kW}{5.9 \times 7.8\,cm^2} = 4.6\frac{kW}{cm^2}. \tag{87}$$

The average power per unit area transported by microwave intensity could be used to evaluate the space-average reduced electric field. Assuming the transmission network impedance, $Z = 50\ \Omega$ we have

$$E_{ave} = \sqrt{P_{ave} \times Z} \approx 478\frac{V}{cm}. \tag{88}$$

To conclude, measuring average power per unit area allowed us to determine not only actual reduced field but consequently electron temperature and rate coefficients for various processes in plasma.

CHAPTER 4

DIAGNOSTIC METHODS

The overall objective of plasma diagnostics is to gather information about the nature of the plasma derived from observations of physical processes and their effects. For this reason much effort has been devoted to devising, developing, and providing techniques for diagnosing the properties of plasma [6,8]. However, the diagnostics of non-stationary and chemically reactive MW plasmas have always presented a great challenge to researchers, mainly because the important plasma parameters vary over a wide range of conditions and their values affect observable quantities in complex ways. Additional problems arise from the time scale and spatial variations in most plasmas, which require sub-microsecond temporal and sub-millimeter space resolution. However, continuous development of novel instrumentation and techniques has an important impact on the diagnosing of these plasmas. In addition, due to their rich chemical activity, developing a kinetic model including all plasma particles (electrons, atoms/molecules, ions) presents a vital step and major challenge for in plasma diagnostics.

This chapter is divided into three sections categorized by the type of diagnostic technique applied. In the first section we will discuss different approaches, based on plasma tomography methods, to obtain spatial distributions of plasma parameters (population densities, excitation temperatures). Then in the second part of this chapter we will describe laser induced fluorescence diagnostic technique necessary in obtaining population densities of specific metastable and resonant atomic levels. And finally, we will complete the last section of this chapter with the time dependent kinetics of the argon and air plasmas. Specifically, we will define the main processes that affect the population rates of several Ar and N_2 excited states.

4.1 PLASMA TOMOGRAPHY

Optical emission spectroscopy (OES) is a useful tool as a non intrusive, *in situ* optical technique. But OES allow only measurements of integrated effects. In order to look into the internal dynamics of the discharge, the integrated data needs to be

transformed into the spatial population distributions. A commonly used method for reconstructing an inner plasma structure is plasma tomography, which serves as a magnifying glass to look at the internal dynamics of discharge without disturbing it. We have used the emission tomography, since the plasma is a strongly radiating object and the emission spectra could be recorded easily. Thus, there was no need for perturbing the system for the purpose of taking measurements.

We have developed a plasma tomography technique to be employed in supersonic flowing MW discharge experiment, described in Section 3.1. Since the discharge is maintained in the cylindrical quartz tube, see Fig. 17, it was possible to simplify the numerical integration for the case of cylindrical symmetry. Cross-sectional scheme of the cylindrical experimental set-up is given in Fig. 30.

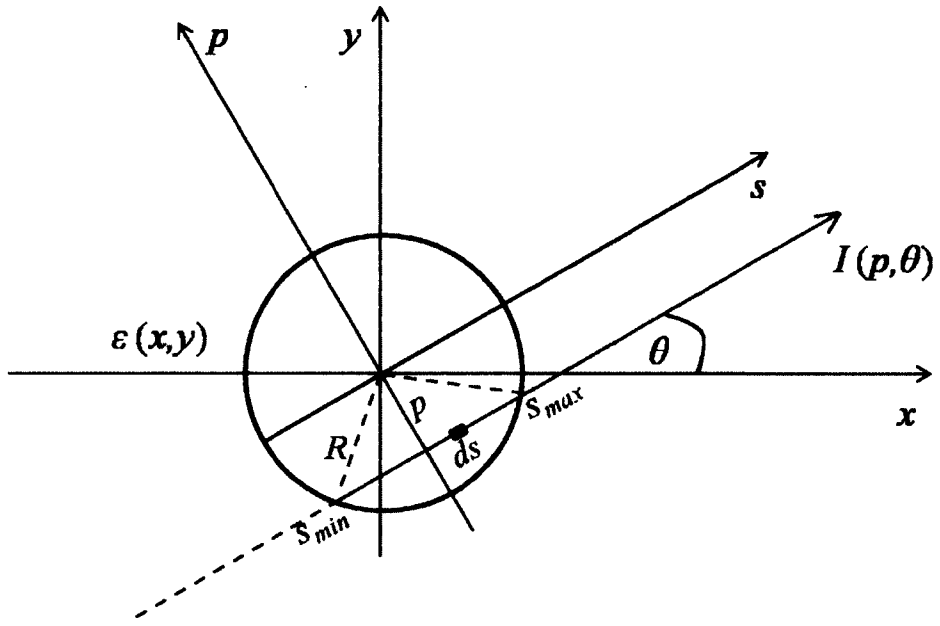

FIG. 30. Cross-sectional scheme of the experimental set-up for our cylindrical plasma tomography experiment.

Let us start by looking at light leaving plasma at an angle θ with respect to the x-axis of the coordinate system outlined in Fig. 30. To better visualize the problem,

it is useful to transfer to new coordinates s and p that are rotated by given angle θ with respect to x and y coordinates, as shown in Fig 30. Then,

$$\begin{aligned} s &= x\cos\theta + y\sin\theta \\ p &= -x\sin\theta + y\cos\theta. \end{aligned} \tag{89}$$

From Fig. 30 can be seen that the total light intensity, $I(p,\theta)$, emitted at an angle θ and distance p from the center of the plasma represents the sum of light intensities from all emitters (excited atoms and ions) aligned along a line parallel to s-axis. This effect was first studied by Johann Radon [15] who did show that for a large number of emitters the sum of line intensities becomes the line integral,

$$I(p,\theta) = \Re[\varepsilon(x,y)] = \int_L \varepsilon(x,y)\,\mathrm{d}s, \tag{90}$$

where L is the line of integration, ds is the increment of the length along that line, and $\varepsilon(x,y)$ is local emissivity from a small volume defined around the point (x,y). If $I(p,\theta)$ is known for all p and θ, then $\varepsilon(x,y)$ is in fact the two dimensional Radon transform. Equation (90) is, then, evaluated numerically by applying the Newton-Cotes quadrature numerical integration and with a good sampling technique of the input data.

We will test the validity of our numerical integration on the examples of Gaussian distribution function, shown in Fig. 31

$$\varepsilon_G(x,y) = \exp(-x^2 - y^2), \tag{91}$$

and parabolic distribution function, shown in Fig. 32

$$\varepsilon_P(x,y) = x^2 + y^2. \tag{92}$$

We have chosen these two functions because they are integrable and have no singularities on L and their Radon transform gives an analytical solution. Moreover, the shape of the parabolic distribution function resembles the shape of plasma driven by surface electromagnetic wave, and provides a convenient comparison between the test function and the experimental data. In order visualise the resemblance with the experimental set-up, both functions were generated in the x and y range -1.6 to 1.6 of arbitrary units (a.u.), which corresponds to the radius of the quartz tube ($R = 1.6$ cm), given in Section 3.1. Furthermore, for better comparison with the quartz tube

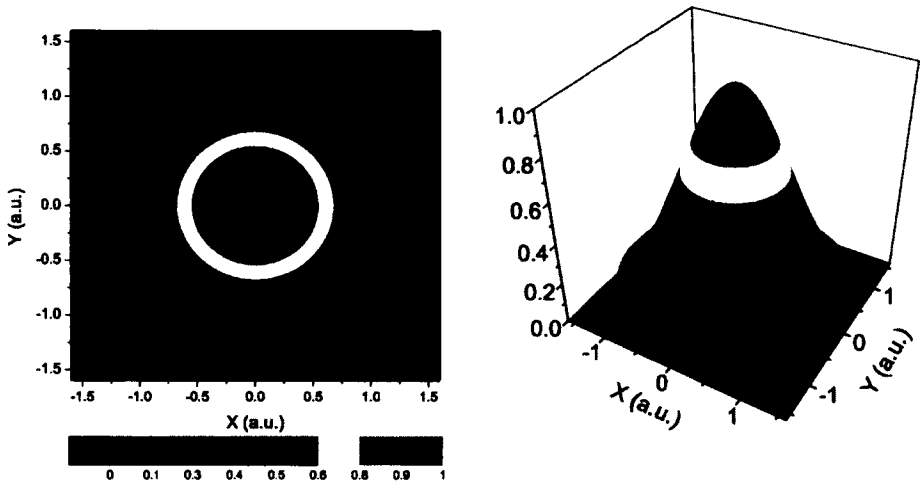

FIG. 31. The two dimensional Gaussian distribution function given as $\varepsilon_G(x,y) = \exp(-x^2 - y^2)$.

cylindrical geometry, the function values were set to zero outside the circle of radius $R = 1.6$ a.u.

Using the coordinate transformation, Eq. (89), we can easily show that $x^2 + y^2 = s^2 + p^2$. Radon transform of Gaussian distribution function then becomes

$$\begin{aligned} f_G(p,\theta) &= \int_{-\infty}^{\infty} \exp(-p^2 - s^2)\, ds \\ &= \exp(-p^2) \int_{-\infty}^{\infty} \exp(-s^2)\, ds \\ &= \sqrt{\pi}\exp(-p^2). \end{aligned} \tag{93}$$

The comparison between numerically obtained and analytically calculated values of the $I(p,\theta)$ of the Gaussian distribution function by using the Eq. (90) is given in Fig. 33. The results show excellent agreement except for the minor noise discrepancies arisen from the numerical error.

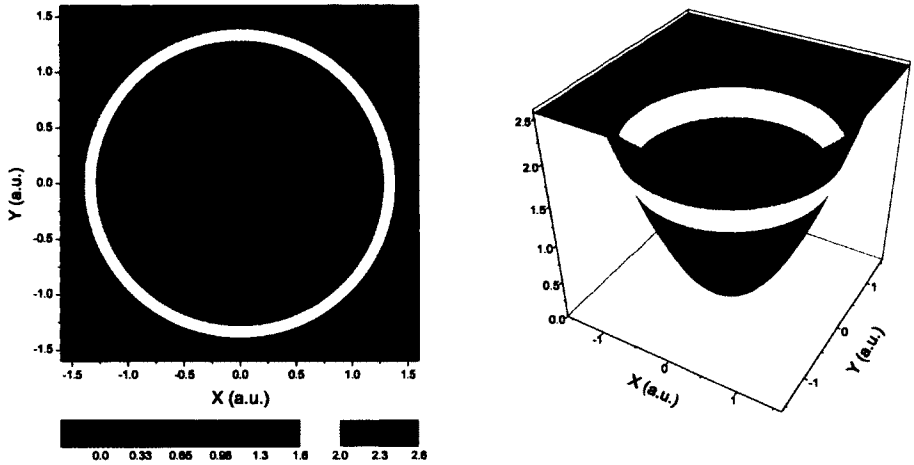

FIG. 32. The two dimensional parabolic distribution function given as $\varepsilon_P(x,y) = x^2 + y^2$.

Radon transform of parabolic distribution function Eq. (92), $\varepsilon_P(x,y) = x^2 + y^2$, has also an analytical solution,

$$f_P(p,\theta) = \int_{-\infty}^{\infty} (p^2 + s^2)\,\mathrm{d}s = \int_{s_{min}}^{s_{max}} (p^2 + s^2)\,ds \tag{94}$$
$$= 2\int_{0}^{s_{max}} (p^2 + s^2)\,ds$$
$$= 2p^2 s_{max} + \frac{2}{3}s_{max}^3,$$

where $s_{max} = -s_{min} = \sqrt{R^2 - p^2}$ and R is the radius of the quartz tube, as shown in Fig. 30. The use of limits s_{min} and s_{max} is justified by assuming that there aren't any emitters outside the walls of the quartz tube. As in the case of Gaussian distribution function, we have obtained very good agreement between numerical values and their analytical solutions, as shown in Fig. 34.

With good confidence in the numerical integration of the direct Radon transform

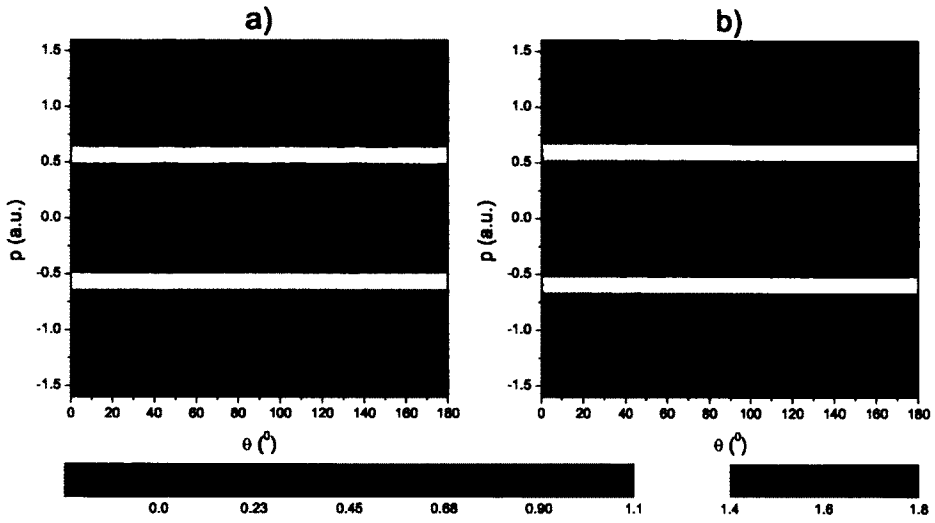

FIG. 33. The direct Radon transform of Gaussian distribution function: a) numerical solution using Newton-Cotes quadrature integration and b) analytical solution.

we can proceed to retrieve the spatial population distributions from this simulated spectral intensities by inverting the Radon integral,

$$\varepsilon(x, y) = \Re^{-1}[I(p, \theta)]. \tag{95}$$

Since our experiment was performed in the cylindrical geometry (both cavity and quartz tube were cylinders), as a first step in finding inverted Radon integral we have assumed that plasma was radially symmetric as the functions defined in Eqs. (91) and (92). In that case Radon integral transforms in its special case, the Abel integral.

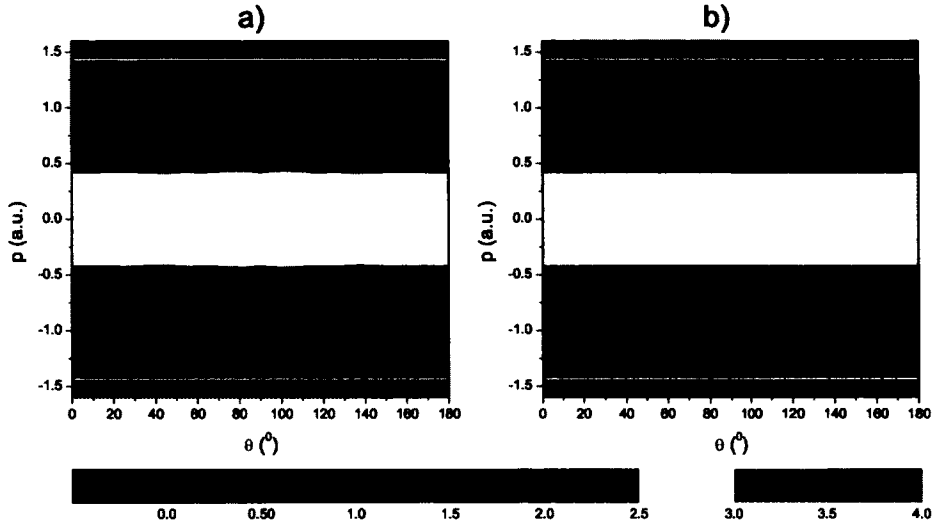

FIG. 34. The direct Radon transform of parabolic distribution function: a) numerical solution using Newton-Cotes quadrature integration and b) analytical solution.

4.1.1 ABEL INVERSION

The Abel transform is a special case of Radon transform when the distribution function $\varepsilon(x, y)$ is radially symmetric and depends only on $r = \sqrt{x^2 + y^2}$, so $\varepsilon(x, y) = \varepsilon(r)$. This means that the set of projections $I(p, \theta)$ are equivalent for any angle θ. Let us, for simplicity, set $\theta = 0$, as shown in Fig. 35. Then $I(p, \theta) = I(y)$. After these simplifications the Radon transform given in Eq. (90) becomes the Abel transform

$$I(y) = 2 \int_0^\infty \varepsilon(r)\, dx = 2 \int_y^\infty \frac{\varepsilon(r) r dr}{\sqrt{r^2 - y^2}}, \tag{96}$$

where $x = \sqrt{r^2 - y^2}$ and $xdx = rdr$.

Since all emitters are located inside the quartz tube, we can set the limits of integration at its walls. Abel transform is then,

$$I(y) = 2 \int_0^{x_{max}} \varepsilon(r)\, dx = 2 \int_y^R \frac{\varepsilon(r) r dr}{\sqrt{r^2 - y^2}}, \tag{97}$$

where $x_{max} = \sqrt{R^2 - y^2}$.

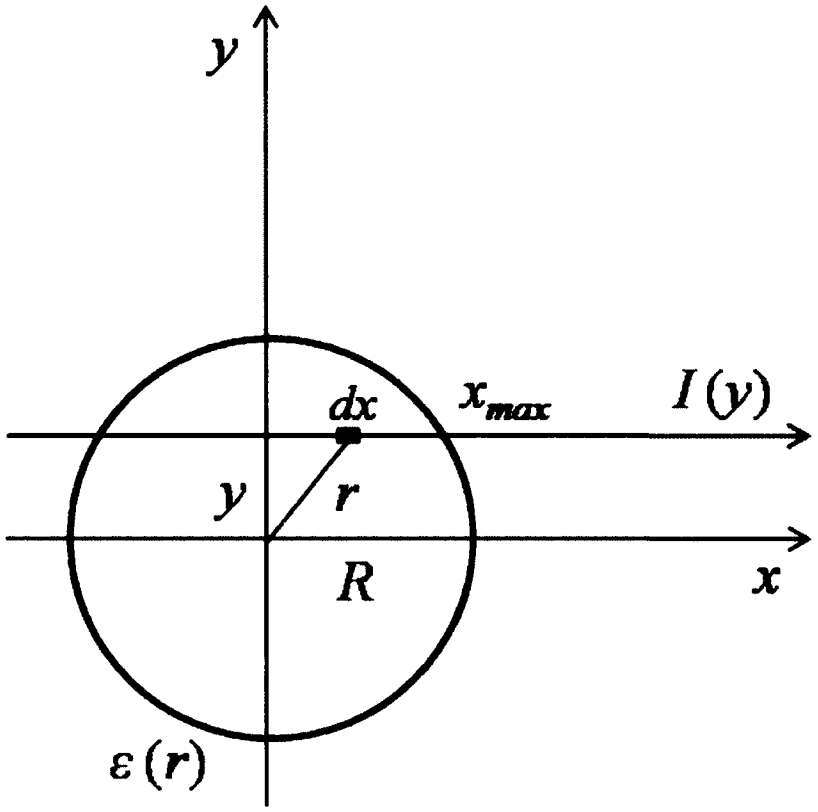

FIG. 35. Scheme of the cylindrical symmetry geometry for Abel transform.

The inverse integral of Abel transform is widely used formula in the literature [15]

$$I(y) = -\frac{1}{\pi}\int_{r}^{\infty}\frac{I'(y)dy}{\sqrt{y^2-r^2}}, \tag{98}$$

or, when the integration is limited to the walls of the quartz tube,

$$I(y) = -\frac{1}{\pi}\int_{r}^{R}\frac{I'(y)dy}{\sqrt{y^2-r^2}}, \tag{99}$$

where $I'(y)$ is the first derivative of $I(y)$ with respect to y.

We have tested both direct and inverse Abel transforms on two test functions the Gaussian and parabolic distribution as test functions presented in Eq. (91) and Eq. (92), respectively. First, we calculated direct Abel transform of given functions

using Eq. (97). Then, we used obtained data to calculate inverse Abel transform, Eq. (99), and return values of the original test functions.

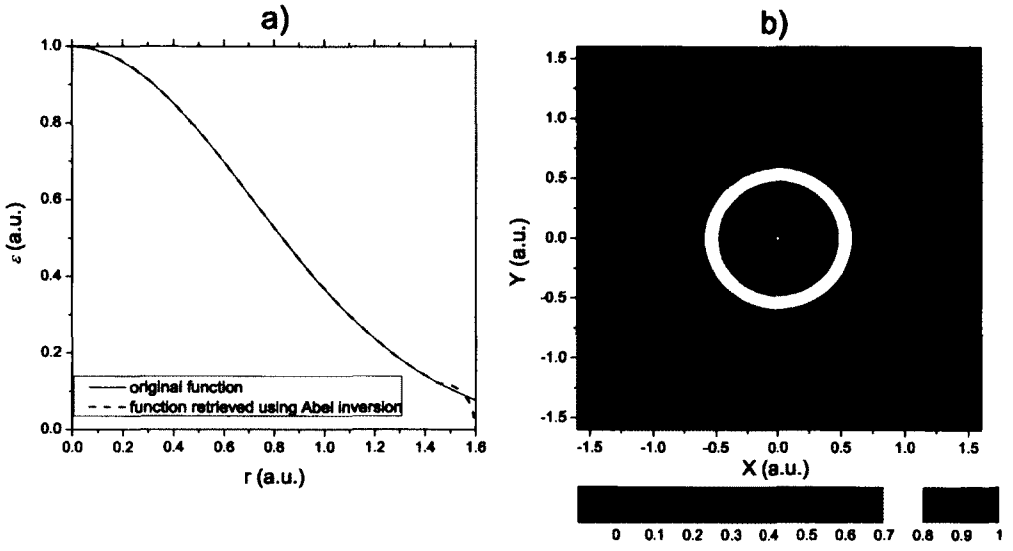

FIG. 36. The inverse Abel transform of Gaussian distribution function: a) comparison with analytical function for an arbitrary angle: full line represents the analytical function, dashed line represents numerically obtained function and b) expanded numerically obtained $\varepsilon(r)$ on the whole 0^0 to 360^0 range for better visualisation.

Figure 36(a) shows comparison between original Gaussian distribution function and the values of the same function obtained after performing direct and inverse Abel transforms. It can be seen that for the most part the results stand in good agreement. The only divergence occurs at the very end of integration range which suggests that these results should be taken with caution. Although there is no angular dependence, for better visualisation, we have expanded numerically obtained $\varepsilon(r)$ dependence on whole 0^0 to 360^0 range and presented results in Fig. 36(b). Similar results were obtained after performing Abel inversion on parabolic distribution function, shown in Fig. 37. In this case, we see even stronger discrepancy at the end of the integration range between original function and Abel inverted data.

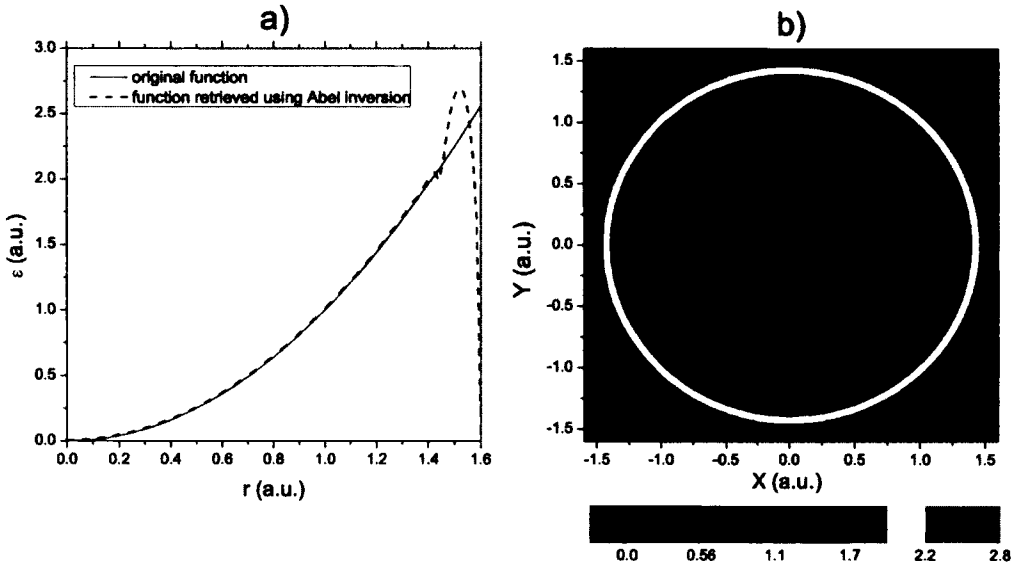

FIG. 37. The inverse Abel transform of parabolic distribution function: a) comparison with analytical function for an arbitrary angle: full line represents the analytical function, dashed line represents numerically obtained function and b) expanded numerically obtained $\varepsilon(r)$ on whole 0^0 to 360^0 range for better visualisation.

The above discussion applies only in the case of ideal, smooth function. In order to make a stronger test, we introduced a random percentage error due to experimental uncertainties into calculation and tried to repeat the inversion process. Then the outcome starts to mimic the real experimental conditions. To test this effect we have added 1%, 5%, and 10% error to data obtained after direct Abel transform and then carried out Abel inversion using new data with error.

It can be seen from Fig. 38 that we were able to reproduce the original data using Abel inversion with fair accuracy when the introduced error in the Gaussian function was less than 5%. When error exceeded 5%, the noise became so large that we were not able to reconstruct the original function. Similar results were obtained when the parabolic distribution function was tested, as shown in Fig. 39.

We expect the percentage error in our experiment within 5 and 10 %. For that

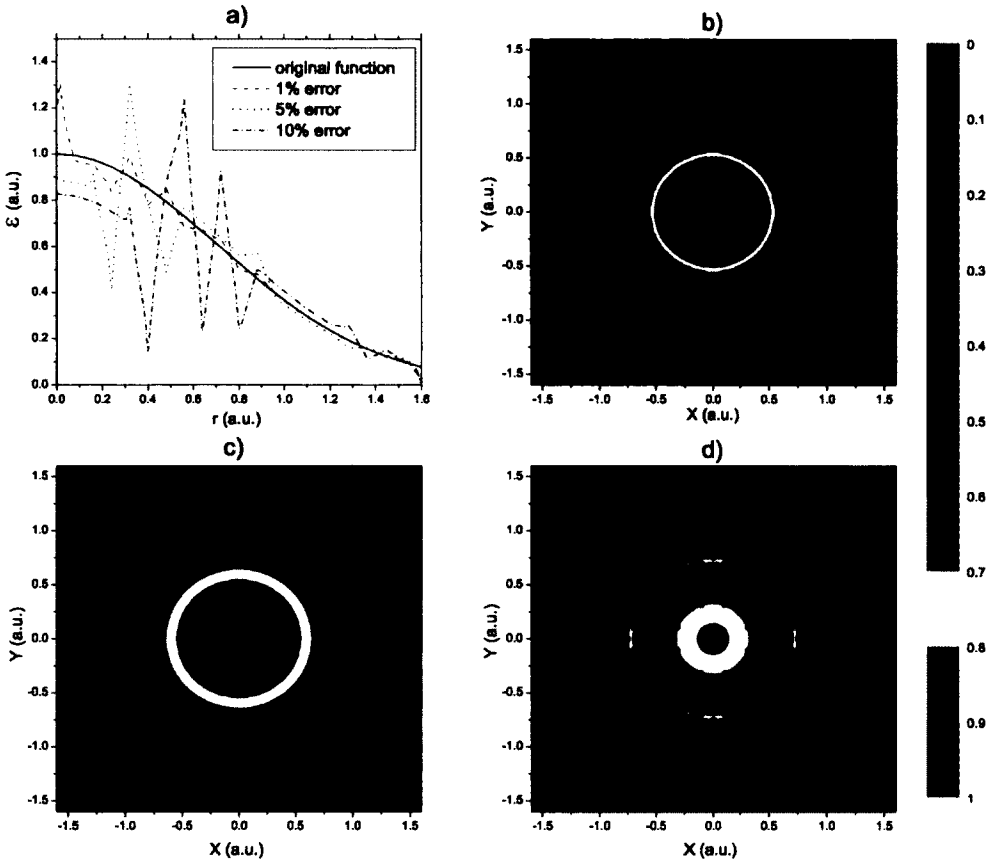

FIG. 38. The inverse Abel transform of Gaussian distribution function: a) comparison with analytical function for an arbitrary angle: full line is the analytical function, and dashed, dotted, dash-dotted lines are calculated Gaussian profiles with 1%, 5%, 10% errors, respectively, and b), c), and d) are expanded $\varepsilon(r)$ on whole 0^0 to 360^0 range for better visualisation with percentage error of 1%, 5%, 10% , respectively.

reason we have decided to apply both cubic spline and polynomial smoothing approximation to smooth the noise in measured signal. Smooth polynomial approximation proved to be more stable and allowed us to reconstruct original function from Abel inverted integral, even in the case when the percentage error was 10%.

Results obtained in this section have shown that Abel inversion represents a very useful tool for the case of radially symmetric discharges. In the real case, plasmas are

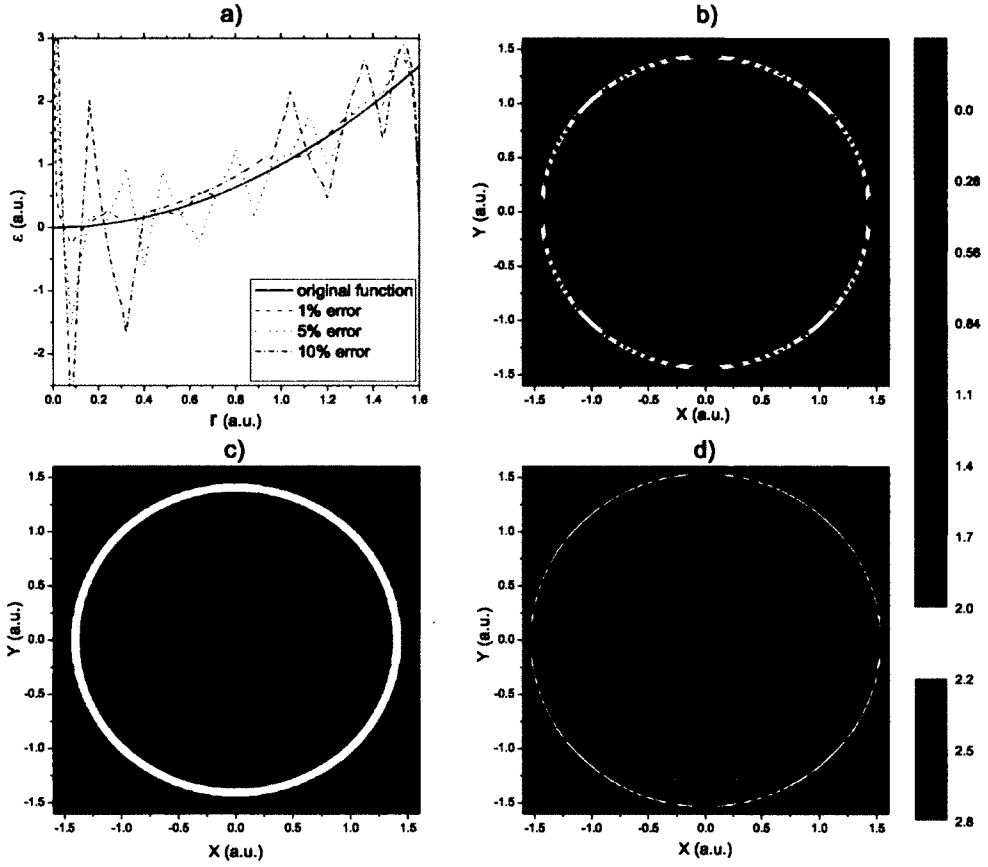

FIG. 39. The inverse Abel transform of parabolic distribution function: a) comparison with analytical function for an arbitrary angle: full line is the analytical function, and dashed, dotted, dash-dotted lines are calculated parabolic profiles with 1%, 5%, 10% errors, respectively, and b), c), and d) are expanded $\varepsilon(r)$ on whole 0^0 to 360^0 range for better visualisation with percentage error of 1%, 5%, 10% , respectively.

rarely radially symmetric. This is particularly the case with non-equilibrium, non-stationary, reactive plasmas explored in this work. These plasmas usually show more complicated, asymmetric properties, meaning that Abel inversion does not provide a complete insight in plasma internal structure.

4.1.2 ASYMMETRIC DISCHARGE - TWO PATH APPROACH

In the study of internal structure in asymmetric plasma, we have developed and applied a technique based on the measurement of spectral line intensities in two mutually perpendicular directions. Similarly, to the previous symmetric case, we choose $\theta = 0$ (parallel to x axis) and $\theta = 90^0$ (parallel to y axis) as directions in our measurement. Then $I(p, \theta = 0) = I(y)$ and $I(p, \theta = 90^0) = I(x)$ and $r = \sqrt{x^2 + y^2}$, as shown in Fig. 40. In addition we assume that the spatial distribution is given by

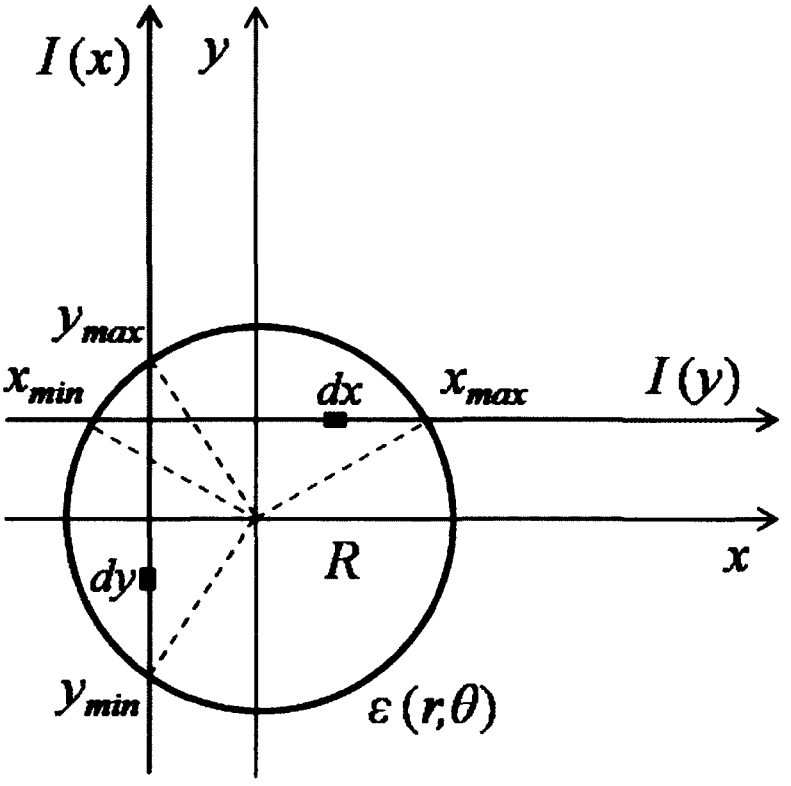

FIG. 40. Scheme of the cylindrical symmetry geometry for asymmetric discharge. $I(x)$ is the Radon integral at x; and $I(y)$ is the Radon integral at y

leading three terms in its Fourier expansion [16, 17]

$$\varepsilon(x, y) = \varepsilon(r, \theta) = H(r) + K(r)\cos\theta + L(r)\sin\theta, \qquad (100)$$

where $H(r)$, $K(r)$, and $L(r)$ are monotonous functions of radius.

Restricting the distribution to only three terms introduces greater probability for inhomogeneities and phantom images to appear, which presents difficulties for formulating the entire angular distribution of plasma parameters. Nevertheless, this approach still delivers additional information on the internal plasma structure. After applying above assumptions and combining Eq. (100) with Radon integral (90), we get

$$\begin{aligned} I(y) &= \int_{x_{min}}^{x_{max}} \varepsilon(r,\theta)\,dx = \int_{x_{min}}^{x_{max}} (H(r) + K(r)\cos\theta + L(r)\sin\theta)\,dx \\ I(x) &= \int_{y_{min}}^{y_{max}} \varepsilon(r,\theta)\,dy = \int_{y_{min}}^{y_{max}} (H(r) + K(r)\cos\theta + L(r)\sin\theta)\,dy, \end{aligned} \tag{101}$$

where $x_{max} = -x_{min} = \sqrt{R^2 - y^2}$, $y_{max} = -y_{min} = \sqrt{R^2 - x^2}$, $\cos\theta = x/r$, and $\sin\theta = y/r$.

Equation (101) can be transformed into

$$\begin{aligned} I(y) &= 2\int_0^{x_{max}} H(r)\,dx + 2\int_0^{x_{max}} L(r)\frac{y}{r}\,dx \\ I(x) &= 2\int_0^{y_{max}} H(r)\,dy + 2\int_0^{y_{max}} K(r)\frac{x}{r}\,dy, \end{aligned} \tag{102}$$

where we have applied the symmetry properties of the sine and cosine functions on symmetric interval within angle θ interval $(-\frac{\pi}{2}, \frac{\pi}{2})$.

Antisymmetric parts of the observed distributions are

$$\begin{aligned} I(-y) &= 2\int_0^{x_{max}} H(r)\,dx + 2\int_0^{x_{max}} L(r)\frac{(-y)}{r}\,dx \\ I(-x) &= 2\int_0^{y_{max}} H(r)\,dy + 2\int_0^{y_{max}} K(r)\frac{(-x)}{r}\,dy. \end{aligned} \tag{103}$$

It follows that we can express $H(r)$, $K(r)$, and $L(r)$ in terms of symmetric and antisymmetric parts of measured functions,

$$\begin{aligned} \tfrac{1}{2}(I(x) + I(-x)) &= 2\int_0^{y_{max}} H(r)\,dy \\ \tfrac{1}{2}(I(x) - I(-x)) &= 2\int_0^{y_{max}} K(r)\frac{x}{r}\,dy \\ \tfrac{1}{2}(I(y) + I(-y)) &= 2\int_0^{x_{max}} H(r)\,dx \\ \tfrac{1}{2}(I(y) - I(-y)) &= 2\int_0^{x_{max}} L(r)\frac{y}{r}\,dx. \end{aligned} \tag{104}$$

Substituting $y = \sqrt{r^2 - x^2}$ and $x = \sqrt{r^2 - y^2}$, the Eq. (104) becomes

$$\begin{aligned}
\tfrac{1}{2}(I(x) + I(-x)) &= 2\int_x^R \frac{H(r)rdr}{\sqrt{r^2 - x^2}} \\
\tfrac{1}{2x}(I(x) - I(-x)) &= 2\int_x^R \frac{K(r)}{r}\frac{rdr}{\sqrt{r^2 - x^2}} \\
\tfrac{1}{2}(I(y) + I(-y)) &= 2\int_y^R \frac{H(r)rdr}{\sqrt{r^2 - y^2}} \\
\tfrac{1}{2y}(I(y) - I(-y)) &= 2\int_y^R \frac{L(r)}{r}\frac{rdr}{\sqrt{r^2 - y^2}}.
\end{aligned} \tag{105}$$

It can be seen that the above equations are similar to Eq. (97) for cylindrical symmetry. This means that we can evaluate $H(r)$, $K(r)$, and $L(r)$ by applying the Abel inverted integral, Eq. (99)

$$\begin{aligned}
H(r) &= -\frac{1}{\pi}\int_r^R \Big(\frac{I(x) + I(-x)}{2}\Big)' \frac{dx}{\sqrt{x^2 - r^2}} \\
\frac{K(r)}{r} &= -\frac{1}{\pi}\int_r^R \Big(\frac{I(x) - I(-x)}{2x}\Big)' \frac{dx}{\sqrt{x^2 - r^2}}
\end{aligned} \tag{106}$$

and

$$\begin{aligned}
H(r) &= -\frac{1}{\pi}\int_r^R \Big(\frac{I(y) + I(-y)}{2}\Big)' \frac{dy}{\sqrt{y^2 - r^2}} \\
\frac{L(r)}{r} &= -\frac{1}{\pi}\int_r^R \Big(\frac{I(y) - I(-y)}{2y}\Big)' \frac{dy}{\sqrt{y^2 - r^2}}.
\end{aligned} \tag{107}$$

Function $H(r)$ can be evaluated either from horizontal or vertical measurements and this can serve as a good test of the applied technique. Since Gaussian (91) and parabolic (92) distribution functions are both radially symmetric we have chosen an asymmetric, $\varepsilon(x, y) = x + y$, function to test the two path method. We have simulated experimental measurements of spectral line intensities with direct Radon integral, which was proved to have sufficient accuracy. Then, we have employed the measurements at 0^0 and 90^0 to reconstruct $\varepsilon(x, y) = x + y$.

Comparison between the original function and the function reconstructed from the two path method is shown in Fig. 41. Again, as in the case of Abel inverted integral, the largest variation between original and reconstructed data is at the outer

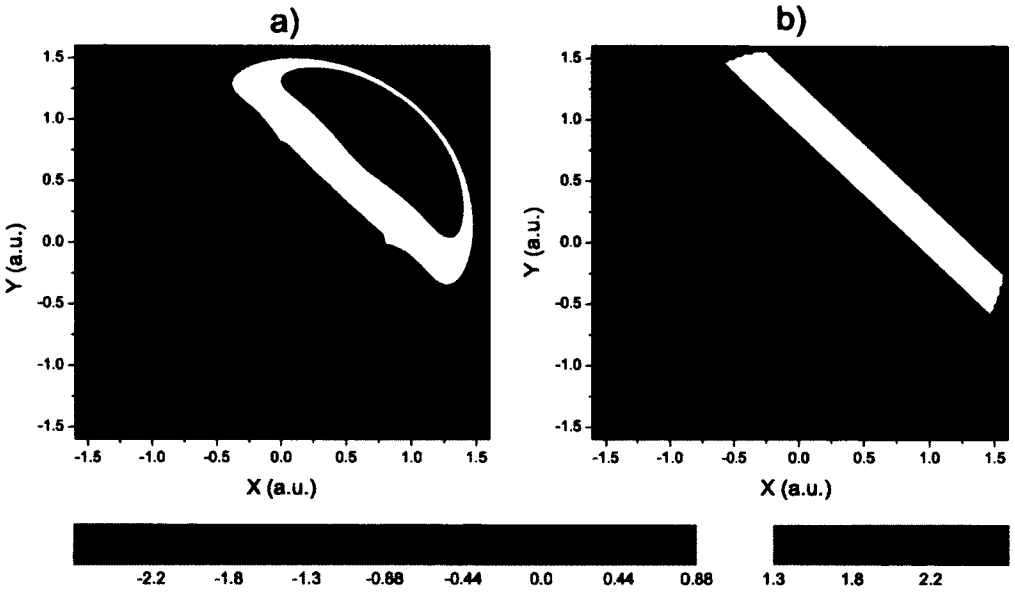

FIG. 41. Emissivity reconstruction for asymmetric discharge, represented by $\varepsilon(x,y) = x + y$: a) numerical solution using Newton-Cotes quadrature integration and b) analytical solution.

integration limits. It is evident from the Fig. 41 that applying this method will not reconstruct the initial function entirely but it will give us a qualitative insight into the sphere. We have determined that two-path method could reproduce a model for emissivity $\varepsilon(x,y)$ from an asymmetric discharge. Therefore, we should expect that it may confirm if the plasmoid, shown in Fig. 17, was sustained with surface wave or not.

4.1.3 TWO DIMENSIONAL INVERSE RADON INTEGRAL

In order to fully recover the desired information about the internal structure of the observed object, we need to go back to the Radon integral Eq. (90) and invert it, to solve for $\varepsilon(x,y)$ in terms of its projections $I(p,\theta)$

$$\varepsilon(x,y) = \Re^{-1}[I(p,\theta) + \eta)], \tag{108}$$

where η is the noise that may be introduced by the measurements and is assumed

with constant value.

We start by expressing the Fourier transform of the distribution function $\varepsilon(x,y)$ in the new coordinate system, given in Eq. (89)

$$\varepsilon(x,y) = \varepsilon(s,p) = \iint_{-\infty}^{\infty} E(\nu_s,\nu_p)\exp(i2\pi(s\nu_s + p\nu_p))\,d\nu_s d\nu_p, \tag{109}$$

where $E(\nu_s,\nu_p)$ is the Fourier transform of $\varepsilon(x,y)$ in frequency domain given as $E(\nu_s,\nu_p) = F[\varepsilon(x,y)]$, and ν_s and ν_p are corresponding coordinates in Fourier frequency domain.

The expression for the spectral line intensities, shown in Eq. (90), can be rewritten as

$$\begin{aligned} I(p,\theta) &= \int_{-\infty}^{\infty} \varepsilon(s,p)ds = \iint_{-\infty}^{\infty} E(\nu_s,\nu_p)\,d\nu_s d\nu_p \int_{-\infty}^{\infty} \exp(i2\pi(s\nu_s + p\nu_p))\,ds \\ &= \iint_{-\infty}^{\infty} \exp(i2\pi p\nu_p)E(\nu_s,\nu_p)\,d\nu_s d\nu_p \int_{-\infty}^{\infty} \exp(i2\pi s\nu_s)\,ds. \end{aligned} \tag{110}$$

After applying property of delta function that $\int_{-\infty}^{\infty} f(x)\delta(x)dx = f(0)$ we get

$$I(p,\theta) = \int_{-\infty}^{\infty} \exp(i2\pi p\nu_p)E(0,\nu_p)\,d\nu_p\,. \tag{111}$$

Here we use the Fourier slice theorem [43], which relates the one dimensional Fourier transform of a projection at an angle θ, $F[I_\theta(p)]$ to the central slice at an angle θ, of its two dimensional Fourier transform $E(0,\nu_p)$, such that

$$F[I_\theta(p)] = E(0,\nu_p). \tag{112}$$

The spectral line intensities $I(p,\theta)$ may now be expressed as

$$I(p,\theta) = \int_{-\infty}^{\infty} \exp(i2\pi p\nu_p)F[I_\theta(p)]\,d\nu_p. \tag{113}$$

When we express the Eq. (109) in polar coordinates in frequency domain we get

$$\varepsilon(x,y) = \varepsilon(s,p) = \int_0^{2\pi} d\theta \int_0^{\infty} \exp[i2\pi\nu(rsin(\varphi-\theta))]E(\nu,\theta)\,\nu\,d\nu, \tag{114}$$

where

- (ν, θ) are the polar coordinates of (ν_s, ν_p) in frequency domain such that

$$d\nu_s\, d\nu_p = \nu\, d\nu\, d\theta \text{ and}$$
$$\nu_s = \nu \cos\theta$$
$$\nu_p = \nu \sin\theta$$

- (r, φ) are the polar coordinates of the pair (p, s) such that

$$p = r\cos\varphi$$
$$s = r\sin\varphi$$

hence $s\nu_s + p\nu_p = \nu r \sin(\varphi - \theta) = p_0$.

The unknown distribution $\varepsilon(x, y)$ is then

$$\varepsilon(x,y) = \int_0^{\pi} d\theta \int_0^{\infty} \exp(i2\pi\nu p_0) E(\nu,\theta)\, \nu\, d\nu + \int_0^{\pi} d\theta \int_0^{\infty} \exp(i2\pi\nu p_0) E(\nu,\theta+\pi)\, \nu\, d\nu, \tag{115}$$

and using the property $E(\nu, \theta + \pi) = E(-\nu, \theta)$ [15], the above expression becomes

$$\begin{aligned} \varepsilon(x,y) &= \int_0^{\pi} d\theta \int_{-\infty}^{\infty} \exp(i2\pi\nu p_0) E(\nu,\theta)\, |\nu|\, d\nu \\ &= \int_0^{\pi} d\theta \int_{-\infty}^{\infty} \exp(i2\pi\nu p_0) F[I_\theta(p)]\, |\nu|\, d\nu. \end{aligned} \tag{116}$$

The inverse Fourier transform of the Eq. (116) gives

$$\varepsilon(x,y) = \int_0^{\pi} d\theta \int_{-\infty}^{\infty} I(p,\theta) F^{-1}[|\nu|] dp, \tag{117}$$

where the inverse Fourier transform of function $|\nu|$ [44] is

$$F^{-1}[|\nu|] = -\frac{1}{2\pi^2 p^2}. \tag{118}$$

Finally, the inverse Radon formula is expressed as

$$\varepsilon(x,y) = -\frac{1}{2\pi^2} \int_0^{\pi} d\theta \int_{-\infty}^{\infty} \frac{I(p,\theta)}{(p-p_0)^2} dp. \tag{119}$$

Integration by parts of the Eq. (119) gives an equivalent formula for Radon inverse formula,

$$\varepsilon(x,y) = -\frac{1}{2\pi^2} \int_0^{\pi} d\theta \int_{-\infty}^{\infty} \frac{\frac{\partial I(p,\theta)}{\partial p}}{(p-p_0)} dp. \tag{120}$$

Finding numerical solutions of the Eq. (119) opens the new set of challenges in our study. The basic inversion formulas are rigorously valid if the function $\varepsilon(x, y)$ is continuous with compact support (meaning that the function is different from zero on the defined region) and the projections $I(p, \theta)$ are given for all the angles. This means that we need an infinite set of projections while in reality it is possible to obtain only a discrete set. The theorem by Solomon *et. al* [45] states that a function of compact support in R^2 is uniquely determined by any infinite set, but not by any finite set, of its projections. This implies that we need to sacrifice uniqueness for practical applications. Another important issue to consider is that stability of the solution is greatly influenced by noise that may be introduced during experimental measurements. Thus, we may need extremely precise measurements to achieve satisfactory accuracy and that may be physically impossible. These problems have been extensively studied in recent years resulting in numerous algorithms and numerical approaches. In the following sections we will present a comparison between two different approaches that were successfully applied in plasma tomography.

Direct integration

One straightforward approach in solving Radon inversion Eq. (119) is to simply apply one of already developed mathematical codes for numerical integration. However, the integral in Eq. (119) approaches infinity when p approaches p_0. One possible solution for this singularity problem is to apply the Cauchy principal value method [46] defined as follows

$$\int_{-\infty}^{\infty} \frac{\varphi(x)}{x^{2m}} = \int_{0}^{\infty} dx\, x^{-2m}\{\varphi(x) + \varphi(-x) - 2\sum_{k=1}^{m} \frac{x^{2k-2}}{(2k-2)!}\varphi^{(2k-2)}(0)\}, \tag{121}$$

$$\int_{-\infty}^{\infty} \frac{\varphi(x)}{x^{2m+1}} = \int_{0}^{\infty} dx\, x^{-2m-1}\{\varphi(x) - \varphi(-x) - 2\sum_{k=1}^{m} \frac{x^{2k-1}}{(2k-1)!}\varphi^{2k-1}(0)\}.$$

In our case $\varphi(x)$ corresponds to $I(p, \theta)$, $x = p - p_0$, $m = 1$, and Eq. (119) becomes

$$\varepsilon(x, y) = -\frac{1}{2\pi^2}\int_{0}^{\pi} d\theta \int_{-\infty}^{\infty} \frac{I(p, \theta)}{(p - p_0)^2} dp = \tag{122}$$

$$= -\frac{1}{2\pi^2}\int_{0}^{\pi} d\theta \int_{0}^{\infty} \frac{I(x + p_0, \theta) + I(-x + p_0, \theta) - 2I(p_0, \theta)}{x^2} dx.$$

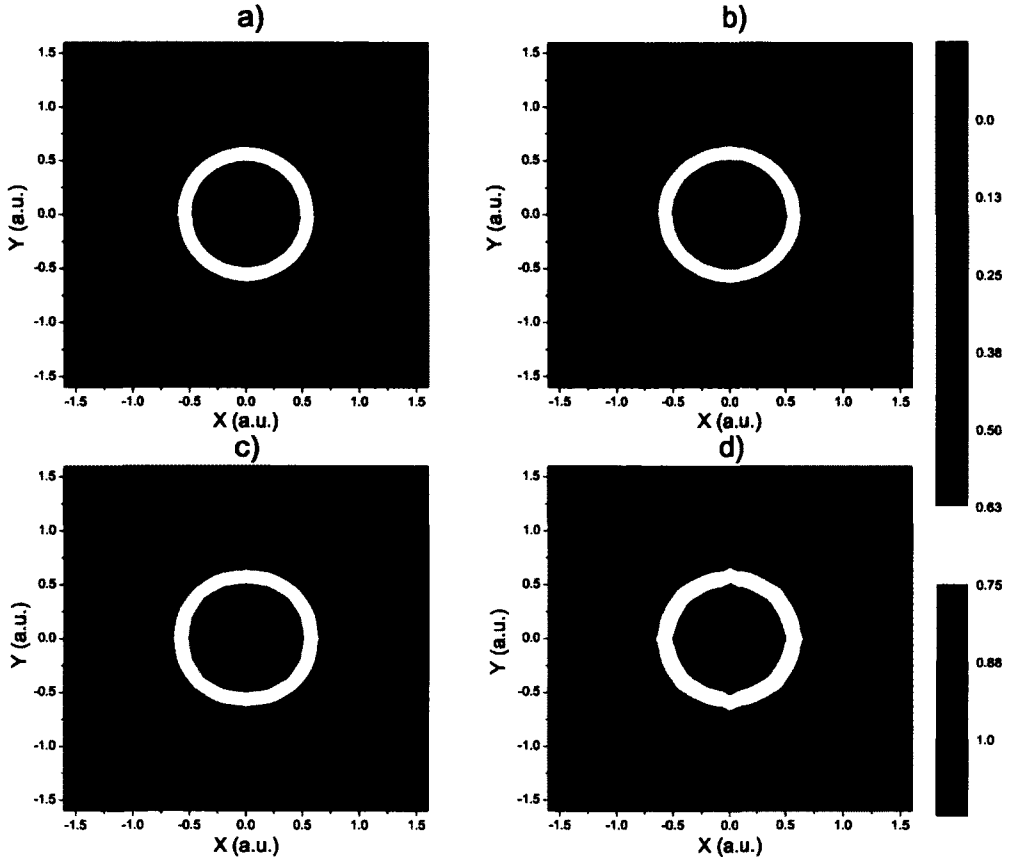

FIG. 42. The Inverse Radon transform of Gaussian distribution function obtained using the direct integration method on the $0^0 - 180^0$ range of angles at a) 17 projections on 45 angles, b) 17 projections on 21 angles, c) 17 projections on 5 angles, and d) 5 projections on 21 angles.

Equation (120) is then

$$\varepsilon(x,y) = -\frac{1}{2\pi^2}\int_0^{\pi} d\theta \int_{-\infty}^{\infty} \frac{I'(p,\theta)}{(p-p_0)} dp = \tag{123}$$

$$= -\frac{1}{2\pi^2}\int_0^{\pi} d\theta \int_0^{\infty} \frac{I'(x+p_0,\theta) - I'(-x+p_0,\theta)}{x} dx,$$

where $I'(x,\theta) = \dfrac{\partial I(x,\theta)}{\partial x}$.

To test this method we applied two distribution functions: Gaussian distribution function, given in Fig. 31 and parabolic distribution function given in Fig 32. The test functions were reconstructed in the following way. First, we generated a discrete set of projections, as was shown in Figs. 36 and 37, respectively. Then, we used a direct integration of Radon inverse integral to obtain the original distributions.

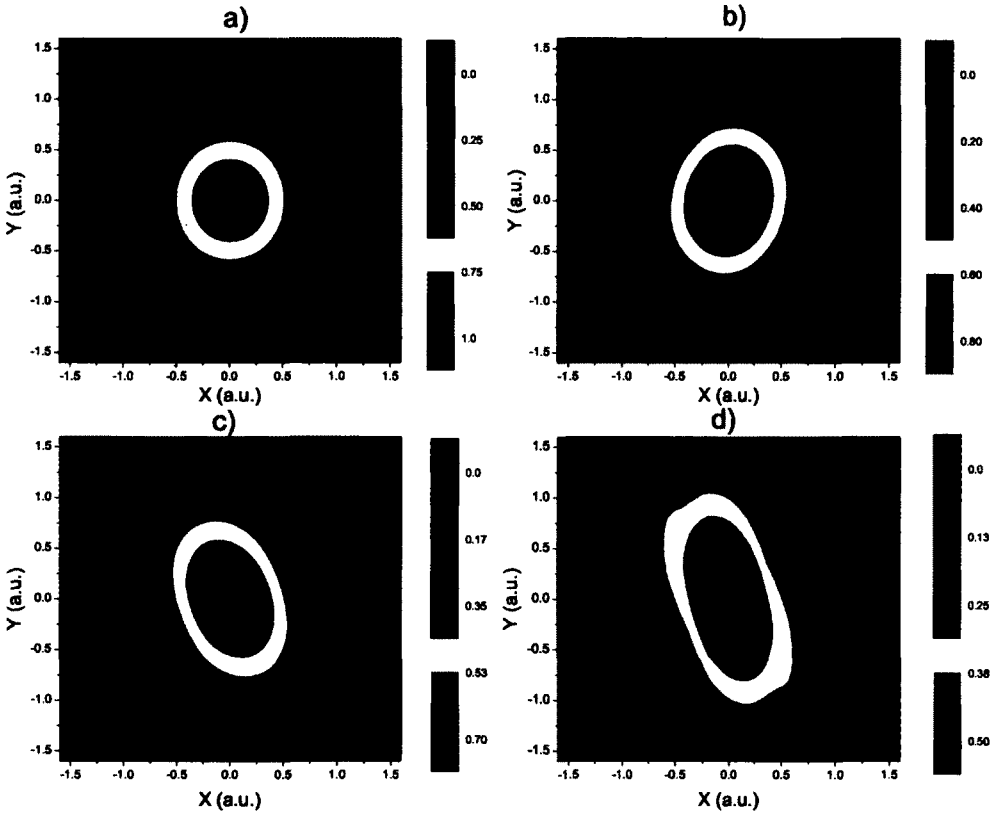

FIG. 43. The Inverse Radon transform of Gaussian distribution function obtained using the direct integration method at 21 different angles and 17 projections at each angle on the a) $10^0 - 170^0$ interval, b) $10^0 - 150^0$ interval, c) $48^0 - 168^0$ interval, and d) $60^0 - 150^0$ interval.

Figure 42 shows how the inverse Radon transform of Gaussian distribution function depends on number of measured angles and number of projections for each angle

on the $0^0 - 180^0$ interval. As seen in the Fig. 42, it is obvious that the number of projections does not change results significantly and that even with only five projections we were able to reconstruct the starting function quantitatively. On the other

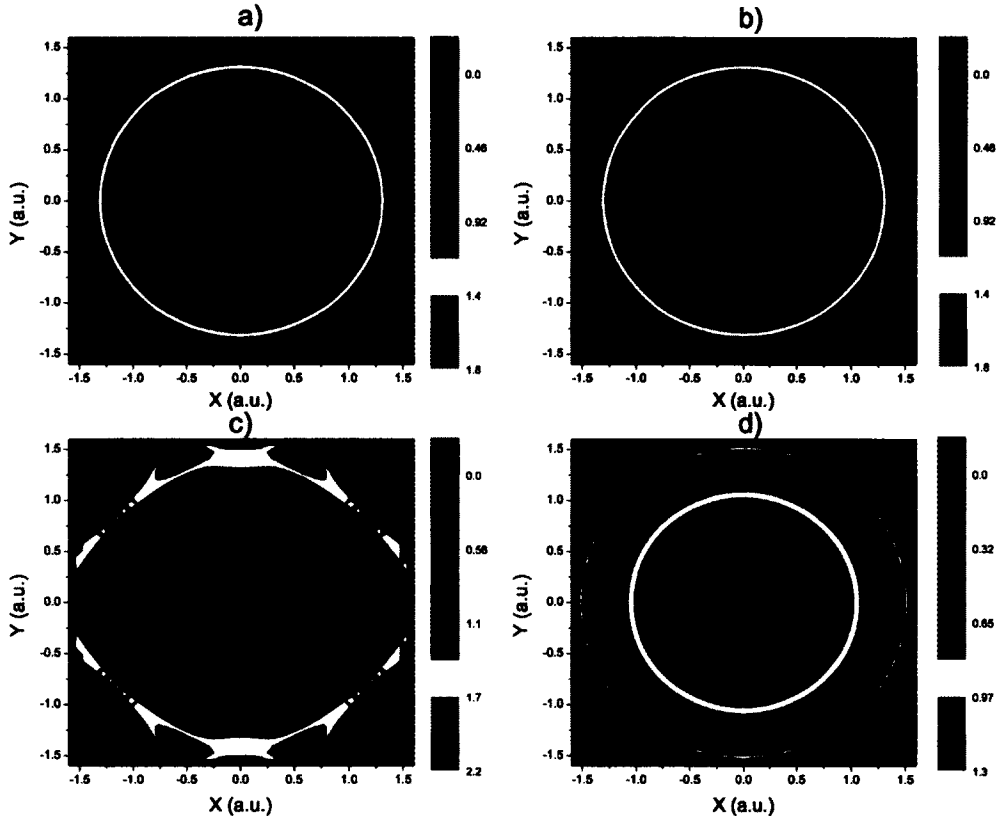

FIG. 44. The Inverse Radon transform of the parabolic distribution function obtained using the direct integration method on the $0^0 - 180^0$ range of angles at a) 17 projections on 45 angles, b) 17 projections on 21 angles, c) 17 projections on 5 angles, and d) 5 projections on 21 angles.

hand, the quality of the Radon inverse integral of the test function depends highly on the number of angles. It means that in order to apply Radon inverted integral with satisfying accuracy, measurements on at least 15 different angles were needed. This requirement was fulfilled in our experiment where we have obtained measurements

at 17 projections at 21 angles. However, it seems that some information is always lost in the reconstruction process which is shown as non physical, negative area at the rims of the circle, for example.

We have also addressed the problem of the limited range of measured angles. In our experiment it was not possible to approach plasma from every angle. We were able to collect data only on the $48^0 - 168^0$ interval. In Fig. 43 we have shown that the areas with missing data were reconstructed as dark spots, perturbing the cylindrical symmetry in that way. In addition, even though the shape of the Gaussian function

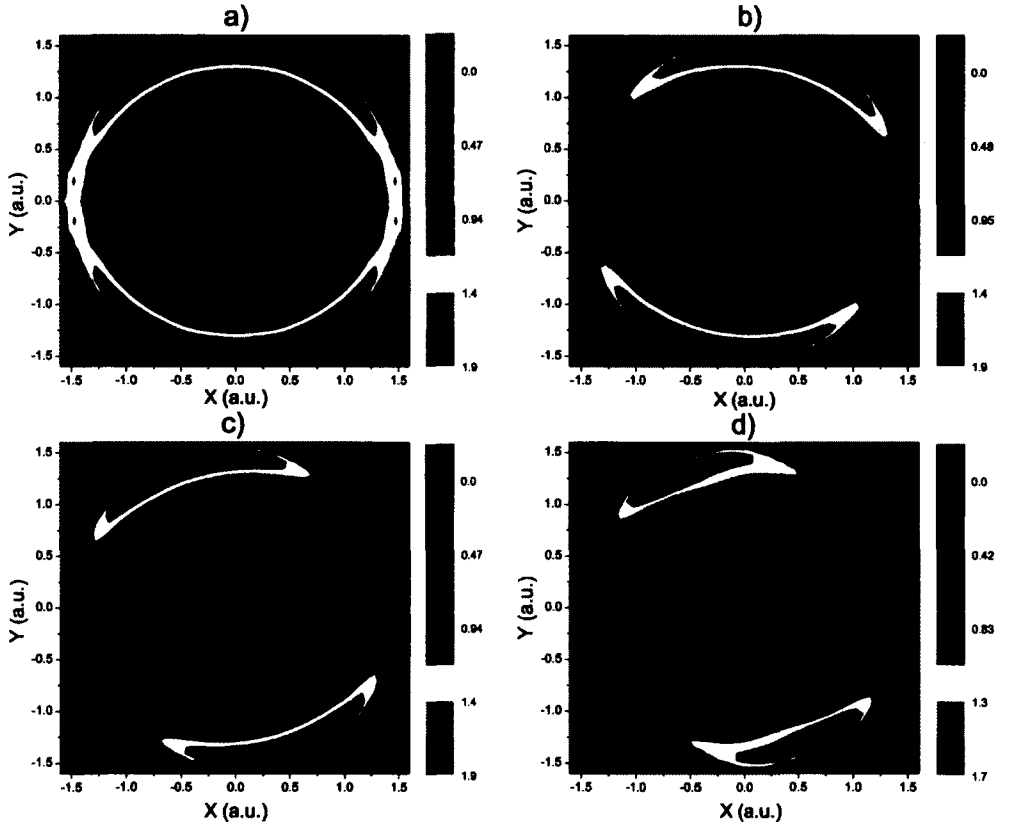

FIG. 45. The Inverse Radon transform of the parabolic distribution function obtained using the direct integration method at 21 different angles and 17 projections at each angle on the a) $10^0 - 170^0$ interval, b) $10^0 - 150^0$ interval, c) $48^0 - 168^0$ interval, and d) $60^0 - 150^0$ interval.

is conserved, the quantitative values of the function at each point were not. There is a 30% of intensity loss on the $48^0 - 168^0$ angle range, which should not be neglected when reconstructing experimental data.

We repeated the same procedure on the parabolic distribution function and obtained similar results, which are shown in Figs. 44 and 45. Figures 44 and 45 show that the parabolic distribution function shows even stronger dependence on the number of measured angles and the range of angles. To conclude, the Radon direct integration is straightforward, easy to implement method, but it needs to be used with caution due to its high sensitivity to the noise introduced by measurements.

Filtered back projection

Filtered back projection (FBP) is a more accurate, easy to implement numerical technique that is widely used for solving reconstruction problems. Here we present the FBP approach for parallel projection data with the τ sampling interval.

We start with the equation for the inverse Radon transform, Eq. (116)

$$\varepsilon(x,y) = \int_0^{\pi} d\theta \int_{-\infty}^{\infty} d\nu |\nu| F[I(p,\theta)] exp(i2\pi\nu p_0), \tag{124}$$

which can be rewritten as

$$\varepsilon(x,y) = \int_0^{\pi} Q_\theta(p) d\theta, \tag{125}$$

where $Q_\theta(p)$ expressed in frequency domain is

$$Q_\theta(p) = \int_{-\infty}^{\infty} d\nu |\nu| F[I(p,\theta)] exp(i2\pi\nu p_0). \tag{126}$$

In principle, the integration in filtered projection given by Eq. (125) has to be carried over all frequencies. However, in practice the energy contained in the Fourier transform components above a certain frequency is negligible and we may consider the projections bandlimited. When the highest frequency in the projections is finite, Eq. (126) becomes

$$Q_\theta(p) = \int_{-\infty}^{\infty} F[I_\theta(p)] H(\nu) exp(i2\pi\nu p_0) d\nu, \tag{127}$$

where $H(\nu)$ is a high frequency noise filter.

The most common filters used in literature are the Ram-Lak filter [47]

$$H(\nu) = \begin{cases} |\nu|, & |\nu| \leq W \\ 0, & \text{otherwise,} \end{cases} \tag{128}$$

and the Shepp-Logan filter [48], shown in Fig. 46a

$$H(\nu) = \begin{cases} |\nu| \frac{\sin(\nu)}{\nu}, & |\nu| \leq W \\ 0, & \text{otherwise,} \end{cases} \tag{129}$$

where W represents any frequency greater than the smallest beyond which the spectral energy in all the projections may be neglected.

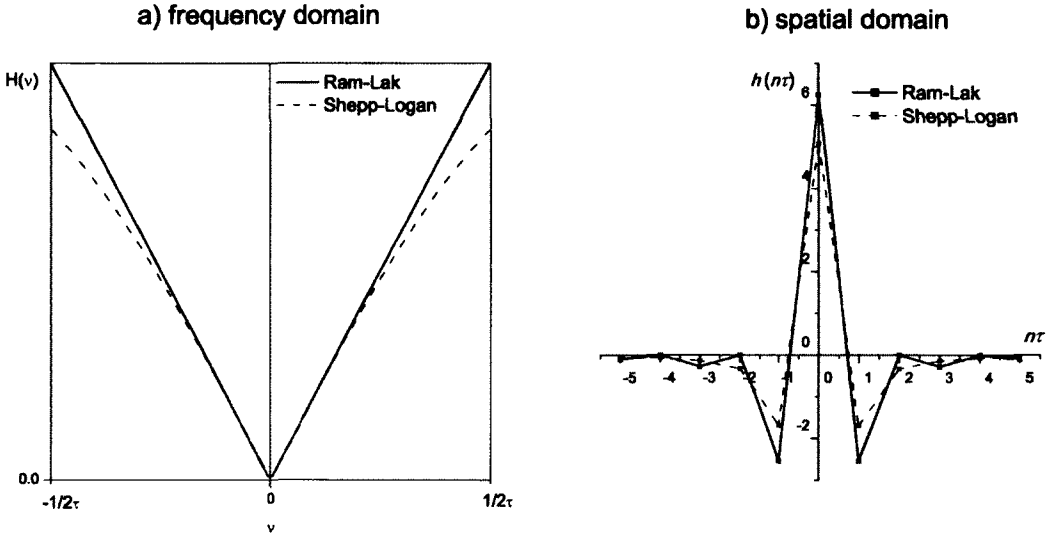

FIG. 46. Ram-Lak and Shepp-Logan filters in a) frequency and b) spatial domain.

$H(\nu)$ functions, actually, represent the Fourier transform of a projection processing filter, and the impulse response $h(p)$ of this filter is then given with the inverse Fourier transform of $H(\nu)$ [47]

$$h(p) = \int_{-\infty}^{\infty} H(\nu) \exp(i2\pi \nu p) d\nu. \tag{130}$$

Experimentally obtained line intensities are presented as a discrete set of projections, measured with the spatial sampling interval τ. Thus, $p = n\tau$ where n is an integer. Hence, in the spatial domain we have

$$h(n\tau) = \begin{cases} \frac{1}{4\tau^2}, & \text{n} = 0 \\ 0, & \text{n even} \\ -\frac{1}{n^2\pi^2\nu^2}, & \text{n odd}, \end{cases} \tag{131}$$

for Ram-Lak filter and

$$h(n\tau) = \begin{cases} \frac{2}{\pi^2\tau^2}, & \text{n} = 0 \\ -\frac{2}{n^2\pi^2(4\nu^2-1)}, & \text{n} \neq 0, \end{cases} \tag{132}$$

for Shepp-Logan filter, see Fig. 46b.

By applying the inverse Fourier transformation and the convolution theorem for each projection $I_\theta(p)$ we obtain

$$Q_\theta(p) = \int_{-\infty}^{\infty} I_\theta(p')h(p-p')\,dp'. \tag{133}$$

If we assume that each projection $I_\theta(k\tau)$ is zero outside the index range $k = 0, 1, ..., K-1$, where K is the number of angles at which the projections are sampled, we may express the filtered projection as

$$Q_\theta(n\tau) = \tau \sum_{k=0}^{K-1} h(n\tau - k\tau) I_\theta(k\tau) \tag{134}$$
$$n = 0, 1, ..., K-1.$$

Finally, the reconstructed function $\epsilon(x, y)$ may be obtained by the discrete approximation of Eq. (125),

$$\varepsilon(x,y) = \frac{\pi}{K} \sum_{i=1}^{K} Q_{\theta_i}(-x \sin\theta_i + y \cos\theta_i). \tag{135}$$

This means that each filtered projection has to be back-projected. For every pair (x, y), there is a point $p = -x \sin\theta_i + y \cos\theta_i$ for a given angle θ. The contribution of each filtered projection Q_{θ_i} to the reconstruction of $\varepsilon(x, y)$ at the particular point (x, y) depends on the value of p for a given θ_i. Depending on a resolution of our reconstruction image it may happen that value of $p = -x \sin\theta_i + y \cos\theta_i$ does not

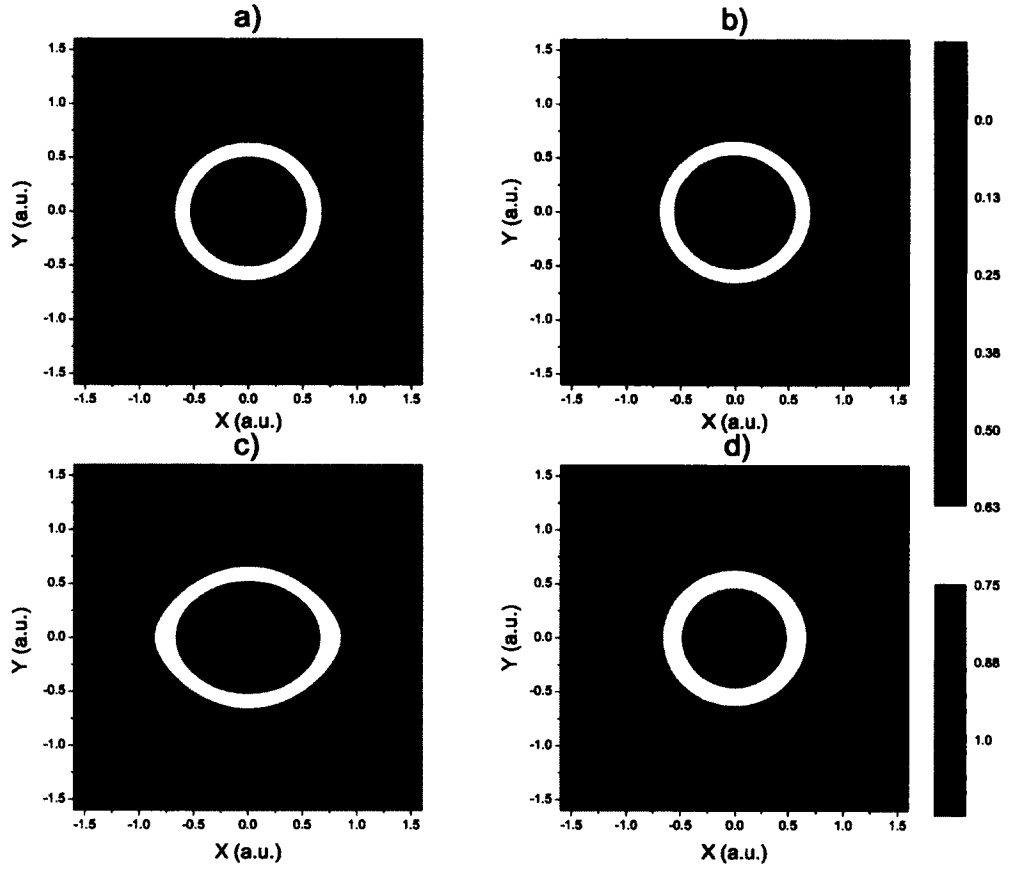

FIG. 47. The inverse Radon transform of Gaussian distribution function obtained using the filtered back projection method with the Shepp-Logan filter on the $0^0 - 180^0$ range of angles at a) 17 projections on 45 angles, b) 17 projections on 21 angles, c) 17 projections on 5 angles, and d) 5 projections on 21 angles.

correspond to the values at which $Q_\theta(p)$ was sampled. The suitable interpolation of Q_θ values at such p successfully deals with that problem.

The filtered back projection method was tested on two functions, Gaussian and parabolic distribution function. It turned out that data obtained using Ram-Lak filter did not show any significant difference compared to data from Shepp-Logan filter. However, numerical code for Shepp-Logan filter proved to be more stable and for that reason, we presented our results by employing Shepp-Logan filtering. Figure

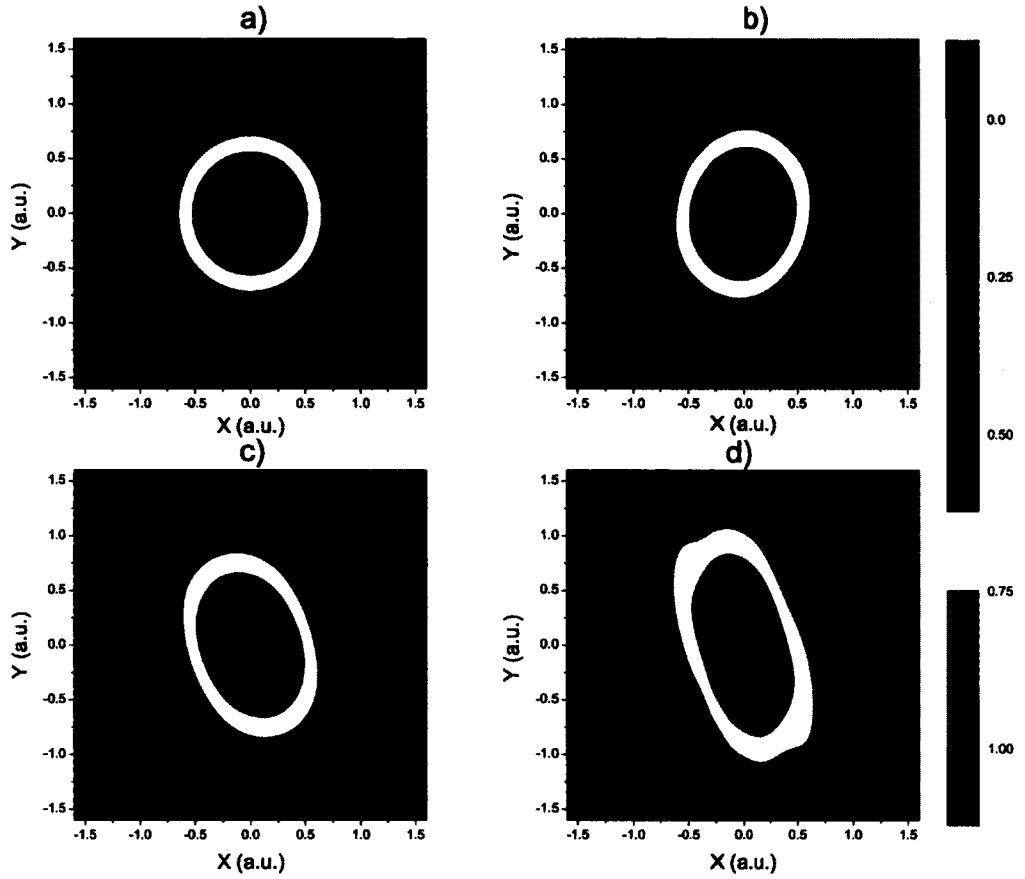

FIG. 48. The inverse Radon transform of Gaussian distribution function obtained using the filtered back projection method with the Shepp-Logan filter at 21 different angles and 17 projections at each angle on the a) $10^0 - 170^0$ interval, b) $10^0 - 150^0$ interval, c) $48^0 - 168^0$ interval, and d) $60^0 - 150^0$ interval.

47 shows the inverse Radon transform of Gaussian distribution function using the Shepp-Logan filter on number of measured angles and number of projections for each angle on the $0^0 - 180^0$ interval. It could be seen that FBP method is sensitive to number of angles while number of projections does not change results significantly. It is, also, obvious, from the Fig. 47b that measurements at 17 projections at 21 angles obtained in our experiment would allow reconstruction of the original function (population densities in our case) with satisfying accuracy. We conclude FBP provides

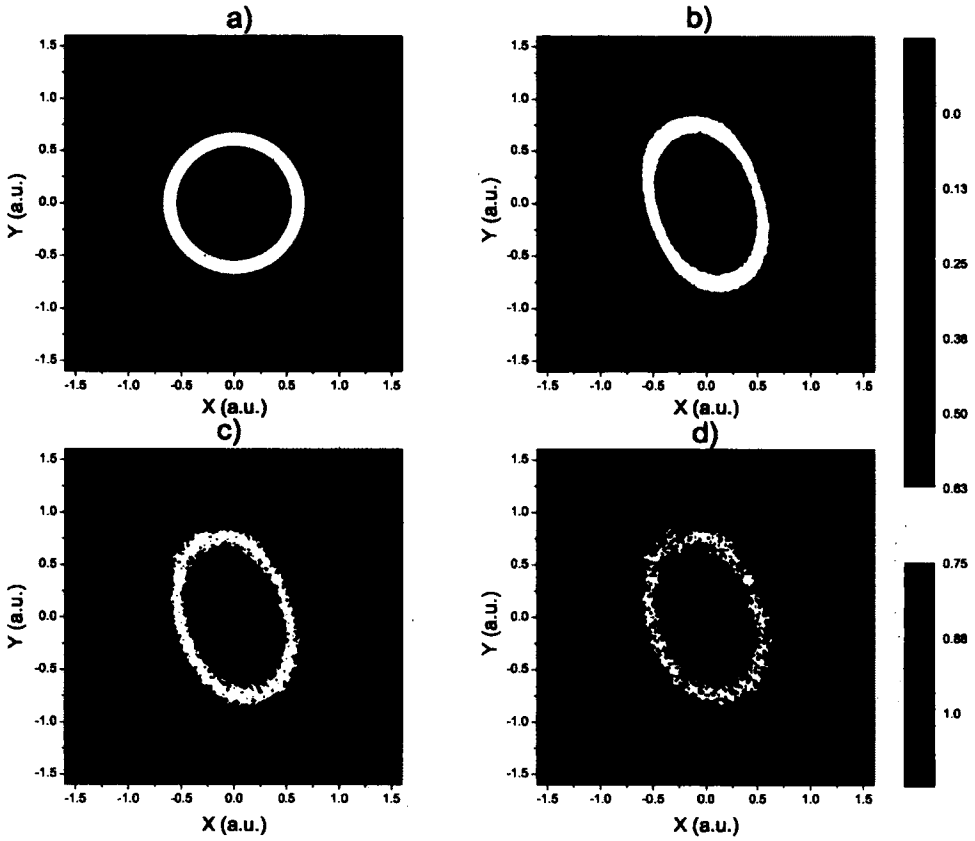

FIG. 49. Comparison between a) the original Gaussian distribution function and the inverse Radon transform of the Gaussian distribution function obtained using the filtered back projection method with the Shepp-Logan filter at 21 different angles and 17 projections at each angle on the $48^0 - 168^0$ interval with the b) 1% error, c) 5% error, and d) 10% error.

quantitative analysis of the reconstructed functions with satisfactory accuracy, that unlike direct integration of inverse Radon transform where the test functions were reconstructed only qualitatively (negative values at the rims of the circle).

The problem of the limited range of measured angles was also addressed. We observed similar behaviour as in case of direct integration; the areas with missing data were reconstructed as dark spots, perturbing the cylindrical symmetry in that way, as shown in Fig. 48. However, Fig. 48 shows that by employing FBP not only

the shape of the Gaussian function is conserved, but also the quantitative values of the function are reproduced at each location.

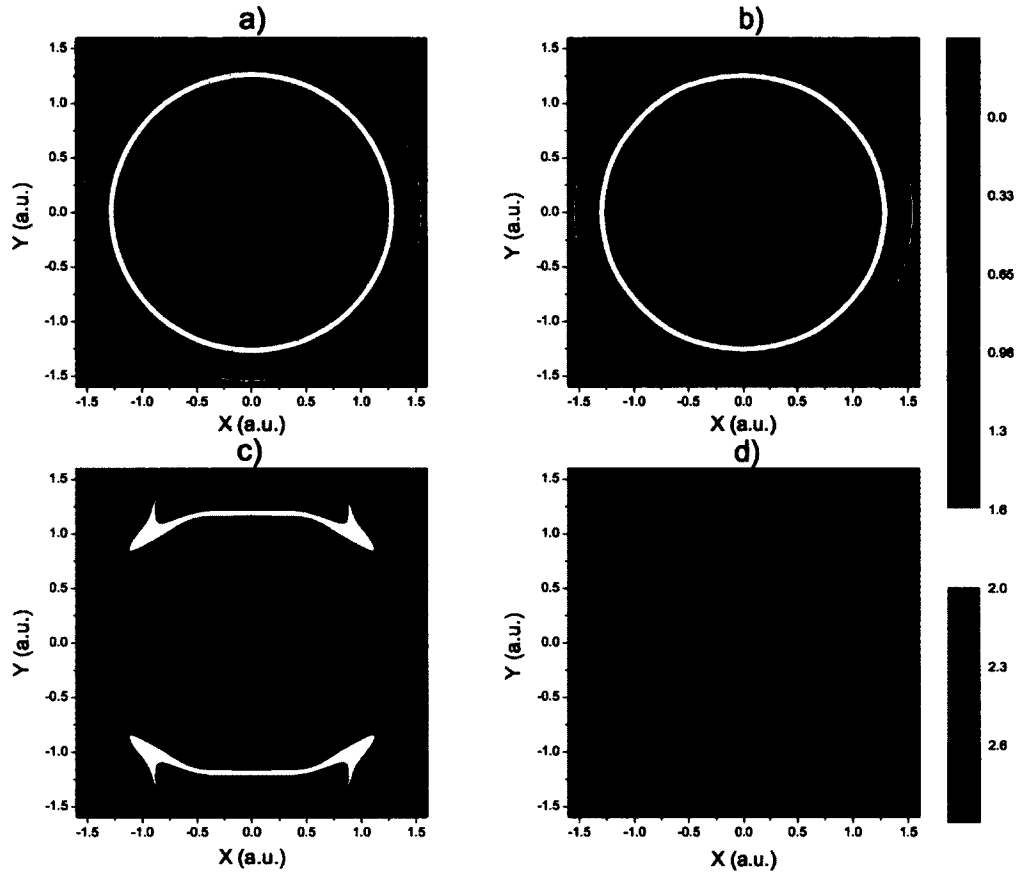

FIG. 50. The Inverse Radon transform of parabolic distribution function obtained using the filtered back projection method on the $0^0 - 180^0$ range of angles at a) 17 projections on 45 angles, b) 17 projections on 21 angles, c) 17 projections on 5 angles, and d) 5 projections on 21 angles.

As a final step, we tested the FBP method on the percentage error as introduced into test functions while performing inverse Radon transform. Similarly, as in case of Abel inversion, it could be seen that results with 5% or more percentage error should

be taken with caution. Specifically, it seems that even though the test Gaussian function is radially symmetric, the results obtained after introducing percentage error and limited number of angles (close to the real experiment) were asymmetric.

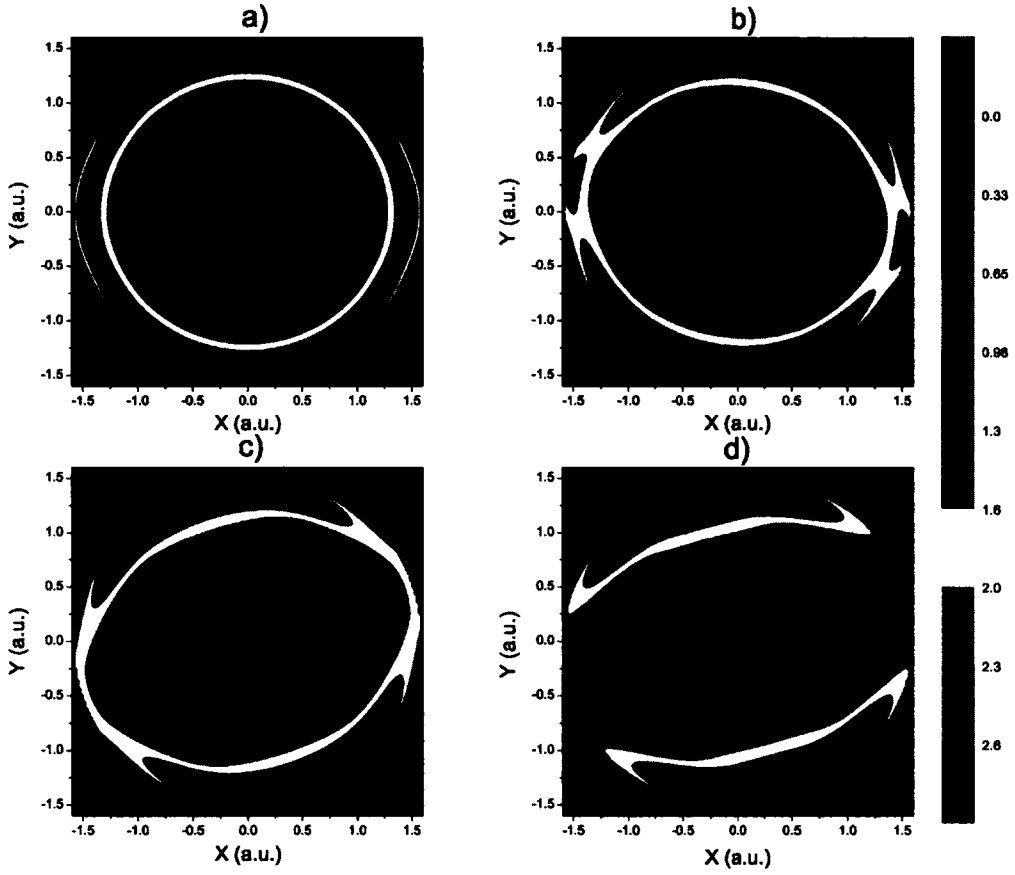

FIG. 51. The Inverse Radon transform of parabolic distribution function obtained using the filtered back projection method with the Shepp-Logan filter at 21 different angles and 17 projections at each angle on the a) $10^0 - 170^0$ interval, b) $10^0 - 150^0$ interval, c) $48^0 - 168^0$ interval, and d) $60^0 - 150^0$ interval.

We repeated the same procedure on the parabolic distribution function and obtained similar results, as shown in Figs. 50, 51, and 52. It could be seen, from the

Fig. 50 that parabolic distribution function is highly sensitive to both number of angles and number of projections. Specifically, in the case with only 5 projections, shown in Fig. 50d, we were not able to reconstruct the test function qualitatively nor quantitatively. However, it is obvious from the Fig. 50b that it was possible to reconstruct the parabolic distribution function with fair accuracy for the measurements at 17 projections and 21 angle corresponding to our experimental conditions.

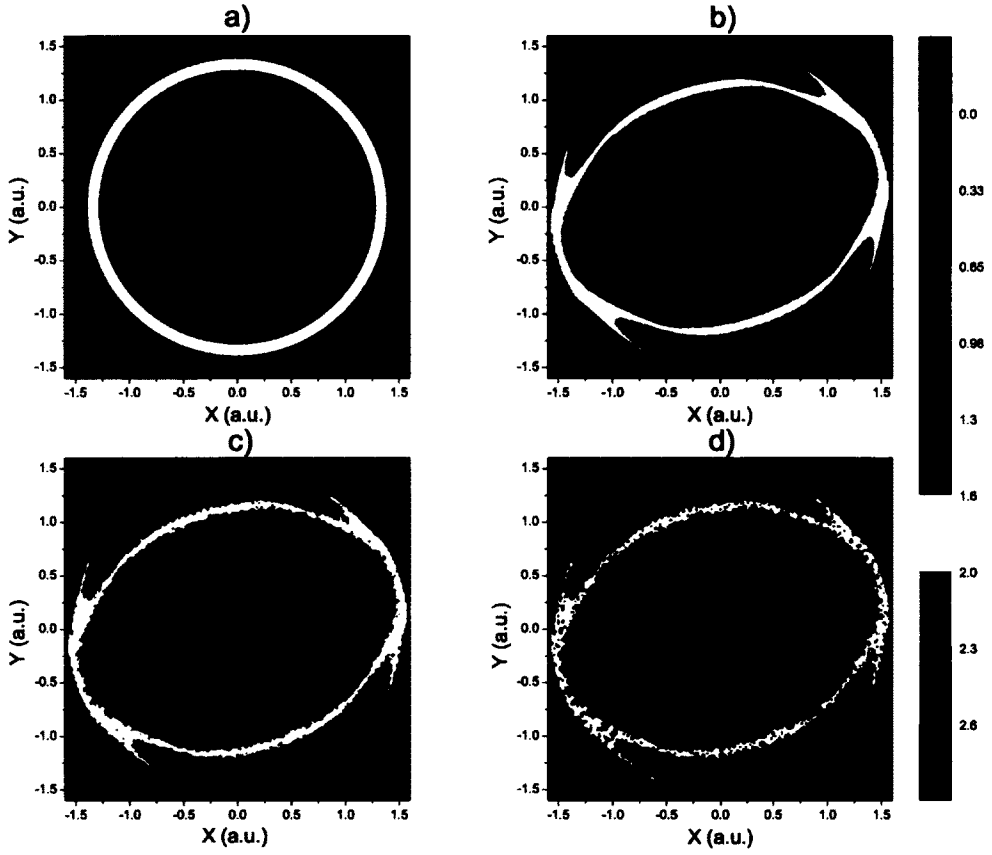

FIG. 52. Comparison between a) the original parabolic distribution function and the inverse Radon transform of the parabolic distribution function obtained using the filtered back projection method with the Shepp-Logan filter at 21 different angles and 17 projections at each angle on the $48^0 - 168^0$ interval with the b) 1% error, c) 5% error, and d) 10% error.

Figure 51 shows how the limited range of angles affects the results. Similarly, as in the case of the Gaussian distribution function, cylindrical symmetry was distorted due to the missing data. In addition, it seems that that at the rims of the circle, the values of the reconstructed function were overestimated for approximatively 10%.

The effects of percentage error on reconstructed parabolic distribution function are presented in Fig. 52. We have observed similar results as for the Gaussian distribution function, meaning that the measurements with 5% or more percentage error should be taken with caution.

4.2 LASER INDUCED FLUORESCENCE

Optical emission spectroscopy allowed us to determine a number of plasma parameters, most importantly population densities of Ar I $4p$ levels. However, obtaining population densities of the lowest-energy excited Ar I $4s$ levels requires a different optical measurement technique because the emission spectral lines from those levels are either forbidden or can be seen in the vacuum ultraviolet spectral region, only. Laser induced fluorescence (LIF) represents a good candidate since it is essentially the optical absorption spectroscopy (OAS) technique. The difference in spectral line intensities when the system is pumped by a laser and without a laser is directly proportional to the population densities of the s states. This statement will be confirmed in the following section.

LIF is a sensitive and powerful spectroscopic technique based on an absorption of laser light that is followed with a spontaneous emission after a certain period of time [49]. A laser tuned to a particular wavelength is used to excite atomic/molecular species to a certain excited state. Excited atoms/molecules will decay back to the allowed lower energy state emitting a photon at specific wavelength. In general, the emitting wavelength is different than the exciting and usually occurs at longer wavelengths. If the fluorescence is at the same wavelength as the excitation, it is called the resonant fluorescence. In this study, we have concentrated only on the effects of resonant fluorescence.

To better understand the principles of LIF, we will begin by examining a simple two-energy level model for LIF detection [49], shown in Fig. 53. It can be seen, from the Fig. 53 that LIF is characterized by four processes: laser absorption, stimulated emission, spontaneous emission, and collisional quenching of the upper level. Laser absorption is proportional to the population density of the lower energy level and the

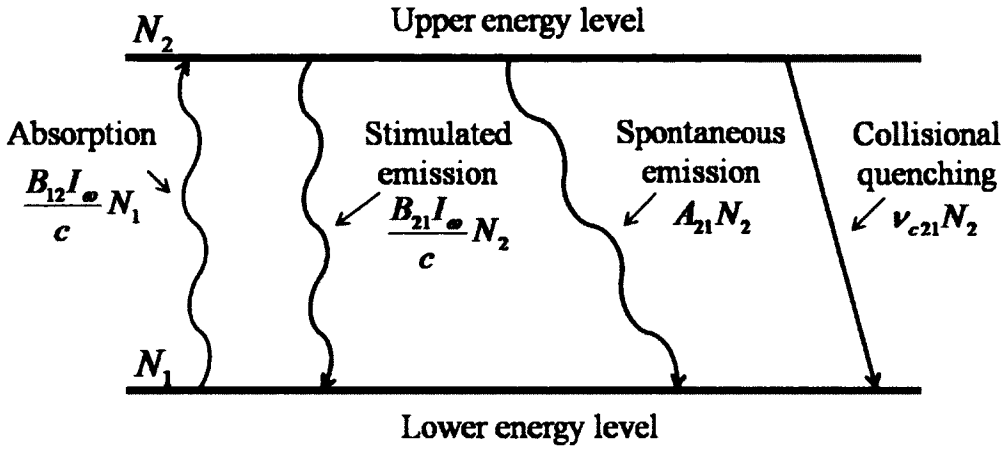

FIG. 53. Two energy level diagram for fluorescence signals.

collision rate for absorption given as [49,50]

$$\nu_{12} = \frac{B_{12}I_\omega}{c}, \tag{136}$$

where B_{12} is the Einstein coefficient for laser absorption, I_ω is the spectral irradiance (incident laser energy density), and c is the speed of light. Stimulated emission is defined in the similar way by population density of the upper level and the collision rate for stimulated emission given as

$$\nu_{21} = \frac{B_{21}I_\omega}{c}, \tag{137}$$

where B_{21} is the Einstein coefficient for stimulated emission. Spontaneous emission and collisional quenching are proportional to the product of upper state population density and Einstein coefficient (A) for spontaneous emission or collisional quenching frequency (ν_{c21}) given respectively. The rate equation of the upper energy level is described by

$$\frac{dN_2}{dt} = \left(\frac{B_{12}I_\omega}{c}\right)N_1 - \left(\frac{B_{21}I_\omega}{c}\right)N_2 - A_{21}N_2 - \nu_{c21}N_2. \tag{138}$$

In order to simplify Eq. (138), we will discuss two limits of laser operation. The first limit is the case of weak laser excitation where $\frac{B_{21}I_\omega}{c} \ll A + \nu_{c21}$ and stimulated emission can be neglected. LIF is then said to be in the linear regime since it is

linearly proportional to the laser input. In the second limit, laser absorption and stimulated emission become so large, due to the strong excitation, that the LIF signal becomes independent of laser energy density and collisional quenching. This regime is called saturation regime and it produces the highest fluorescence signal. However, it is very difficult to achieve saturation regime due to the energy spread of the focused laser beam. At the outer edges of the laser beam, the power decreases and saturation is not achieved. In addition, the temporal variation of laser intensity presents another challenge in obtaining saturation. LIF measurements in this study are made in linear regime, due to the weak laser irradiance.

After applying this simplification to the Eq. (138) it appears that the LIF contribution to the rate populations of the upper energy level comes directly from laser absorption and spontaneous emission, and the collisional quenching. The rate coefficients for collisional quenching are provided in Subsection 2.2.3. In order to obtain rates for laser absorption and spontaneous emission we need to know the laser energy density, and the Einstein coefficients for absorption and spontaneous emission. Energy density is given in Subsection 3.1.2 and is equal to $I_\omega = 1.5 \cdot 10^{-4}$ J/cm^2. Einstein coefficients are determined from the well known equations for blackbody radiation [49,50],

$$g_1 B_{12} = g_2 B_{21} \tag{139}$$

and

$$\frac{A_{21}}{B_{21}} = \frac{8\pi h}{\lambda^3}, \tag{140}$$

where g_1 and g_2 are statistical weights of the lower and upper level respectively, and λ is the wavelength that corresponds to the energy transition between two levels.

Einstein A_{21} coefficient is inversely proportional to the radiative lifetime ($A \sim 1/\tau$) of the upper level and its values for argon transitions are tabulated in literature. Since we neglected stimulated emission, the only unknown left is Einstein B_{12} coefficient for laser absorption. By combining Eqs. (139) and (140) we obtain

$$B_{12} = \frac{g_2}{g_1} \frac{A_{21}\lambda^3}{8\pi h}. \tag{141}$$

In the following section we will provide a detailed description on how laser induced fluorescence could be applied to obtain populations of Ar metastable and resonant energy levels by setting the laser wavelength exactly to the desired transition.

4.3 PLASMA KINETICS

4.3.1 KINETIC MODEL OF ARGON

To better understand complexity of argon kinetics it is necessary to first establish an understanding of the Ar atom structure. When in ground state, argon has an electron configuration $1s^2 2s^2 2p^6 3s^2 3p^6$ with shorthand notation $3p^6\ {}^1S_0$ and total angular momentum $J = 0$. From the ground state electrons in Ar atom can be excited to higher energy levels, when enough energy is added to the system. An electron transition between two energy levels is most likely to happen when the added energy is equal to the energy difference between the two levels [51]. The

TABLE 3. Configuration of energy levels of Ar I with comparison to Paschen notation.

Paschen label	Level	J	Energy (eV)
ground	$3p^6\ {}^1S_0$	0	0.0
$1s_5$	$4s[3/2]_2\ {}^3P_2$	2	11.55
$1s_4$	$4s[3/2]_1\ {}^3P_1$	1	11.62
$1s_3$	$4s'[1/2]_0\ {}^3P_0$	0	11.72
$1s_2$	$4s'[1/2]_1\ {}^1P_1$	1	11.83
$2p_{10}$	$4p[1/2]_1\ {}^3S_1$	1	12.91
$2p_9$	$4p[5/2]_3\ {}^3D_3$	3	13.08
$2p_8$	$4p[5/2]_2\ {}^3D_2$	2	13.09
$2p_7$	$4p[3/2]_1\ {}^3D_1$	1	13.15
$2p_6$	$4p[3/2]_2\ {}^3P_2$	2	13.17
$2p_5$	$4p[1/2]_0\ {}^3P_0$	0	13.27
$2p_4$	$4p'[3/2]_1\ {}^1P_1$	1	13.28
$2p_3$	$4p'[3/2]_2\ {}^1D_2$	2	13.30
$2p_2$	$4p'[1/2]_1\ {}^3P_1$	1	13.33
$2p_1$	$4p'[1/2]_0\ {}^1S_0$	0	13.48

first excited configuration of argon, $3p^5 4s$, contains 4 levels, while the second excited

configuration, $3p^5 4p$, contains 10 levels. In this work we will use Paschen notation for Ar structure due also, to its simplicity. Table 3 presents configuration of neutral Ar atom (Ar I) for the first 15 energy levels together with the Paschen notation for each corresponding level. We have employed a LK coupling term symbol notation where the orbital angular momentum of the core electrons L_1 (those that are not in an excited state) is coupled with the orbital angular momentum of the external electrons L_2 to give total orbital angular momentum L. The total orbital angular momentum L is then coupled with the spin of the core electrons S_1 to obtain the resultant angular momentum K of the final term. The spin of the core is coupled with the spin of the external electrons S_2 to obtain the total spin S. The total angular momentum is formed by $J = L + S$. The resulting symbol is in the form:

$$nl_2[K]_J \ ^{2S+1}L_J, \tag{142}$$

where nl_2 are quantum numbers of external electrons.

The first excited, $4s$, levels with $J = 1$ ($1s_2$ and $1s_4$) satisfy the selection rules ($\Delta J = \pm 1$) and decay very fast into the ground state ($J = 0$) with radiative life times of 1.96 nm and 8.4 ns, respectively [11]. These levels are called *resonant levels.* Optical transitions from the lowest levels with $J = 2$ ($1s_5$) and $J = 0$ ($1s_3$) are electric dipole forbidden, making these levels *metastable levels.*

Emissions from Ar plasma are mostly dominated by the transitions between the first two excited configurations [11], which are shown in Fig. 54. Optical emission transitions observed in our argon discharge are marked in red. For better characterization of the discharge, population densities of both upper ($4p$) and lower ($4s$) energy levels should be determined. Population densities of the upper energy levels are obtained from the intensity of the light emitted during the transition (spectral line emission intensity) as it was described in previous chapter. The hardship in obtaining population densities of Ar $4s$ states lays in the premise that they can radiatively decay only to the ground state. Resonant levels decay to the ground state in nanosecond time scale emitting light in VUV region, meaning that ultra-fast, expensive detecting systems operating in VUV region are needed for their observation. Radiative decay of metastable levels is electric dipole forbidden and they decay back to the ground state mostly through collisional quenching processes. A variety of indirect and direct methods have been developed to obtain these population densities. Direct measurements of metastable population densities include laser induced

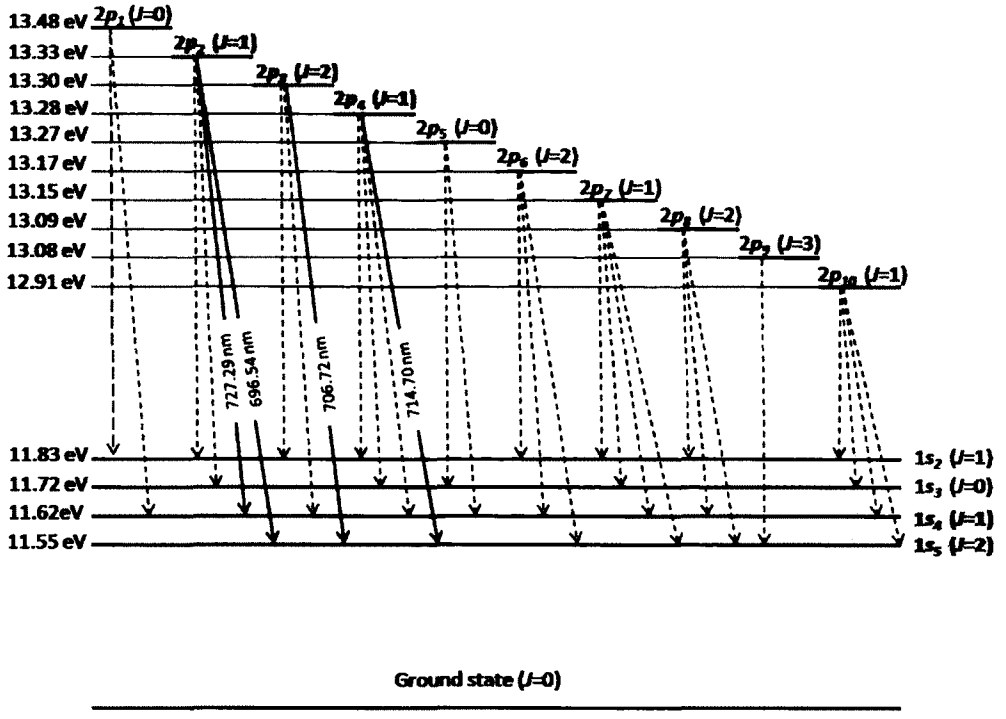

FIG. 54. Partial energy level diagram for argon. Transitions from and to the ground state are not included in this figure.

fluorescence measurements [52] or absorbtion measurements [53]. Indirect measurements include a detailed modelling of production and loss mechanisms of a specific Ar level [54, 55].

A kinetic model of Ar represents a simpler and less expensive approach in determining population densities of its metastable and resonant states. This technique is based on calculating the population rates of metastable and resonant levels by including contributions from all the processes that affect the populations of the desired states.

Before we start the kinetic analysis, we will first establish a notation system for the variables required (population densities and rate coefficients). Population densities of Ar energy levels will be marked with the capital letter N with the specification to which level is referred to given in the letter subscript. For example, the notation of the population density of the Ar metastable $1s_5$ ($J = 2$) state will be N_{s5}. We obtain

the notation for rate coefficients required for the kinetic analysis in the similar way. Rate coefficients will be marked with the small letter k with the subscript carrying the information on which type of collision between particles is involved (electron impact or collisional quenching with neutral particles). Additional information on which two particles are colliding is contained in superscript of the notation letter. For example, the rate coefficients for collisional quenching of Ar $2p_4$ ($J = 1$) state with the Ar atom in ground state is given as $k_c^{g,p4}$. To avoid redundancy, the rate coefficients for electron collision from the ground state were written as k_e^g.

Since our goal is to obtain population densities of Ar s (metastable $1s_5$, $J = 2$ and resonant $1s_4$, $J = 1$) states, we will concentrate on population density rates of Ar p states that we already know. We start by assuming a simplified model which does not include ionization and recombination processes due to their small coefficient rates and low ionization coefficient of the plasma ($\leq 10^{-4}$). Also, effects of radiation trapping can be neglected since plasma is optically thin and emission lines are little affected by reabsorbtion phenomena. According to the above assumptions, population rate of Ar $2p_x$ ($x = 1, 2, ...$) excited levels are mainly affected by these processes [11, 12, 56, 57]:

1. Electron excitation from the ground state

$$e + \mathrm{Ar}(N_n) \rightarrow e + \mathrm{Ar}(N_{px}) \tag{143}$$

$$\sim k_e^g N_e N_n$$

   where k_e^g is the corresponding coefficient rate

2. Electron excitation from the metastable and resonant levels

$$e + \mathrm{Ar}(N_{sm}) \rightarrow e + \mathrm{Ar}(N_{px}) \tag{144}$$

$$\sim k_e^{sm} N_e N_{sm}$$

   where k_e^{sm} is the corresponding coefficient rate

3. Radiative transition from higher energy levels ($4d$, $5s$, $6s$,...)

$$\mathrm{Ar}(N_{higher}) \rightarrow \mathrm{Ar}(N_{px}) + h\nu \tag{145}$$

$$\sim (1/\tau_{higher}) N_{higher}$$

   where τ_{higher} is the corresponding radiative lifetime

4. Radiative transition to metastable and resonant levels

$$\mathrm{Ar}(N_{px}) \rightarrow \mathrm{Ar}(N_{sm}) + h\nu \tag{146}$$

$$\sim (1/\tau_{sm})N_{px}$$

where τ_{sm} is the corresponding radiative lifetime

5. Quenching (collisional deactivations)

$$\mathrm{Ar}(N_n) + \mathrm{Ar}(N_{px}) \rightarrow \mathrm{Ar}(N_n) + \mathrm{Ar}(N_{sm}), \tag{147}$$

$$\sim k_c^{g,px} N_n N_{px}$$

where $k_c^{g,px}$ is the corresponding coefficient rate.

It should be noted that due to the short radiative lifetimes (< 10 ns) of resonant states, $1s_2$ and $1s_4$, their populations are much lower than the population of the $1s_3$ and $1s_5$ metastable states. Therefore, electron impact excitation from resonant states was neglected in this approximation. Further, the contributions from higher excited states of Ar are excluded from the model since the emissions from these states are reduced due to the fewer number of high-energy electrons in the plasma that are able to excite them [56,57].

The net population rate of $\mathrm{Ar}(N_{px})$ state is, then, given with

$$\frac{dN_{px}}{dt} = k_e^g N_e N_n + k_e^{s3} N_e N_{s3} + k_e^{s5} N_e N_{s5} - \sum_{m=2}^{5} \frac{1}{\tau_{sm}} N_{px} - k_c^{g,px} N_n N_{px}. \tag{148}$$

Most of the work presented in literature is limited to steady state cases ($\frac{dN_{px}}{dt} = 0$) in low pressure discharges (miliTorr pressure range) when radiative decay is the main depopulation process and quenching processes may be neglected [12,54,56,57]. The working pressure in our experiment was between 1-3 Torr suggesting that collisional quenching process involving neutrals becomes important and should be included in the model. Moreover, we will derive the equation for the steady state solution but also propose a new approach for the time-dependent calculations of Ar metastable ($1s_5$) and resonant ($1s_4$) states by applying laser induced fluorescence.

The steady state approximation states

$$\frac{dN_{px}}{dt} = 0, \tag{149}$$

and Eq. (148) becomes

$$k_e^{s3} N_e N_{s3} + k_e^{s5} N_e N_{s5} = -k_e^g N_e N_n + \sum_{m=2}^{5} \frac{1}{\tau_{sm}} N_{px} + k_c^{g,px} N_n N_{px}. \quad (150)$$

As can be seen, there are two unknown Ar I $1s$ states in Eq. (150). A possible approach is to measure population densities of two different Ar I $2p$ levels and obtain kinetic equations for each of them. As a consequence we would have two kinetic equations with two unknowns. Coupling these two equations would allow us to obtain average population densities of metastable ($1s_5$ and $1s_3$) levels. However, population densities of Ar I resonant ($1s_4$ and $1s_2$) levels can not be obtained by applying this approach.

In general case, when it is possible to observe the time dependence of Ar ($2p_x$) levels, a differential equation (148) could be solved numerically. When the observed level is pumped by a laser from the desired resonant or metastable level, the new balance equation would look similar to the Eq. (148) with the addition of an extra term due to the laser absorption (as described in previous section),

$$\begin{aligned} \frac{dN'_{px}}{dt} = {} & k_e^g N_e N_n + k_e^{s3} N_e N_{s3} + k_e^{s5} N_e N_{s5} \\ & - \sum_{m=2}^{5} \frac{1}{\tau_{sm}} N'_{px} - k_c^{g,px} N_n N'_{px} \\ & + \frac{B_{12} I_\omega}{c} N_{sm}, \end{aligned} \quad (151)$$

where B_{12} is Einstein coefficient for laser absorption and I_ω is laser spectral irradiance. It should be noted that N_{sm} corresponds to the lower level N_1 and N_{px} corresponds to the upper level N_2 in the Eq. (138).

Since the laser pulse duration was 3-5 ns and measurements were taken in 20 μs time intervals, we assumed that, due to the microsecond time averaging, populations of metastable and resonant levels remained the same. With this assumption in mind and after subtracting Eq. (148) from Eq. (151) we have obtained

$$\begin{aligned} \frac{d}{dt}(N'_{px} - N_{px}) = {} & -\sum_{m=2}^{5} \frac{1}{\tau_{sm}} (N'_{px} - N_{px}) - k_c^{g,px} N_n (N'_{px} - N_{px}) \\ & + \frac{B_{12} I_\omega}{c} N_{sm}. \end{aligned} \quad (152)$$

Hence, the population of the resonant/metastable level is equal to

$$\frac{B_{12} I_\omega}{c} N_{sm} = \frac{d}{dt}(N'_{px} - N_{px}) + \Big(\sum_{m=2}^{5} \frac{1}{\tau_{sm}} + k_c^{g,px} N_n \Big) (N'_{px} - N_{px}). \quad (153)$$

In steady state case, Eq. (153) becomes

$$N_{sm} = \frac{c \cdot \left(\sum_{m=2}^{5} 1/\tau_{sm} + k_c^{g,px} N_n \right)}{B_{12} I_\omega} (N'_{px} - N_{px}), \tag{154}$$

and can be solved analytically. It could be seen from the Eqs. (153) and (154) that the population densities of resonant/metastable argon levels are directly proportional to the difference between spectral line intensities (population densities of N_{px} levels) when the laser is on (N'_{px}) and when there is no laser (N_{px}).

4.3.2 KINETIC MODEL OF NITROGEN

Nitrogen spectroscopy is often used as a diagnostic tool for characterization of air discharges, due to its abundance. Therefore, we have studied molecular structure of pulse repetitive discharge in air, described in Section 3.2, by analyzing vibrational spectra of certain nitrogen bands. In previous section we have described how the kinetic model of Ar I can be applied to calculate time dependent population densities of argon metastable/resonant $4s$ levels. In this section we will show a simple but accurate kinetic model of nitrogen molecular bands employed to obtain time resolved electron densities. In defining the time-dependent kinetics of nitrogen we start by assuming a simplified model based on the spectral intensities of certain nitrogen bands. In particular, we focuse on the Second Positive System band intensity $C^3\Pi_u \rightarrow B^3\Pi_g$ (0-0) at 337.1 nm. Energy level diagram of neutral N_2 levels included in the kinetic model is shown in Fig. 55.

Again, as in the case of argon discharge, we did not include ionization and recombination processes due to their small coefficient rates and low ionization coefficient of the plasma ($\leq 10^{-4}$). Further, resonant transitions from the excited states of the carrier gas to N_2 ($C^3\Pi_u$) state that would increase its population density are excluded from this model. There are various examples in literature including the work of Kim et al. [58] and Zhu et al. [59] that support these assumptions. Acknowledging these restrictions we can state that nitrogen excited electronic state ($C^3\Pi_u$) is affected mainly by three processes [60, 61]:

1. Electron excitation from the ground state

$$e + N_2(X^1\Sigma^+) \rightarrow e + N_2(C^3\Pi_u) \tag{155}$$

$$\sim k_e^{X(0)} N_e N_{n(0)}$$

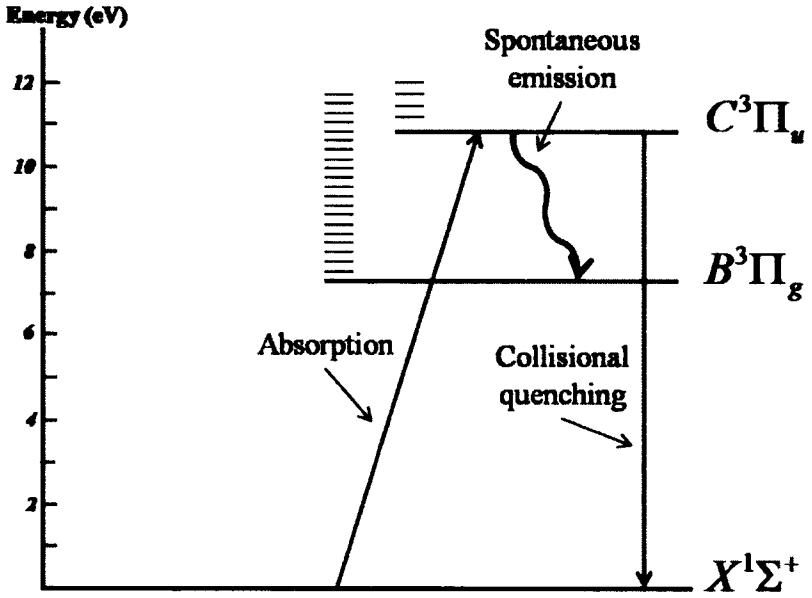

FIG. 55. Energy level diagram for N_2 levels included in the kinetic model.

where $k_e^{X(0)}$ is the corresponding coefficient rate

2. Radiative transition to $B^3\Pi_g$ level

$$N_2(C^3\Pi_u) \rightarrow N_2(B^3\Pi_g) + h\nu \tag{156}$$

$$\sim (1/\tau_{CB}) N_{C(0)}$$

where τ_{CB} is the corresponding radiative lifetime

3. Quenching (collisional deactivations)

$$N_2(C^3\Pi_u) + N_2(X^1\Sigma^+) \rightarrow 2N_2(X^1\Sigma^+). \tag{157}$$

$$\sim k_c^{X(0),C(0)} N_{n(0)} N_{C(0)}$$

where $k_c^{X(0),C(0)}$ is the corresponding coefficient rate.

Among these transitions, only transitions involving the vibrational ground state of each electronic state are considered. However, experimental data indicated that some transitions involving levels other than vibrational ground states are significant enough to be included in the kinetic model. They are:

(a) Vibrational excitation/deexcitation by electron impact (e-V) from the ground vibrational level (v=0) of $N_2(C^3\Pi_u)$

$$e + N_2(C^3\Pi_u, 0) \rightleftharpoons e + N_2(C^3\Pi_u, v),\ v = 1, 2, ... \tag{158}$$
$$\sim k_e^{C(0)} N_e N_{C(0)}$$

where $k_e^{C(0)}$ is the corresponding coefficient rate.

(b) Vibration-vibration collision processes (V-V)

$$N_2(C^3\Pi_u, 0) + N_2(C^3\Pi_u, v) \rightleftharpoons$$
$$N_2(C^3\Pi_u, 1) + N_2(C^3\Pi_u, v-1)$$
$$v = 2, 3, ... \tag{159}$$
$$\sim k_c^{C(0),C(v)} N_{C(0)} N_{C(v)}$$

where $k_e^{C(0),C(v)}$ is the corresponding coefficient rate.

When the above processes are included, the net population rate of the $N_2(C^3\Pi_u)$ state is given with

$$\begin{aligned}\frac{dN_{C(0)}}{dt} &= k_e^{X(0)} N_e N_{n(0)} - \frac{N_{C(0)}}{\tau_{CB}} - k_c^{X(0),C(0)} N_{n(0)} N_{C(0)} \\ &\quad - \sum_v k_e^{C(0)} N_e N_{C(0)} + \sum_v k_e^{C(v)} N_e N_{C(v)} \\ &\quad - \sum_v k_c^{C(0),C(v)} N_{C(0)} N_{C(v)} + \sum_v k_c^{C(1),C(v-1)} N_{C(1)} N_{C(v-1)},\end{aligned} \tag{160}$$

where we applied similar notation system as in the case of argon. Population densities of N_2 energy levels were labelled the same way as before with the additional information on vibrational structure given in apprentices. For example, population density of $N_2(C^3\Pi_u)$ ($v = 0$) state was written as $N_{C(0)}$. The same was applied to rate coefficients. Rate coefficient for collisional quenching of $N_2(C^3\Pi_u)$ ($v = 0$) state with N_2 in ground state $N_2(X^1\Sigma^+)$ ($v = 0$) was given as $k_c^{X(0),C(0)}$.

We have assumed Boltzmann distribution of vibrational state population which we will prove valid using our experimental data

$$N_{C(v)} = N_{C(0)} e^{-\frac{E_{v0}}{k_B T_v}}, \tag{161}$$

where E_{v0} is transition energy between $N_2(C_v)$ state and $[N_2(C_{v=0})]$ state, T_v is corresponding vibrational temperature and k_B is Boltzmann constant. We will also

demonstrate by using our experimental data that both e-V and V-V processes (the last three terms of Eq. (160)) are negligible comparing to the electronic transitions of $N_2(C^3\Pi_u)$ state (the first four terms of Eq. (160)).

Pancheshnyi et al. [62] investigated a detailed kinetic model of nitrogen discharges by including the quenching process between ground state oxygen molecules and $N_2(C^3\Pi_u)$ state

$$N_2(C^3\Pi_u) + O_2 \rightarrow N_2(X^1\Sigma_g^+) + O + O. \tag{162}$$

According to Ref. [62], the quenching rate of the C state in collisions with oxygen molecules is $2.7\times10^{-10}\text{cm}^3/\text{s}$, and the quenching rates in the collisions with nitrogen molecules is $(9 \pm 3) \times 10^{-10}\text{cm}^3/\text{s}$. In the extreme case that all oxygen molecules from the air remain in their ground state, unattached, and not dissociated, reaction (162) would contribute by less then 10% to the overall quenching of the C state. This contribution is within the error of nitrogen-induced quenching rate, and may be neglected without increasing the error of the final result. Therefore, the kinetic model for nitrogen was used in order to avoid complication with N_2/O_2 mixture. The effect of oxygen was introduced as a small error of the analysis.

We will start with an analytic form of the kinetic model, using the approximation that the electron density and $N_2(C^3\Pi_u)$ population are constant. Assuming that the population of the upper energy level $[N_2(C^3\Pi_u)]$ does not change in time and that contributions from vibrational transitions are negligible, we derive the solution for the steady state from

$$\frac{dN_{C(0)}}{dt} = 0. \tag{163}$$

After combining relations (160) and (163), neglecting the contribution of upper vibrational levels (last four terms in Eq. (160)), we obtained the electron density relation to be

$$k_e^{X(0)} N_e N_{n(0)} = \frac{N_{C(0)}}{\tau_{CB}} + k_c^{X(0),C(0)} N_{n(0)} N_{C(0)}. \tag{164}$$

Thus,

$$N_e = N_{C(0)} \frac{1 + \tau_{CB} k_c^{X(0),C(0)} N_{n(0)}}{\tau_{CB} k_e^{X(0)} N_{n(0)}}. \tag{165}$$

Generally, one can solve numerically Eq. (160) for any input power function provided that a waveform for $k_e(E/N_n(t))$ is established. Hence,

$$\frac{dN_{C(0)}}{dt} = k_e^{X(0)}(t) N_e(t) N_{n(0)} - \frac{N_{C(0)}(t)}{\tau_{CB}} - k_c^{X(0),C(0)} N_{n(0)} N_{C(0)}(t). \tag{166}$$

Substituting

$$N_{C(0)} = x \tag{167}$$

$$N_{n(0)} = const = A \tag{168}$$

and

$$\frac{1}{\tau_{CB}} + k_c^{X(0),C(0)} N_{n(0)} = const = \omega, \tag{169}$$

we can express the Eq. (166) in a simplified form

$$\frac{dx}{dt} + \omega x = A k_e^{X(0)}(t) N_e(t). \tag{170}$$

From the Eq. (170) follows that the kinetics of $N_2(C^3\Pi_u)$ state, i.e. measured population density waveform and its first derivative, can be used in determination of time-resolved electron density of the plasma.

CHAPTER 5

RESULTS

Microwave discharges that operate at low pressures and high densities have proved to be an attractive choice for plasma etching and cleaning purposes. The extensive research necessary for characterization of these discharges requires a complete set of plasma parameters obtained under the different MW plasma regimes. For that reason, we have provided full parametric description of two types of MW discharges, a supersonic flowing Ar discharge and a pulse-repetitive air discharge.

The common property of these MW discharges is that they are far from thermodynamic equilibrium, meaning that all particles (atoms in ground state, excited atoms, and electrons) are described with different temperatures. Since these plasmas are weakly ionized (ionization coefficient less than 1%) implying that particles in these discharges are mostly neutral in the ground state, it is reasonable to assume the gas density and gas kinetic temperature to be equal to density and temperature of neutral particles in the ground state. We will also assume that the gas kinetic temperature is equal to the rotational temperature of diatomic molecules in the discharge. This assumption is valid if the molecular electronically excited states are produced by direct electron excitation from the ground state, whereby the rotational energy structure is conserved.

Employing different diagnostic techniques (plasma tomography, laser induced fluorescence) allowed us to resolve spatial and time characteristics of plasma parameters providing us, in that way, with full control and optimization of parameters required for plasma processing.

This section is organized as follows. Firstly, we define molecular (rotational and vibrational) structure of N_2 Second Positive System (SPS) $C^3\Pi_u \rightarrow B^3\Pi_g$ and determine the corresponding temperatures, since the structure of N_2 defines the plasma structure. Secondly, we derive gas temperatures and gas densities of both discharges described in this study. Thirdly, we evaluate population densities of excited particles. In the case of argon discharge we are providing both time and space resolved data, while in case of air discharge just the time resolved population waveforms will

be presented. Finally, we will discuss electron temperature and density of both discharges. In addition, time resolved Ar metastable/resonant population densities will be obtained by employing LIF.

5.1 ROTATIONAL TEMPERATURE

Molecular structure of MW plasmas was studied in pulse-repetitive air discharge by observing N_2 molecular bands, in particular Second Positive System band intensity $C^3\Pi_u \rightarrow B^3\Pi_g$ (0-0) at 337.1 nm. Since molecules are characterized with vibrational and rotational levels besides electronic configuration, we start by describing time averaged parameters that characterize vibrational and rotational nature of molecules (the vibrational temperature, of vibrationally excited $N_2(C^3\Pi_u)$ states, and the rotational temperature).

The importance of rotational temperature lays in the premise that it could be a good indicator of the gas temperature, one of the key parameters in driving the reaction rates of many processes. There are examples in literature [63,64] confirming this assumption for the case of SPS $C^3\Pi_u \rightarrow B^3\Pi_g$, $\Delta v = 2$ molecular band. In the Nitrogen Second Positive System the rotational spectrum consists of three branches: P, Q, and R. Both P and R branches are split into three sub-branches and the Q branch into two due to the triplet splitting of the rotational quantum number J. We have chosen to use Δv=2 vibrational sequence from the R_2 branch of the $C^3\Pi_u \rightarrow B^3\Pi_g$ band, since there is minimal self absorption and there is no interference from other atomic lines or molecular bands. Furthermore, we have employed only lines with higher J values, since they are less self absorbed than those at lower values.

We start by defining the rotational term values, $F_{\Omega,J}$ ($\Omega = 0, 1, 2$), for triplet (Π) states of any vibrational level v. These rotational terms may be expressed by the semi-empirical formula [65] given as

$$\begin{aligned} F_{0,J} &= B_v[J(J+1) - \sqrt{Z_1} - 2Z_2] - D_v(J - \frac{1}{2})^4 \\ F_{1,J} &= B_v[J(J+1) + 4Z_2] - D_v(J + \frac{1}{2})^4 \\ F_{2,J} &= B_v[J(J+1) + \sqrt{Z_1} - 2Z_2] - D_v(J + \frac{3}{2})^4, \end{aligned} \tag{171}$$

where B_v and D_v are rotational constants, Y_v is a spin-axis coupling constant listed

in Table 4 [66], and

$$Z_1 = Y_v(Y_v - 4) + \frac{4}{3} + 4J(J+1) \quad (172)$$

$$Z_2 = \frac{1}{3Z_1}[Y_v(Y_v - 4) - \frac{4}{9} - 2J(J+1)]. \quad (173)$$

TABLE 4. Values of the constants for the evaluation of rotational terms of N_2 SPS [63].

	$C^3\Pi_u$			$B^3\Pi_g$		
v	B_v	Y_v	$D_v \times 10^6$	B_v	Y_v	$D_v \times 10^6$
0	1.815	21.5	6.7	1.628	25.9	6.4
1	1.793	21.5	6.8	1.610	26.2	6.5
2	1.769	21.4	7.3	1.592	26.4	6.7
3	1.740	21.1	8.5	1.574	26.8	6.8
4	1.700	20.3	12.5	1.555	27.0	6.9

The difference between rotational terms of two vibration levels $v' - v''$ ($C^3\Pi_u$ to $B^3\Pi_g$) is proportional to the wavenumber of the rotational lines as

$$\nu = \nu_0 + F'_{J'} - F''_{J''}, \quad (174)$$

where ν_0 is the band origin (band head) of the system, F' and F'' are the rotational terms for the upper and lower levels, respectively and J' and J'' are corresponding rotational numbers. After applying selection rules ($\Delta J = 0, \pm 1$) we obtain three rotational branches

- P branches (Ω = 0,1,2)

$$\nu^P_{\Omega,J''} = \nu_0 + F'_{\Omega,J''-1} - F''_{\Omega,J''} \quad (175)$$

- Q branches (Ω = 1,2)

$$\nu^Q_{\Omega,J''} = \nu_0 + F'_{\Omega,J''} - F''_{\Omega,J''} \quad (176)$$

- R branches (Ω = 0,1,2)

$$\nu^{R}_{\Omega,J''} = \nu_0 + F'_{\Omega,J''+1} - F''_{\Omega,J''} \tag{177}$$

where J'' is the rotational quantum number of the lower level v''.

We have converted these wavenumbers into wavelengths and calculated Fortrat diagrams, by employing above equations, for the N_2 (0-2) band with bandwidth at λ = 380.47 nm, as shown in Fig. 56. Fortrat diagrams presented in Fig. 56 allowed us to identify the rotational bands associated with specific quantum number.

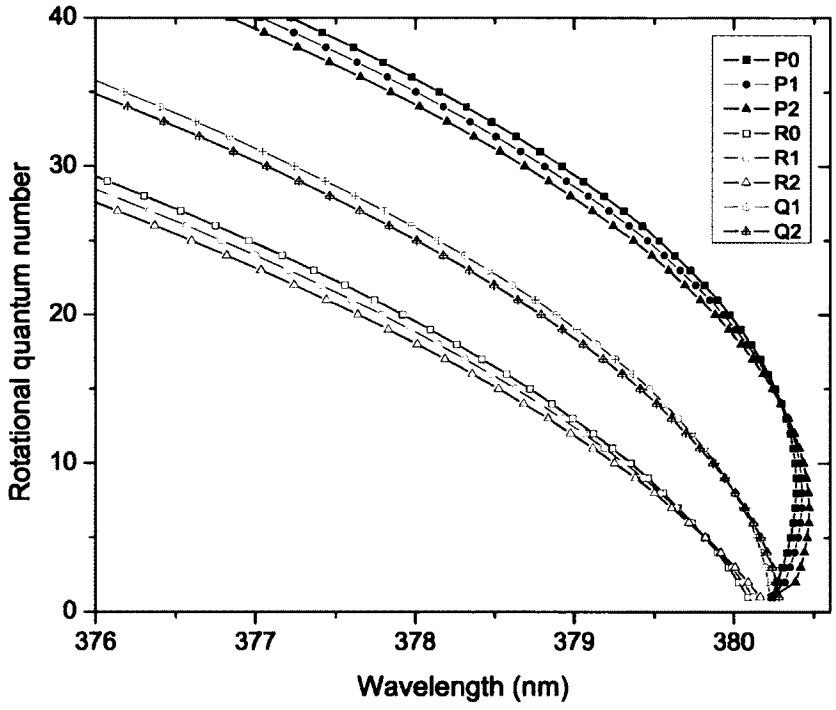

FIG. 56. Fortrat diagram of $N_2C^3\Pi_u \rightarrow B^3\Pi_g$ second positive system.

As we have already mentioned in Subsection 4.3.2, the electronically excited states, $N_2(C^3\Pi_u)$, are mostly produced by direct electron excitation from the ground, $N_2(X^1\Sigma^+_g)$, state. This implies that the rotational population distribution of the excited $(C^3\Pi_u)$ level corresponds to the population distribution of the ground state at

particular rotational temperature T_r. Ground state population distribution, and thus ($C^3\Pi_u$) level population distribution $f_{J'}$ satisfies Boltzmann distribution law, given as

$$f_{J'} = (2J'+1)\exp\Big(-J'(J'+1)\frac{hc}{kT_r}\Big), \tag{178}$$

where J' is the rotational quantum number of the excited state v', h is Plank's constant, c is the speed of light, B_x is the rotational constant for the ground state (1.9898 cm^{-1}), and k is the Boltzmann constant. Dividing $f_{J'}$ by the partition function

$$Q = \sum_{J'} f_{J'} \tag{179}$$

leads to the normalized population, $P_{J'}$,

$$P_{J'} = f_{J'}/Q. \tag{180}$$

Normalized population, $P_{J'}$, is distributed between the P, Q and R branches through the Hönl-London factors (line strengths). For the N_2 SPS [65] they are given with

$$S^P_{\Omega,J'} = \frac{(J'+1+\Omega)(J'+1-\Omega)}{J'+1} \tag{181}$$

$$S^Q_{\Omega,J'} = \frac{(2J'+1)\Omega^2}{J'(J'+1)} \tag{182}$$

$$S^R_{\Omega,J'} = \frac{(J'+\Omega)(J'-\Omega)}{J'} \tag{183}$$

and they obey the sum rule

$$\sum_{\Omega}(S^P_{\Omega,J'} + S^Q_{\Omega,J'} + S^R_{\Omega,J'}) = 2J'+1. \tag{184}$$

Combining the above equations, normalized intensity of any line for the branch i (i = P, Q, R) is determined to be

$$I^i_{\Omega,J'} = S^i_{\Omega,J'}\frac{1}{Q}\exp\Big(-J'(J'+1)\frac{hcB_x}{kT_r}\Big). \tag{185}$$

While Eq. (185) gives the theoretical prediction of the normalized line intensity, the observed spectral lines are always broadened due to the different broadening mechanisms in the gas discharge. The main contribution to spectral broadening in gas discharges at low pressures comes from Doppler broadening, which is due to the thermal motion of absorbing and emitting particles [67].

For particles moving with a velocity v, transition frequencies will differ from those of particles at rest as

$$\nu = \nu_0(1 \pm \frac{v}{c}), \tag{186}$$

where ν_0 are transition frequencies for particles at rest. The broadened spectral line distribution $W^i_\Omega(\nu)$ around the center frequency, ν_0, is given by Gaussian distribution function

$$W^i_\Omega(\nu) = I^i_{\Omega,J'}\exp\Big(-\frac{mc^2(\nu-\nu_0)^2}{2kT_r\nu_0^2}\Big), \tag{187}$$

where m is the mass of the particle. The function full width at the half maximum (FWHM) of Gaussian distribution function is given by

$$\delta\nu_D = \Big(\frac{2\pi\nu_0}{c}\Big)\sqrt{8ln(2)\frac{kT_r}{m}}, \tag{188}$$

or in terms of wavelengths

$$\delta\lambda_D = \lambda_0\sqrt{8ln(2)\frac{kT_r}{mc^2}}. \tag{189}$$

In addition to Doppler broadening, instrumental broadening due to the limited resolution of the experimental apparatus was also present. The result of instrumental broadening is again Gaussian lineshape. Therefore, the total FWHM of the spectral line is

$$\delta\lambda_G = \delta\lambda_D + \delta\lambda_I, \tag{190}$$

where $\delta\lambda_I$ comes from instrumental broadening.

Normalized intensity, Eq. (187), can be expressed in terms of $\delta\lambda_G$ and has the form of

$$W^i_\Omega(\lambda) = \frac{1}{\delta\lambda_G}I^i_{\Omega,J'}\exp\Big(-\frac{(\lambda-\lambda_0)^2}{{\lambda_G}^2}\Big), \tag{191}$$

Normalized rotational spectrum intensity is given as the sum of all normalized intensities

$$W(\lambda) = \sum_{i,\Omega} W^i_\Omega(\lambda). \tag{192}$$

We have employed Eq. (192) to numerically obtain synthetic rotational spectra. As it can be seen, the only unknown in the equation is the rotational temperature T_r, which is used as a free parameter. By comparing experimentally obtained spectra with theoretically simulated synthetic spectra we were able to estimate T_r when the discrepancies between spectra were minimal.

As an additional test of the applied method we have used Eq. (178) to obtain an exponential fit of the experimentally observed normalized line intensities $f_{J'}/(2J'+1)$ versus $J'(J'+1)$ to obtain rotational temperature from the slope of the fit. Furthermore, this allowed us to confirm whether rotational population distributions satisfy Boltzmann distribution by falling on the line of the fit.

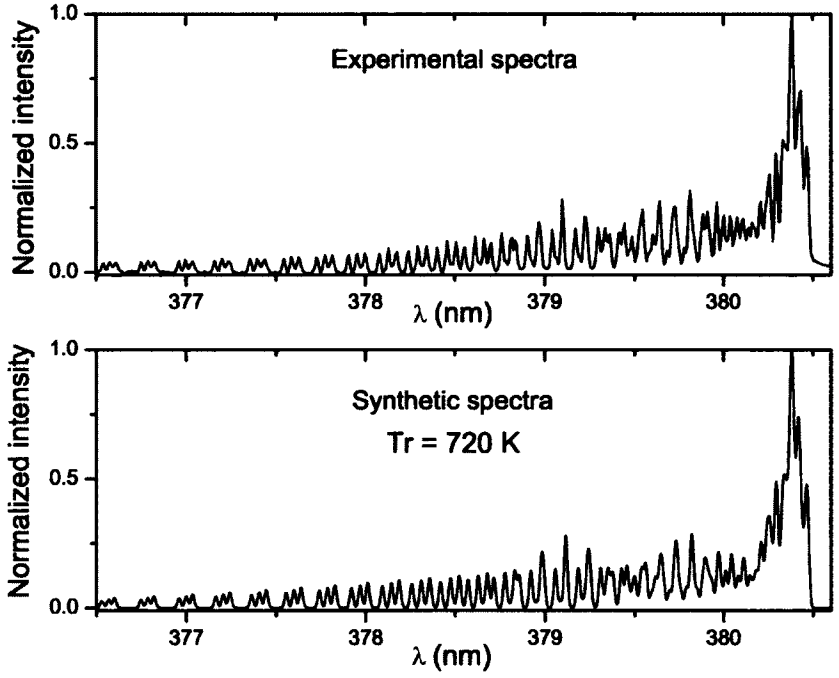

FIG. 57. Comparison between the experimental and synthetic spectra of Nitrogen Second Positive System at 11.8 Torr in air discharge.

Figure 57 shows comparison between the experimental and synthetic spectra of Nitrogen Second Positive System Δv=2 vibrational sequence from the R_2 branch at pressure $p = 11.8$ Torr in air discharge. The discrepancies between the two spectra were estimated to be less than 5%. Instrumental spectral line broadening was $\delta\lambda_I = 0.01$ nm and obtained rotational temperature was $T_r = 720 \pm 70$ K. Experimental errors were evaluated from the measurement errors combined with the error due to discrepancies between two spectra. We have compared this temperature to rotational

temperature $T_r = 750 \pm 70$ determined from the slope of the Boltzmann distribution, as shown in Fig. 58. As can be seen, the results stand in good agreement within the evaluated error. Furthermore, Fig. 58 shows that semi-logarithmic character of Boltzmann plot is satisfied by all line intensities with higher J' values (J'>15).

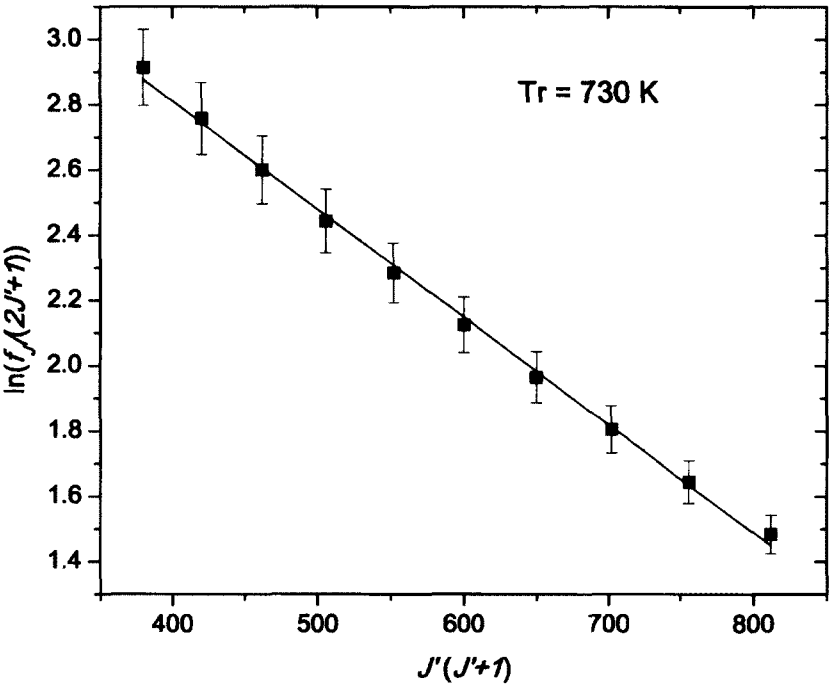

FIG. 58. Rotational temperature obtained from the linear fit (full line) of the natural logarithm of normalized line intensities versus $J'(J'+1)$ of the R_2 branch of Nitrogen Second Positive System at 11.8 Torr in air discharge. Experimental errors are indicated with error bars.

Similarly, we have obtained rotational temperatures at different pressures and presented them in Table 5. It seems that the rotational temperature decreases with the pressure increase.

Since supersonic flowing MW discharge was sustained in pure argon, we were not able to study molecular structure of this discharge. However, previous work [68] on this experiment included measurements in argon with the addition of 5% air.

TABLE 5. Rotational temperatures obtained from the Nitrogen Second Positive System at different pressures in air discharge, generated with the same MW power.

Pressure (Torr)	Rotational temperature (K)
10.0	740±70
11.8	720±70
13.0	690±70
20.0	600±60

Even though, introducing a small amount of air would change the dynamics of the discharge, the results obtained in this way could still serve as good indicators of rotational and thus gas kinetic temperature in our study. According to Ref. [68] estimated rotational temperature at pressure $p = 2.3$ Torr was $T_r = 1550 \pm 50$ K.

5.2 VIBRATIONAL TEMPERATURE

Knowledge of the vibrational temperature is fundamental for understanding the physical and chemical processes in the N_2 and N_2-mixture discharges because vibrational temperature provides an insight in to the vibration-vibration and vibration-translation energy exchange processes. Moreover, the time scale of the microwave pulses in the case presented in Section 3.2 is long enough for the distribution of vibrational state populations of the $N_2(C^3\Pi_u)$ states to be expressed by the vibrational temperature T_v as a single statistical parameter by using the Eq. (161) for Boltzmann distribution. Thus, it was necessary for further analysis to determine the value of the vibrational temperature.

In order to minimize the error due to the self-absorption, we have chosen to use N_2 SPS ($C^3\Pi_u \rightarrow B^3\Pi_g$), $\Delta v = 2$ transition for determination of the vibrational temperature. By assuming that a Boltzmann factor is applicable to the limited number of the observed vibrational states we have introduced the proportionality equation

$$I_{v'v''} \approx A_{v'v''}\nu_{v'v''}e^{-\frac{G_0(v')hc}{kT_v}}, \tag{193}$$

where $I_{v'v''}$ is the spectral line intensity, $A_{v'v''}$ is the Frank-Condon factor for the transition between the upper (v') and lower (v'') state [66], $\nu_{v'v''}$ is the transition

frequency, $G_0(v')hc$ is the energy of the vibrational level. It is defined as [65]

$$G_0(v') = \omega_e(v' + \frac{1}{2}) - \omega_e x_e(v' + \frac{1}{2})^2 + \omega_e y_e(v' + \frac{1}{2})^3 + \omega_e z_e(v' + \frac{1}{2})^4, \quad (194)$$

where T_v is the vibrational temperature. Using the Boltzmann plot, similar to the determination of rotational temperature, the vibrational temperature was found to be $T_v = (3300 \pm 200)$ K at pressure $p = 11.8$ Torr. Experimental error was evaluated from the measurement errors.

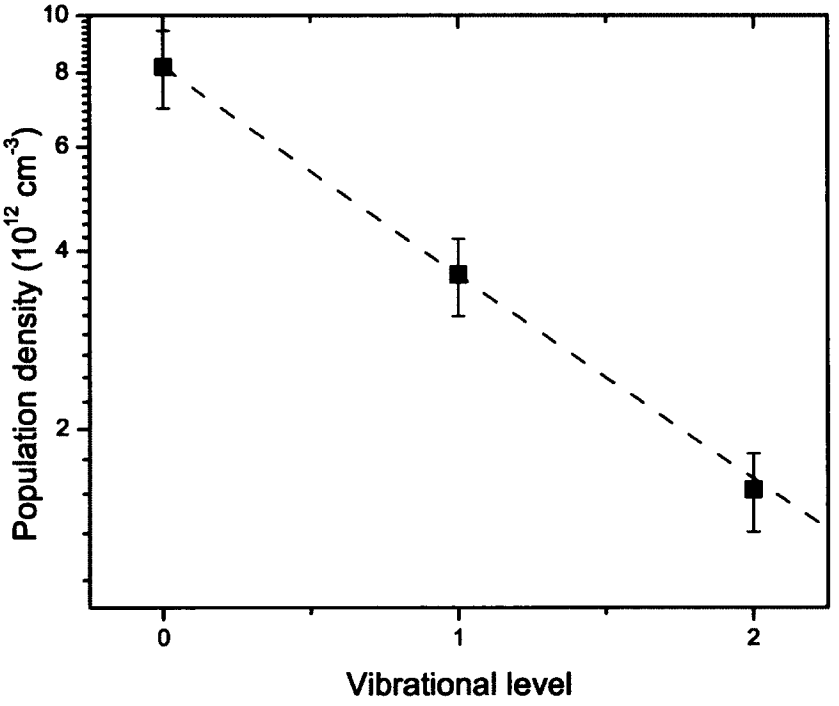

FIG. 59. Comparison between the vibrational population distribution of N_2 ($C^3\Pi_u$) states measured from emission spectrum and the values of the population distributions calculated from Boltzmann distribution, Eq. (81), at T_v=3300 K.

By applying the relationship between spectral line intensity and the population density of the upper level given by Eq. (81) we have obtained population densities

for the first three vibrational levels of the $C^3\Pi_u$ state. Figure 59 shows vibrational distribution of $C^3\Pi_u$ state for the first three vibrational levels obtained from absolute intensities of the bands belonging to $\Delta v = 2$ sequences. It fits very well with the Boltzmann distribution justifying the assumption of the V-V equilibrium.

5.3 GROUND-STATE POPULATIONS

In weakly ionized plasmas (degree of ionization less than 1%), ground state population N_n can be approximated with the neutral particle density and is determined from the ideal gas equation

$$N_n = \frac{p}{kT_g}, \tag{195}$$

where p is the pressure in the static cell, N_n is the ground-state number density (in cm^{-3}) and T_g is the gas kinetic temperature. We have assumed that gas kinetic temperature is equal to the rotational temperature of molecules in the discharge since the molecular excited states are produced by direct electron excitation from the ground state.

Using the measured gas temperature and knowing the pressure in chamber, we employ Eq. (195) and calculate ground-state number density in pulse repetitive discharge in air, described in Section 3.2. The results are shown in Table 6.

TABLE 6. Ground-state populations obtained from the Nitrogen Second Positive System at different pressures in air discharge.

Pressure (Torr)	Ground-state populations (10^{17} cm^{-3})
10.0	1.3±0.2
11.8	1.6±0.2
13.0	1.8±0.2
20.0	3.2±0.4

It can be seen from the table that ground-state population densities increase with the pressure increase. This is understandable since rotational temperature and, correspondingly, gas kinetic temperature decrease when the pressure increases.

In the case of supersonic flowing discharge in argon, described in Section 3.1,

we were able to estimate the gas density by adding a small amount of nitrogen and assuming the rotational temperature (i.e. gas kinetic temperature) from the above section. After employing Eq. (195) for given temperature, we determined gas density $N_n = (1.4 \pm 0.2) \times 10^{16}$ cm^{-3} at pressure $p = 2.3$ Torr. Note, that errors in obtaining ground state populations are evaluated from experimental errors due to gas temperature and pressure measurements.

5.4 POPULATION DENSITIES OF EXCITED LEVELS

The kinetics of excited particles is one of the key characteristics in low-temperature gas discharges. Detailed investigation of these excited particles can lead to better understanding of radiative and chemical properties of discharges and improve the applications of optical diagnostic methods [12, 69]. In this section, we employ Eq. (81) and the method described in Chapter 3 to obtain the population densities of the atom/molecule upper energy levels from the measured spectral line intensities.

5.4.1 PULSE-REPETITIVE AIR DISCHARGE

We have observed time-resolved emission spectra from the N_2 ($C^3\Pi_u \rightarrow B^3\Pi_g$) (0-0) transition in pulse-repetitive air discharge. Employing Eq. (81) that relates population density of the upper energy level to the measured spectral line intensity, described in Subsection 3.1.2, allowed us to determine the population densities of the upper $C^3\Pi_u$ level at different pressures, as shown in Fig. 60.

It can be seen in Fig. 60 that the discharge breakdown occurred in the initial 0.5 μs, which was indicated with peak values of the population densities. Also, it appears that the peak values of population densities increase when the pressure increases, while the average values for N_2 ($C^3\Pi_u$) level that is $N_C \approx 7 \times 10^{12}$ cm^{-3}, vary little with the pressure change.

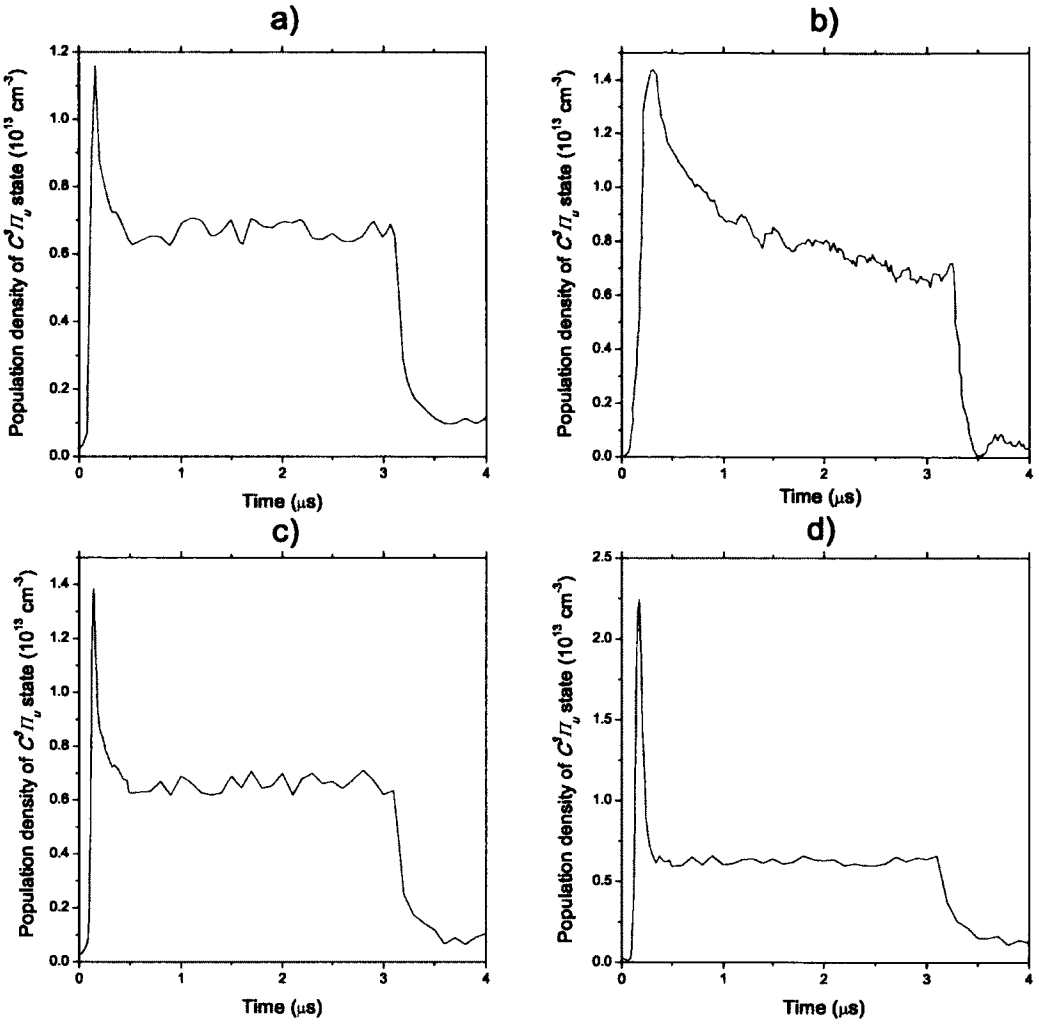

FIG. 60. Time-resolved population densities of the Second Positive System of Nitrogen (0-0) band at pressures: a) 10 Torr, b) 11.8 Torr, c) 13 Torr, and d) 20 Torr.

5.4.2 SUPERSONIC FLOWING ARGON DISCHARGE

In the case of supersonic flowing argon discharge, shown in Section 3.1, we were able to obtain not only time resolved spectra of excited Ar I states by employing time synchronization device, but also spatially resolved spectra of Ar I levels by applying plasma tomography approach. All measurements were taken in the plasma afterglow region, see Fig. 17, in order to characterize plasmoid-like formation. Similarly, as in

the above subsection, we used Eq. (81) to determine population densities of the Ar I upper energy levels.

a) Time-resolved data

Time resolved measurements were taken 5 cm downstream of the cavity in the experiment, see Fig. 17, which corresponds to the middle area of the plasmoid. The working pressure was $p = 2.3$ Torr. We obtained population distributions of three Ar I excited p states

- $2p_2$ or $4p'[1/2]_1$ $^3P_1$ $J = 1$ state from the spectral line intensity at 696.54 nm
- $2p_3$ or $4p'[3/2]_2$ $^1P_2$ $J = 2$ state from the spectral line intensity at 706.72 nm
- $2p_4$ or $4p'[3/2]_1$ $^1P_1$ $J = 1$ state from the spectral line intensity at 714.70 nm.

Spectral line intensities were measured with ICCD camera in 20 μs time intervals during the power signal.

Figure 61 shows the time dependent population distributions compared to the power sine signal. It can be deduced from the figure that during and immediately after the breakdown (the first two milliseconds), population distributions peak in their values. This is followed by the decrease in intensities during the plasma stabilization. Finally, when the discharge becomes quasi-stationary, the population density distributions show weak time dependence and can be approximated with their average values. The variation of the average values is probably due to additional changes of plasma conditions that are not included in the error estimation. Peak population densities are determined to be $N_{p2}^{peak} = 4.8 \pm 0.5 \times 10^5$ cm^{-3}, $N_{p3}^{peak} = 5.0 \pm 0.4 \times 10^5$ cm^{-3}, and $N_{p4}^{peak} = 7.8 \pm 0.6 \times 10^5$ cm^{-3}, while average values of population densities are estimated to $N_{p2}^{av} = 1.0 \times 10^5$ cm^{-3}, $N_{p3}^{av} = 1.1 \times 10^5$ cm^{-3}, and $N_{p4}^{av} = 1.6 \times 10^5$ cm^{-3} for Ar I excited states $2p_2$, $2p_3$, and $2p_4$, respectively.

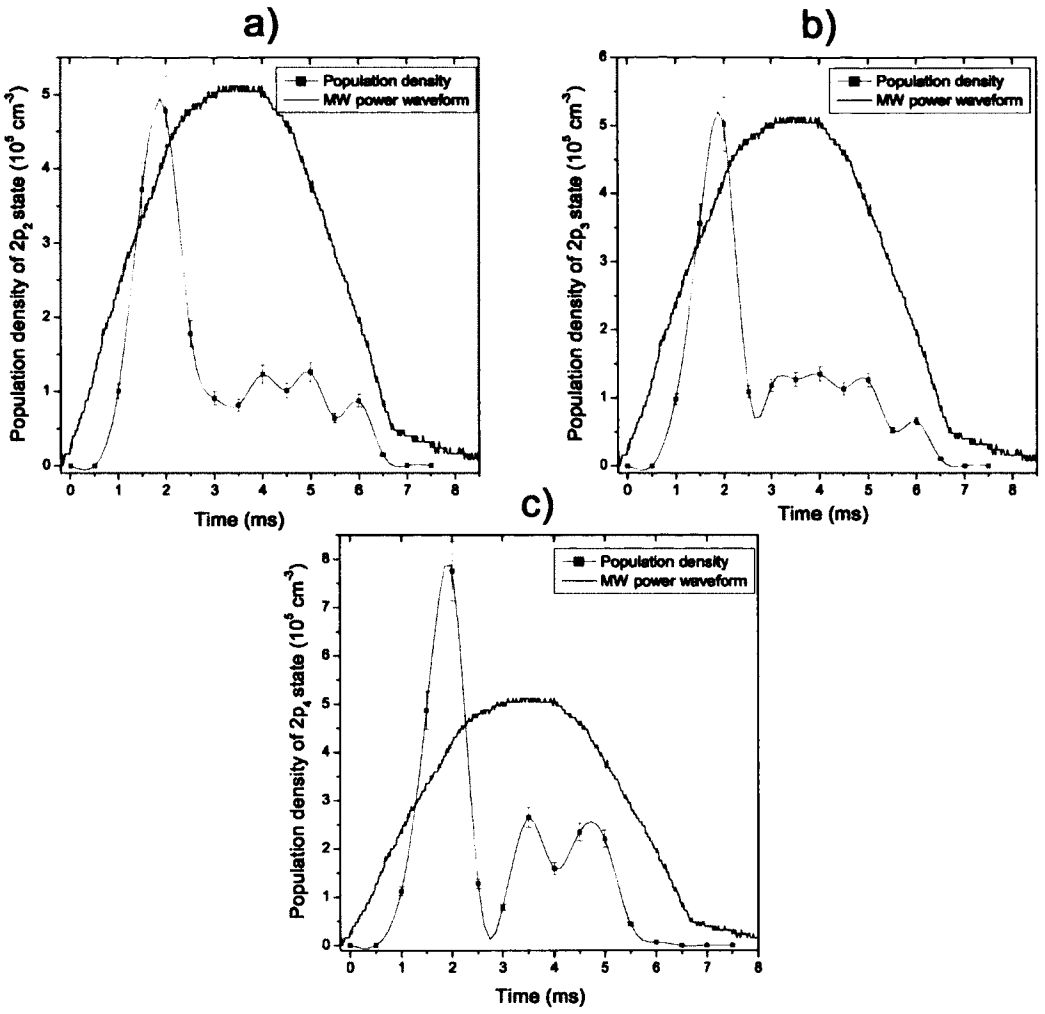

FIG. 61. Time dependence of the population densities inside the power sine signal at 2.3 Torr of the Ar I: a) $2p_2$ state, b) $2p_3$ state, and c) $2p_4$ state. The experimental results are connected with the smoothed fitted line.

b) Spatially resolved data - Plasma tomography

As a first step in obtaining time-averaged, spatially resolved population densities in argon, we have employed Abel inversion integration valid in the case of radially symmetric discharges. Three Ar I excited states

- $2p_3$ or $4p'[3/2]_2$ $^1P_2$ $J = 2$ state from the spectral line intensity at 706.72 nm

- $2p_4$ or $4p'[3/2]_1$ $^1P_1$ $J = 1$ state from the spectral line intensity at 714.70 nm
- $3s$ or $6s[3/2]_2$ $^3P_2$ $J = 2$ state from the spectral line intensity at 710.75 nm

were used for determining the spatial population density distributions.

Spectral line intensities were collected at 10 different locations downstream the microwave cavity (from 1.5 cm to 10.5 cm) and at 11 positions across the quartz tube (from the top to the bottom), see Fig. 17. Measurements were taken only at one angle due to the assumed radial symmetry. Therefore, there was no need to present data at each cross-sectional area of the quartz tube. Even though it was enough to take measurements only from the center to the one end of the quartz tube, we have scanned the whole area inside the tube to verify the assumption of plasma symmetry. If plasma is radially symmetric, the results from the upper side would be equivalent to the ones from the bottom. Measured spectral line intensities are shown in Fig. 62. It can be seen the presence of larger population densities at the lower side of the quartz tube which indicates the lack of radial symmetry. In other words, Abel inversion technique is not the best choice for reconstructing the internal plasma structure. However, it may happen that the upper and the lower sides are each radially symmetric independently. For that reason, as a first approximation, we estimated spatial distributions of Ar I $4p$ and $6s$ states using the Abel inverted integral given by Eq. (99) and results are presented in Fig 63.

It is evident from the Fig. 63 that the excited argon atoms are mostly located close to the inner surface of the quartz tube implying that the discharge is partially sustained with the surface wave, which is in a good agreement with our theoretical predictions stated in Section 3.1. However, spatial distributions of the Ar I population densities obtained using Abel inversion do not contain information whether discharge is symmetric or not. For that reason, we have applied the technique based on the measurements of spectral line intensities in two mutually perpendicular directions, described in Section 4.1.

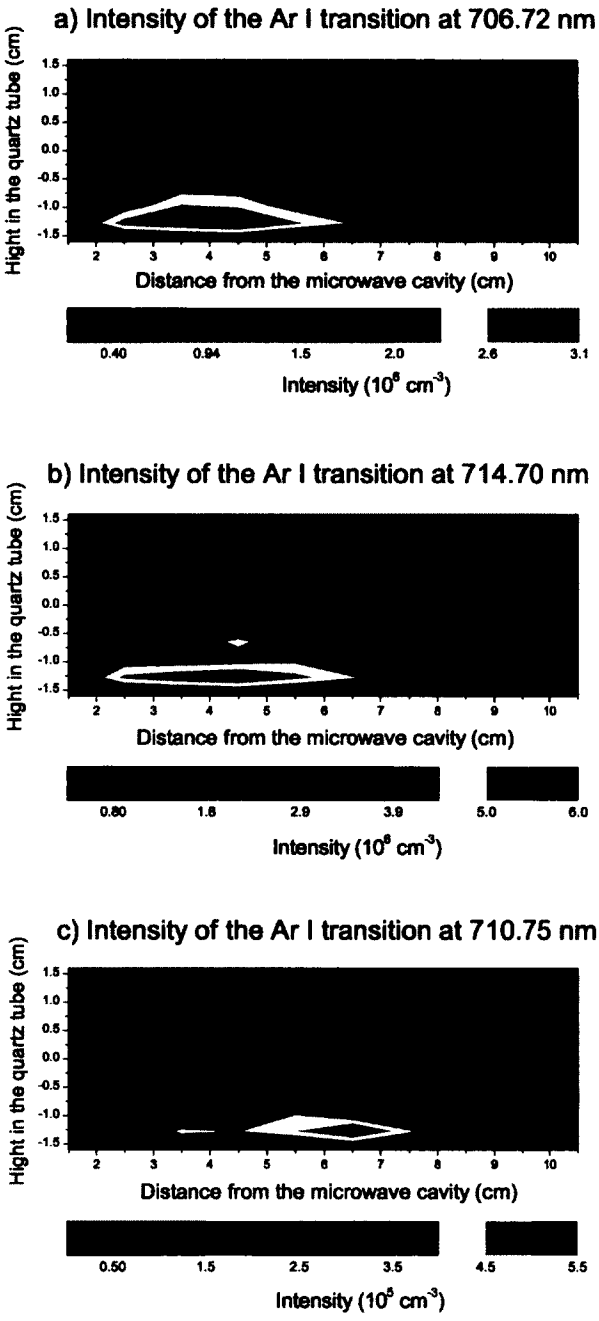

FIG. 62. Spatial distributions of the Ar I spectral line intensities of: a) $2p_3$ state b) $2p_4$ state, and c) $3s_3$ state. Measurements were taken along the quartz tube at pressure $p = 2.4$ Torr.

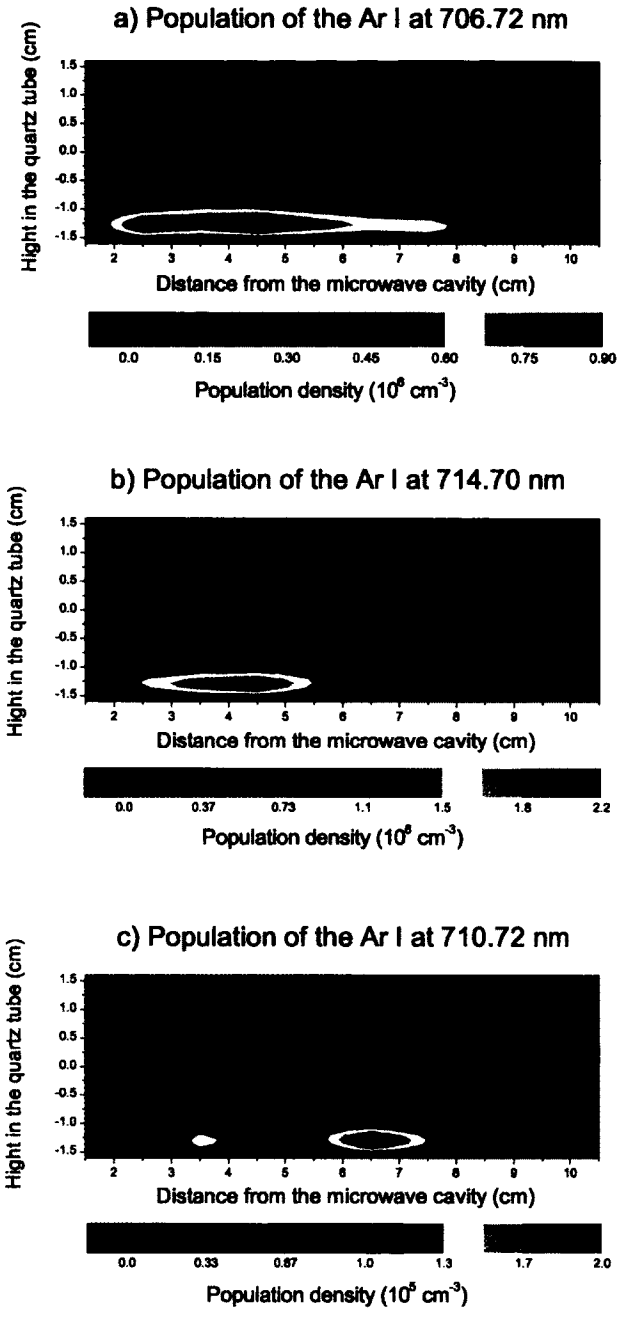

FIG. 63. Spatial distributions of the Ar I population densities obtained by applying Abel inversion integral: a) $2p_3$ state b) $2p_4$ state, and c) $3s_3$ state. Measurements were taken along the quartz tube at pressure $p = 2.4$ Torr, see Fig. 17.

Two excited Ar I states

- $2p_3$ or $4p'[3/2]_2$ $^1P_2$ $J = 2$ state from the spectral line intensity at 706.72 nm
- $2p_4$ or $4p'[3/2]_1$ $^1P_1$ $J = 1$ state from the spectral line intensity at 714.70 nm

were used for determining the spatial population density distributions. Data obtained with Abel inversion method served as measurements at one angle (i.e. $\theta = 0$). Additional measurements at $\theta = 90^0$ were performed at four different distances from the MW cavity(1.5 cm to 4.5 cm). These positions correspond to the beginning up to the central plasmoid region. The reconstructed populations of Ar I atoms are plotted in Figs. 64 and 65. The figures indicate turbulent behaviour of the discharge, which can be described only when time-resolved diagnostic methods are applied. It can be deduced from the figures that maximum population density of the Ar I $2p_3$ level $N_{p3} = 4.5 \times 10^5$ cm^{-3}, which is in good agreement with the population densities obtained using the time-resolved diagnostic method. Maximum population density of the Ar I $2p_4$ level is $N_{p4} = 1.3 \times 10^6$ cm^{-3}, which is a factor of two larger than time-resolved population densities. This is probably due to the lower accuracy of the method itself. However, the same conclusion remains that Ar atoms tend to populate outer parts of the quartz tube.

To summarize, Abel inversion, Eq. (99), and two path model, Eqs. (106) and (107), represent useful tools in understanding the internal plasma structure, especially when plasma is radially symmetric or at least close to the radial symmetry. But for complete analysis of plasma parameters it is necessary to conduct a full 2D plasma tomography based on the inverse Radon integral.

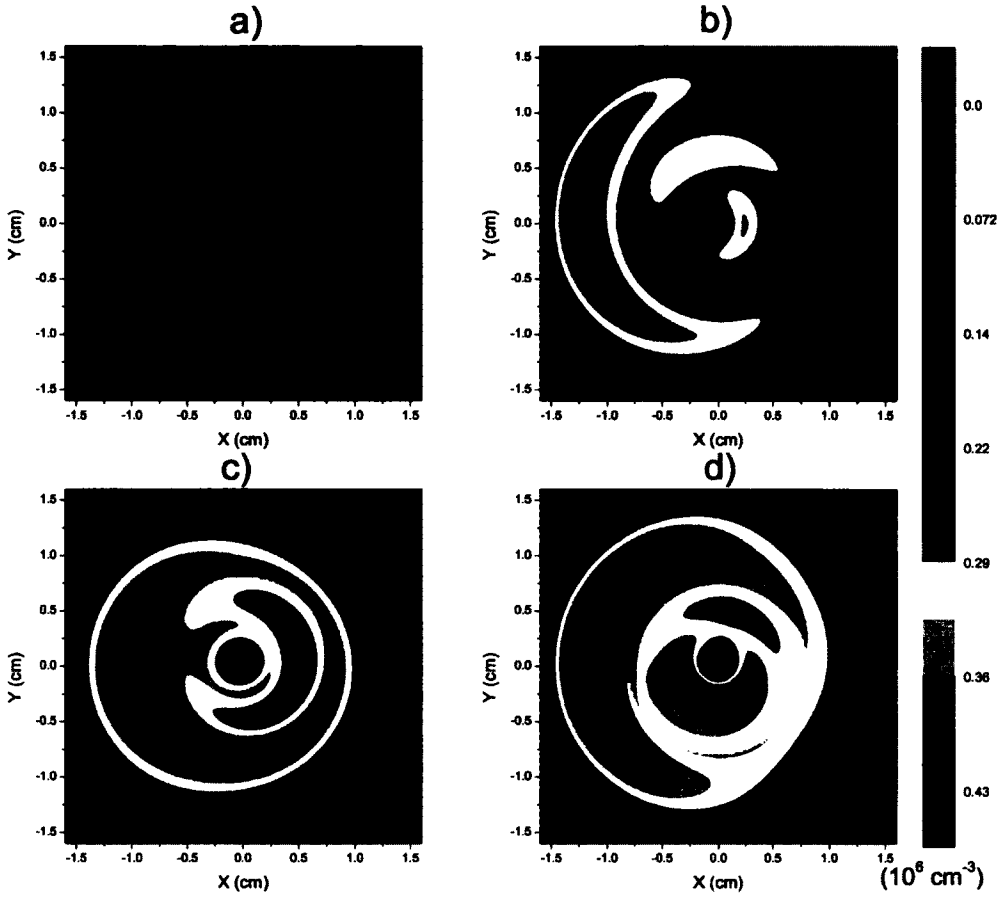

FIG. 64. Spatial distributions of the Ar I $2p_3$ population density at 706.72 nm measured at a) 1.5 cm, b) 2.5 cm, c) 3.5 cm, and d) 4.5 cm distance from the MW cavity, see Fig. 17. Measurements were obtained by applying two path method, based on measurements of spectral line intensities in two mutually perpendicular directions, at pressure $p = 2.4$ Torr.

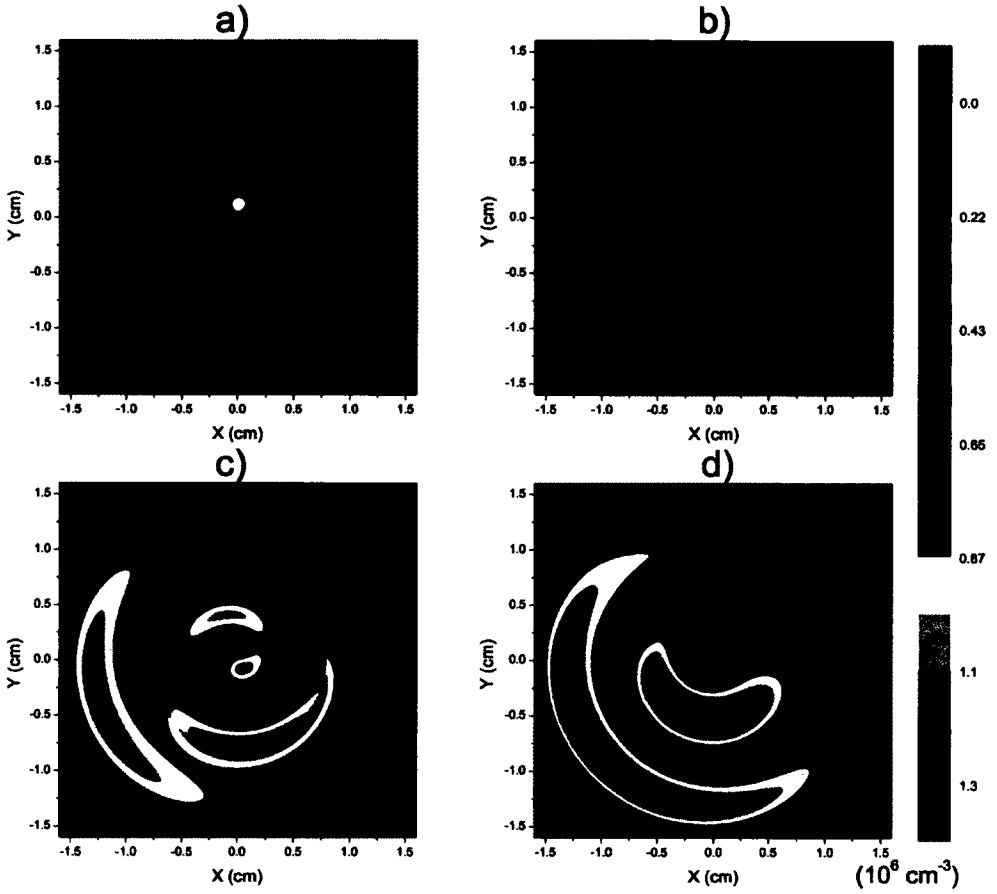

FIG. 65. Spatial distributions of the Ar I $2p_4$ population density at 714.70 nm measured at a) 1.5 cm, b) 2.5 cm, c) 3.5 cm, and d) 4.5 cm distance from the MW cavity, see Fig. 17. Measurements were obtained by applying two path method, based on measurements of spectral line intensities in two mutually perpendicular directions, at pressure $p = 2.4$ Torr.

We have employed a full 2D plasma tomography based on the filtered back projection method with Shepp-Logan filter on the same two Ar I excited states

- $2p_3$ or $4p'[3/2]_2$ $^1P_2$ $J = 2$ state from the spectral line intensity at 706.72 nm
- $2p_4$ or $4p'[3/2]_1$ $^1P_1$ $J = 1$ state from the spectral line intensity at 714.70 nm

to obtain spatial population density distributions.

The populations were evaluated at three different positions across the plasmoid relative to the cavity, see Fig. 17. The first measurements were taken 3 cm from the cavity corresponding to the beginning of the plasmoid. The next position measured was at 4.5 cm from the cavity that corresponds to the middle range of the plasmoid. Finally, we observed the end of the plasmoid by taking measurements 8 cm from the cavity.

Figure 66 shows how the spatial distribution of Ar I excited states at 706.72 nm is changing along the plasmoid. It could be seen that the argon atoms are mainly populated close to the inner surface of the quartz tube. At distances 3 cm and 8 cm from the cavity (two ends of the plasmoid) argon atoms are concentrated close to one side of the quartz tube, while in the middle (4.5 cm from the cavity) we observe almost symmetrical population distributions. The maximal value population density that is $N_{p3} = 1.3 \times 10^5$ cm^{-3}, is reached at the surface of the tube in the middle of the plasmoid.

Similar results are observed for population distributions of Ar I excited states at 714.70 nm, see Fig 67. Argon atoms are distributed mostly at the surface of the tube with the maximal population density $N_{p4} = 1.6 \times 10^5$ cm^{-3}. It should be noted, that population densities obtained using this method are in good agreement with the values of the population densities obtained using the time-resolved diagnostic method implying that 2D inverse Radon integration technique Eq. (135) provides not only qualitative but also a quantitative description of the plasmoid object.

The lack of cylindrical symmetry in the population distributions emerges from our ability to measure at a limited range of angles (48^0 to 168^0), as shown in Section 4.1. The missing parts correspond to the area that was not covered in the experiment. It is, however, obvious from the Figs. 66 and 67 that the excited species are dominantly

populated at the rim of the plasmoid. This observation indicates that the plasmoid is sustained by a surface wave.

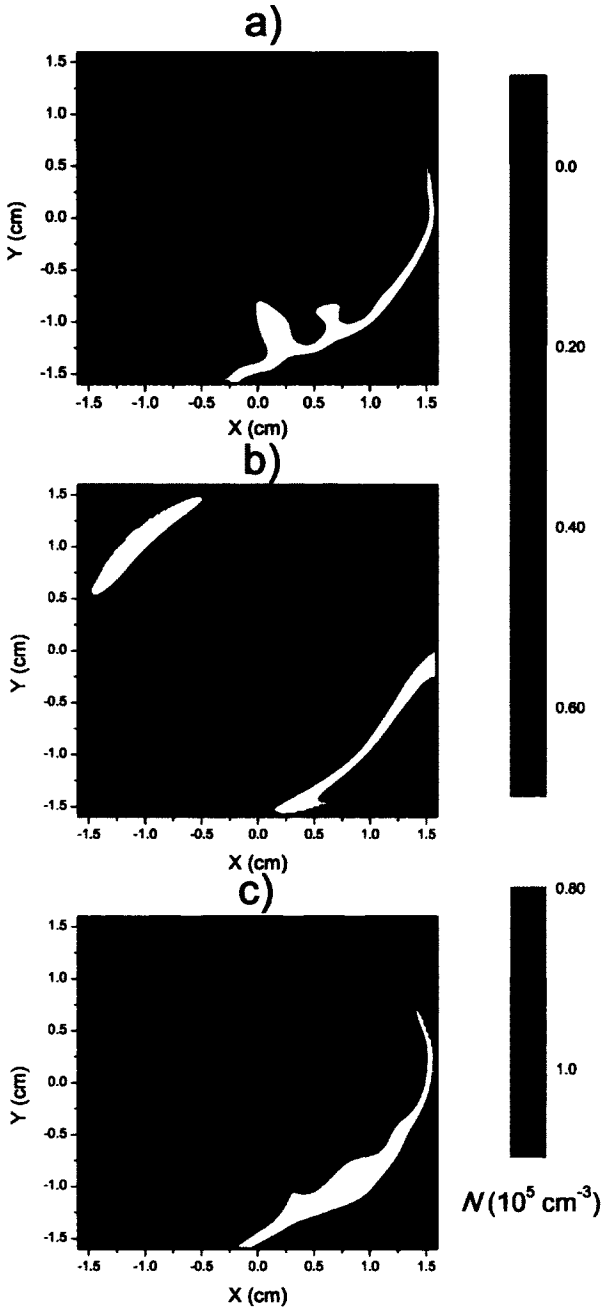

FIG. 66. Spatial distributions of the Ar I $2p_3$ population density at 706.72 nm measured at different distances from the MW cavity: a) 3 cm, b) 4.5, and c) 8 cm. Measurements were obtained by applying filtered back projection method with Shepp-Logan filter (Section 4.1) at pressure $p = 2.4$ Torr.

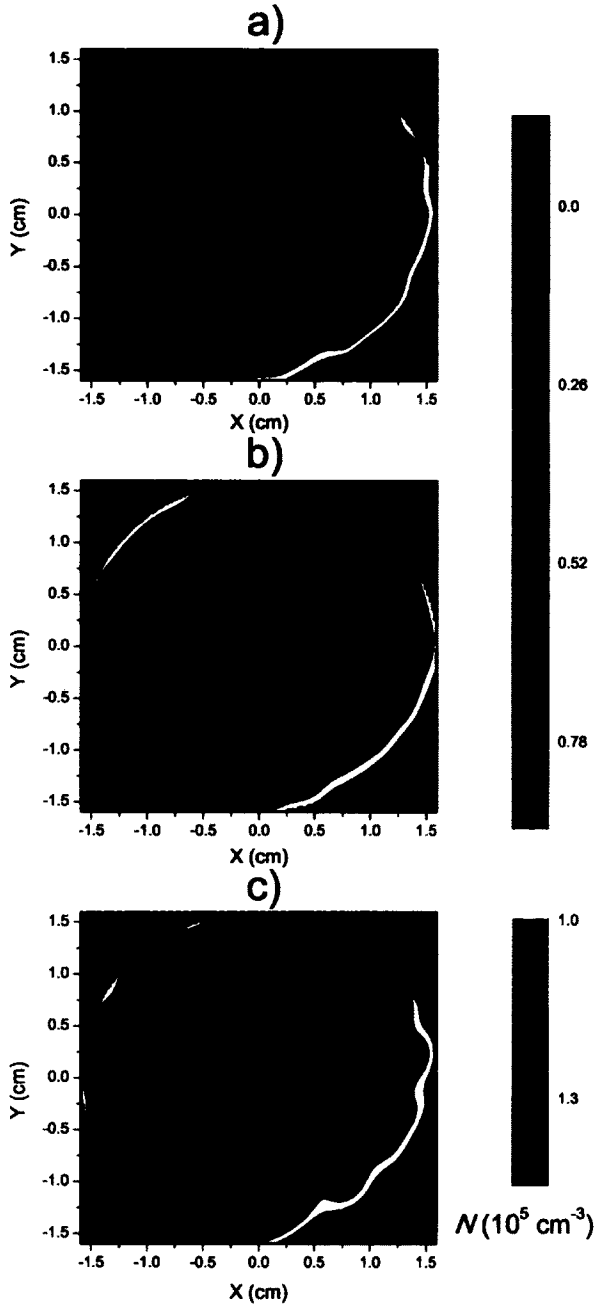

FIG. 67. Spatial distributions of the Ar I $2p_3$ population density at 714.70 nm measured at different distances from the MW cavity: a) 3 cm, b) 4.5, and c) 8 cm. Measurements were obtained by applying filtered back projection method with Shepp-Logan filter (Section 4.1) at pressure $p = 2.4$ Torr.

5.5 ELECTRON EXCITATION TEMPERATURE

The electron excitation temperature is an important parameter for the characterization of plasma since it describes the energy distribution of the excited atomic states. We have obtained spatial distributions of the electron excitation temperatures in the supersonic flowing argon discharge, described in Section 3.1, by employing the Boltzmann plot method. This method assumes that the spectral irradiances (I_{ki}) of different Ar excited state spectral lines having the same lower energy and different threshold excitation energies (E_k) follow a Botzmann distribution [70]

$$I_{ki} = \frac{g_k A_{ki}}{\lambda_{ki}} e^{-E_k/k_B T_{exc}} \tag{196}$$

where g_k is the statistical weight of the upper level k, A_{ki} is the transition probability, λ_{ki} is the wavelength, and T_{exc} is the excitation temperature. The electron excitation temperature relates to the slope of the $log(I_{ki}\lambda_{ki}/g_k A_{ki})$ versus E_k plot. We were looking into transitions to the Ar I $3s^2 3p^5(^2P^0_{3/2})4s, J = 2$ lower level. The upper energy levels, wavelengths and corresponding constants used for determining the excitation temperature are presented in the Table 7.

TABLE 7. Ar I spectral lines used for T_{exc} determination.

Upper level	J	λ (nm)	g_k	A_{ki} (10^6 s^{-1})	E_k (eV)
$5p[3/2]_2\ ^1P_2$	2	415.9	5	1.400	14.53
$5p[5/2]_3\ ^1P_3$	3	420.1	7	0.967	14.50
$4p'[3/2]_2\ ^1P_2$	2	706.8	5	3.860	13.30
$4p'[3/2]_1\ ^1P_1$	1	714.7	3	0.625	13.28
$4p'[5/2]_3\ ^1P_3$	3	811.5	7	33.10	13.07

Equation (196) incorporates a premise that discharge satisfies the local thermodynamic equilibrium (LTE) or, at least, is close to it. The validity criteria for LTE

was established by Griem [18]

$$N_e \geq 7 \times 10^{18} \frac{z^7}{n^{17/2}} (\frac{kT_e}{z^2 E_H}) cm^{-3} \tag{197}$$

where N_e is electron density, z=1 for neutral emitters, n is a principal quantum number of the upper level (n=4 for argon), E_H is ionization energy of hydrogen, and T_e is electron temperature.

Based on the previous work on the same experiment [68] electron temperature was determined to be $T_e \approx 6000$ K which corresponds to $kT_e \approx 0.5$ eV. Employing Eq. (197) leads to the conclusion that an electron density of $N_e \geq 10^{13}$ cm^{-3} is required to fulfil LTE. According to Ref. [68] this condition is satisfied in the supersonic flowing argon discharge which justifies the Boltzmann plot approach in calculating T_{exc}.

We obtained the distributions of excitation temperatures at two positions along the plasmoid, 3 cm and 8 cm from the cavity corresponding to the beginning and ending of the plasmoid, respectively, see Fig. 17. Results are presented in Fig. 68. The maximal excitation temperature obtained was T_{exc} = 2820 K at 3 cm downstream the cavity and T_{exc} = 3030 K at 8 cm from downstream cavity. This is in good agreement with previously published data [68].

Note that the excitation temperature maximum tends to be in contrast to the population distribution. Furthermore, the temperature distributions exhibit rotational behavior. Both effects reflect the influence of the supersonic flow. Relative populations of the two excited levels tend to follow the dynamics and structure of the flow, which in turn is affected by the surface wave discharge. The phenomenon is nonlinear and more detailed spectroscopy is needed to clarify fully the flow dynamics.

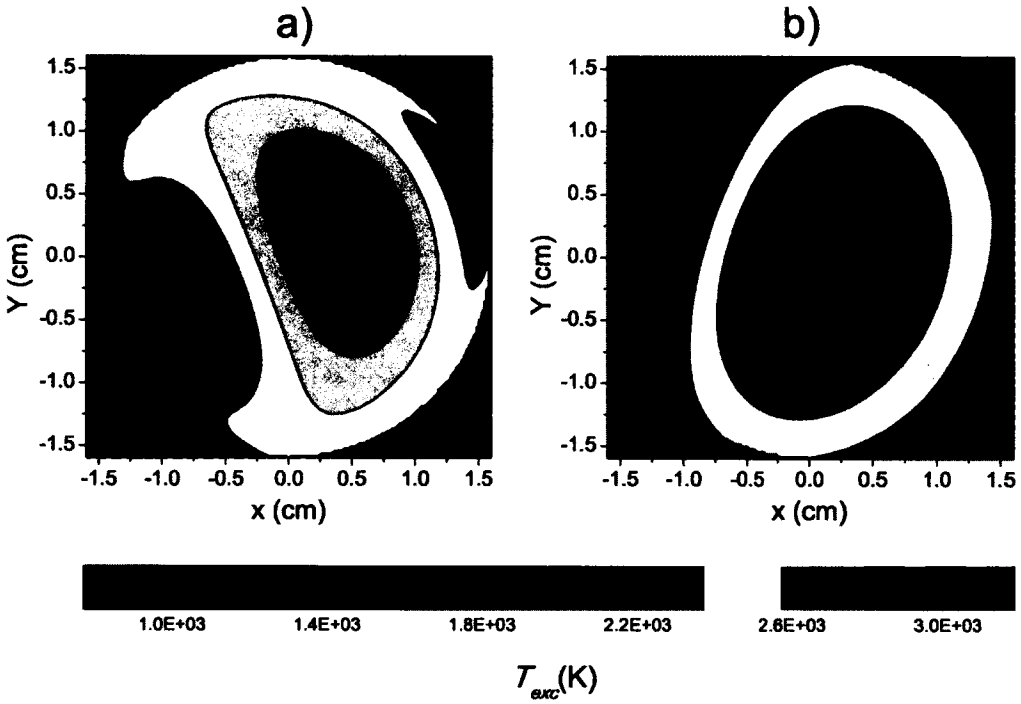

FIG. 68. Spatial distributions of argon excitation temperatures obtained at distances a) 3 cm from the cavity and b) 8 cm from the cavity.

5.6 ELECTRON TEMPERATURE

One of the most informative parameters in plasma physics is electron temperature because electrons are involved in almost all collision processes in the plasma (excitation, ionization, dissociation) defining in that way physical and chemical plasma properties. Time-resolved electron temperature was obtained in pulse repetitive MW discharge in air that is described in Section 3.2, from the values of the time dependent reduced electric field by applying the correlation graph given in Fig. 10 which is given in Chapter 2. Space-average peak electric field was determined from the average peak power density, P_{ave} by employing Eq. (88).

At the chamber pressure p=11.8 Torr and room temperature the averaged peak reduced field was therefore

$$\left(\frac{E}{N_n}\right)_{ave} = 126\,Td. \tag{198}$$

This means that the peak power of 210 kW at the waveform plateau corresponds to the average reduced electric field of 126 Td.

The actual time-dependent reduced electric field at the plasma can be calculated from the average power per unit area transported by microwave intensity,

$$I \sim \left(\frac{E}{N_n}\right)^2, \tag{199}$$

taking into account

$$I = I_F - I_R, \tag{200}$$

where I_F is the intensity of the forward (travelling) wave and I_R is the intensity of the reflected wave. Thus,

$$\left(\frac{E}{N_n}\right)^2(t) = \left(\frac{E}{N_n}\right)_F^2(t) - \left(\frac{E}{N_n}\right)_R^2(t), \tag{201}$$

where $\left(\frac{E}{N_n}\right)_F(t)$ is reduced electric field associated with the forward wave and $\left(\frac{E}{N_n}\right)_R(t)$ is the reduced electric field associated with reflected wave. Reduced electric field is related to the total power as

$$\left(\frac{E}{N_n}\right)(t) \sim \sqrt{P(t)}. \tag{202}$$

If we introduce the reflection coefficient

$$\Gamma(t) = \sqrt{\frac{P_R(t)}{P_F(t)}} = \frac{\left(\frac{E}{N_n}\right)_R(t)}{\left(\frac{E}{N_n}\right)_F(t)}, \tag{203}$$

where $P_F(t)$ and $P_R(t)$ are the forward and reflected power respectively, we derive

$$\left(\frac{E}{N_n}\right)(t) = \left(\frac{E}{N_n}\right)_F \sqrt{1 - \Gamma^2(t)}. \tag{204}$$

Forward and reflected power waveforms were recorded at the front and rear end of a bidirectional coupler with the attenuations of 23 and 13 dB, respectively (shown in Fig. 28). Further, in the case of reflected power waveform, pyramidal horn acted as the receiving antenna at the aperture, whereby the reflected beam passed through a ceramic power attenuation factor of $(\varepsilon_z)^{-1/2} \approx \frac{1}{3}$ that has to be taken into account [41].

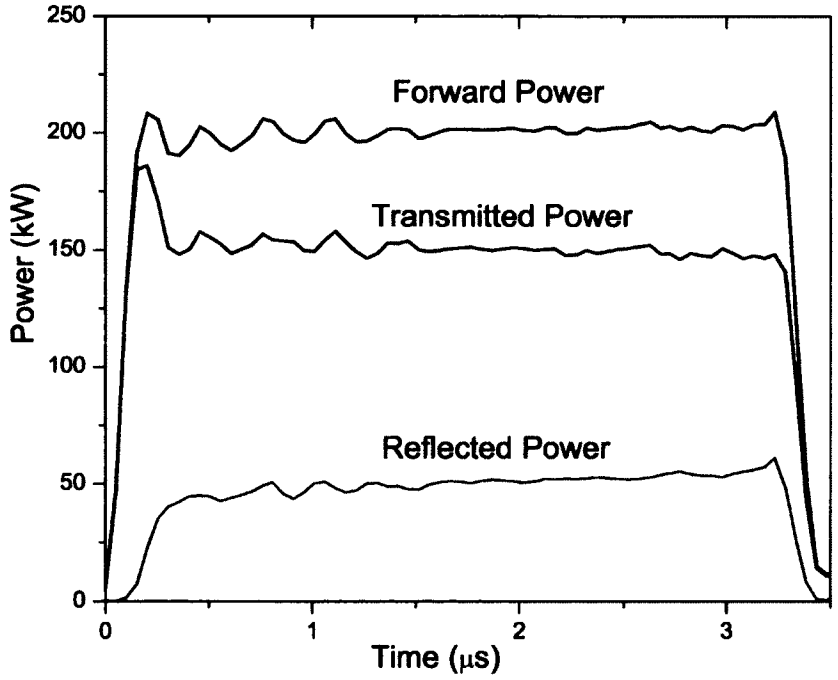

FIG. 69. Forward, reflected and transmitted into plasma power waveforms.

The actual power waveforms are evaluated from the detector voltage waveforms according to

$$P_F(t) = P_{peak} \times \frac{V_{FP}(t)}{V_{FPmax}} \tag{205}$$

$$P_R(t) = P_{peak} \times \frac{V_{RP}(t)}{10 \times V_{RPmax}} (\epsilon_z)^{-1/2} \tag{206}$$

$$P_T(t) = P_F(t) - P_R(t), \tag{207}$$

where $P_F(t)$, $P_R(t)$, and $P_T(t)$ are the forward, reflected and transmitted power, respectively, $V_{FP}(t)$ and $V_{RP}(t)$ are measured forward and reflected voltage waveforms respectively, and V_{FPmax} and V_{RPmax} are their maximum values.

Figure 69 shows the waveforms for the forward, reflected and transmitted power evaluated from the detector signals. From the figure it can be seen that the reflected power signal was measured at $\leq$ 20% of forward power signal. Still, the reflected power waveform quantifies the contribution of the reflected wave in the total field amplitude at the aperture and in the sustaining the standing wave discharge between the dielectric cover of the aperture and the plasma itself, in analogy to the cylindrical surface wave discharges.

Knowing the time-resolved waveforms of the forward and reflected power allowed us to apply Eq. (204) and determine the time variation of the reduced electric field. Figure 70 shows pressure dependence of the reduced electric field E/N_n. It appears that E/N_n is almost constant for most of the pulse duration except for the first 0.5 μs during the discharge build-up when it peaks in its value. Also, as it can be seen from the figure, at lowest pressure at 10 Torr, E/N_n is the largest with the peak values $(E/N_n)_{peak} \approx 160$ Td and average values $(E/N_n)_{ave} \approx 145$ Td. At 11.8 and 13 Torr pressure, E/N_n is at its minimum with $(E/N_n)_{peak} \approx 115$ Td and $(E/N_n)_{ave} \approx 105$ Td, and at 13 Torr E/N_n increases and has the peak value $(E/N_n)_{peak} \approx 130$ Td and average value $(E/N_n)_{ave} \approx 120$ Td.

Figure 71 shows time-resolved electron temperatures obtained from the reduced electric as a function of pressure. It is obvious that electron temperature depends on pressure in similar way as reduced electric field. This is expected since electron temperature is almost linearly proportional to E/N_N, see Fig. 10. Peak values of electron temperature vary from 2-3 eV, while average values range from 1.7-2.7 eV.

Note that for simplicity, the effect of the relaxation of electron energy distribution function (EEDF) was neglected. In the initial 0.5 microseconds the EEDF is dominated by inelastic collisions, mostly by ionization, and differs substantially from

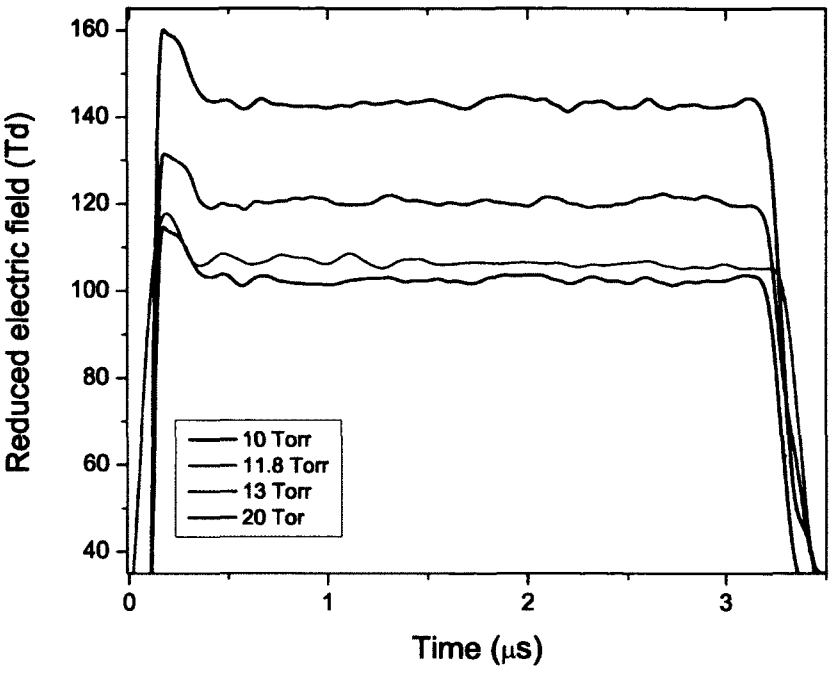

FIG. 70. Time-resolved reduced electric field evaluated from the power waveform at pressures of: a) 10 Torr, b) 11.8 Torr, c) 13 Torr, and d) 20 Torr.

the EEDF applied in the rest of the pulse, which is based on the full set of electron-molecule collisions. Small values of N_e in the time interval of discharge build-up will make the effect of time dependent EEDF small. Still, evaluation of EEDF at the inception of the microwave discharge is certainly an important task for future work.

Similarly, as in the case of rotational temperature evaluation we were not able to obtain electron temperatures in argon discharge described in Section 3.1. In the first approximation we will employ previous work on the same experiment [68] to estimate electron temperatures. According to [68] at pressure $p = 2.3$ Torr, electron temperature was $T_e = 6000$ K which corresponds to $kT_e = 0.5$ eV.

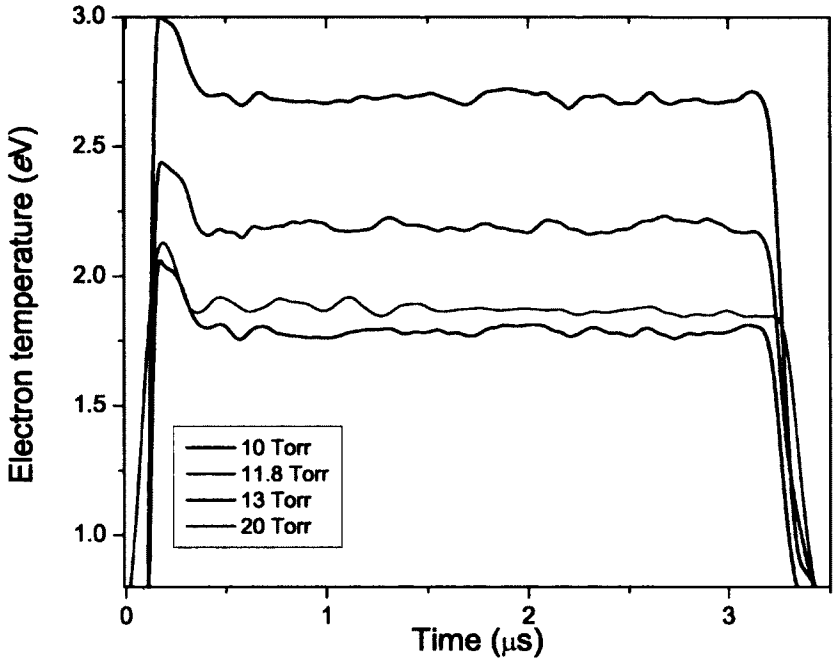

FIG. 71. Time-resolved electron temperatures evaluated from power waveform at pressures of: a) 10 Torr, b) 11.8 Torr, c) 13 Torr, and d) 20 Torr.

5.7 RATE COEFFICIENTS

We proceed by calculating rate coefficients required for kinetic model in pulse repetitive air discharge described in Section 3.2. As it has already been pointed out, the rate coefficient for the electron impact excitation, $k_e^{X(0)}$, depends on the reduced electric field (given in Fig. 14a) and can be obtained from reduced electric field (or electron temperature) values by employing Eq. (51).

In the Fig. 72 time-resolved $k_e^{X(0)}$ is presented at four different pressures. It could be deduced from the figure that $k_e^{X(0)}$ behaves similarly as E/N_n or T_e in terms of both pressure and time dependence. Peak values of the rate coefficient are in the (4-15) $\times 10^{-11}$ cm^3/s range and average values vary from 2 $\times 10^{-11}$ to 10 $\times 10^{-11}$ cm^3/s.

Figure 70 showed that the reduced electric field is almost constant for most of the pulse duration allowing us to apply the rate coefficients for vibrational excitation by electron impact, $k_e^{C(0)}$ and $k_e^{C(v)}$, with a constant value. In the first approximation, all rate coefficients for vibrational excitation by electron impact were determined by

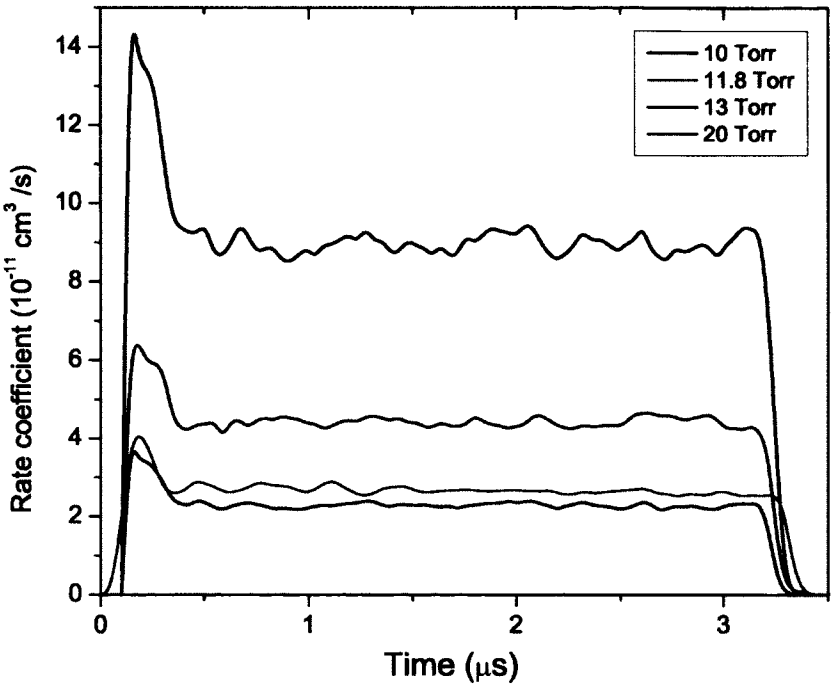

FIG. 72. Time-resolved rate coefficient for electron impact excitation of the (0-0) band in the Second Positive System of Nitrogen at pressures of: a) 10 Torr, b) 11.8 Torr, c) 13 Torr, and d) 20 Torr.

employing Eq. (51), assuming that for this particular case the EEDF was constant during the pulse and dependent solely on the self-consistent electrical field.

There are still no measured nor calculated total cross-sections for vibrational excitation of the $N_2(C^3\Pi_u)$ state available. In order to estimate these rate coefficients, we have taken the advantage of the fact that the vibrational excitation rates of the nitrogen ground state have been reported in the literature [20]. Therefore, we estimate $k_e^{C(0)}$ and $k_e^{C(v)}$ by scaling the values of rate coefficients for the vibrational levels in $N_2(X_1\Sigma_g^+)$ state. Results for the rate coefficients in the ground state are given in the Table 8. The same concern arises in evaluation of rate coefficients for V-V processes, $k_c^{C(0),C(v)}$ and $k_c^{C(1),C(v-1)}$. By applying the results of Capitelli and Dilonardo [71], we have estimated these coefficients to be about 10^{-18} cm^3/s, which implies they could be neglected in the first approximation.

The next step was to evaluate the rate constant for collisional deactivation.

TABLE 8. Rate coefficients for the electron-impact vibrational excitation of the ground-state nitrogen.

v	1	2	3	4
Rate coefficients (10^{-10} $\frac{cm^3}{s}$)	41.6	23.8	16.2	9.37

Quenching rate constant, $k_c^{X(0),C(0)}$, is a function of density and vibrational quantum number [31], as shown in Eq. (66). Rate coefficients for the collisional quenching at different pressures are presented in Table 9 where we used the radiative life time of $N_2(C^3\Pi_u)$ state $\tau_{CB} = 45$ ns.

TABLE 9. Rate coefficients for the collisional quenching from the Nitrogen Second Positive System at different pressures in air discharge.

Pressure (Torr)	Rate coefficients (10^{-11} $\frac{cm^3}{s}$)
10.0	2.9
11.8	2.7
13.0	2.7
20.0	2.3

We should mention that in discharges containing air, the nitric oxide, NO, which is highly reactive, could be produced in observable quantities. In this work we evaluated the presence of nitric oxide by comparing the radiation from nitrogen and nitric oxide bands. We found that NOγ bands could be barely observed. Thus, we conclude that NO presence is negligible.

Separately, for the purpose of the study of supersonic flowing argon discharge described in Section 3.1 we have calculated rate coefficients for electron impact excitation from its dependence on the reduced electric field or electron temperature values by employing Eq. (51) (given in Fig. 13). By assuming electron temperature $T_e = 0.5$ eV, we have evaluated excitation rate coefficients from Ar I ground state to be $k_e^{g,p2} = 0.5 \times 10^{-11}$ cm^3/s for Ar I $2p_2$ excited state, $k_e^{g,p3} = 0.24 \times 10^{-11}$ cm^3/s for Ar I $2p_3$ excited state, and $k_e^{g,p4} = 0.13 \times 10^{-11}$ cm^3/s for Ar I $2p_4$ excited state. Excitation rate coefficients from Ar I metastable $1s5$ state are $k_e^{g,p2} = 1.8 \times 10^{-11}$

cm^3/s for Ar I $2p_2$ excited state, $k_e^{g,p3} = 10.0 \times 10^{-11}$ cm^3/s for Ar I $2p_3$ excited state, and $k_e^{g,p4} = 1.4 \times 10^{-11}$ cm^3/s for Ar I $2p_4$ excited state.

We have also calculated the quenching rate coefficients in supersonic flowing argon discharge by employing the results of Zhu and Pu [30], see Table 1. They are equal to $k_c^{g,p2} = 2.3 \times 10^{-11}$ cm^3/s for Ar I $2p_2$ excited state and $k_c^{g,p3} = k_c^{g,p4} = 6.8 \times 10^{-11}$ cm^3/s for Ar I $2p_3$ and $2p_4$ excited states respectively, at pressures of 2.3 Torr. In addition, radiative life times for Ar I $2p \rightarrow 1s$ transitions are given in Table 10.

TABLE 10. Radiative life times for $2p \rightarrow 1s$ transitions in argon discharge.

	$1s_2$	$1s_3$	$1s_4$	$1s_5$
$2p_2$	21.7 ns	28.0 ns	182 ns	52.0 ns
$2p_3$	7.80 ns		23.5 ns	52.6 ns
$2p_4$	24.0 ns	17.9 ns	1.52×10^4 ns	532 ns

5.8 ELECTRON DENSITY

Electron density is one of the most fundamental plasma parameters since it affects the energy balance and heat transfer, kinetics, and global properties of the plasma, such as wave transmission reflectivity, absorption, and scattering [8]. It is, therefore, of vital importance to determine the time-resolved electron density distributions in the case of non-equilibrium, non-stationary, fast moving, and chemically reactive gas discharges. Time-resolved electron density was obtained in pulse repetitive air discharge, described in Section 3.2, by applying kinetic model based on the analysis of molecular bands of nitrogen $C^3\Pi_u \rightarrow B^3\Pi_g$ second positive system.

Both electronic and vibrational states were included in the study. Vibrational population of the $N_2(C^3\Pi_u)$ state depends on two main terms, vibrational excitation by electron impact within the $N_2(C^3\Pi_u)$ state, and vibration-vibration collisions within the same state, described in Subsection 4.3.2. We have estimated the contributions from both e-V and V-V collisional processes by using rate coefficients for the nitrogen ground state in the absence of the proper coefficient rates for the $N_2(C^3\Pi_u)$ state. The terms due to the e-V processes are nine orders of magnitude smaller than any other term in the Eq. (160) and the terms due to the V-V processes contribute even less to Eq. (160). Rates for the vibrational excitation of the $N_2(C^3\Pi_u)$ state are even smaller than the ones for the ground state which justifies neglecting them. Thus the last four terms in Eq. (160) are neglected in the numerical solution, as well as for the analytical approximation.

Electron density was first estimated by employing Eq. (165) for the steady state analytic method. Results for the steady state case are given in Table 11.

TABLE 11. Time-averaged electron density obtained in the Nitrogen Second Positive System at different pressures in air discharge.

Pressure (Torr)	Electron density (10^{13} cm^{-3})
10.0	6.5
11.8	5.0
13.0	4.6
20.0	1.3

We have assumed that the relative errors in pressure and k_e measurements were no more than 5%. The electron density waveform was then obtained numerically in two steps. First, we calculated the first derivative of the measured $N_2(C^3\Pi_u)$ state and then we used this value to determine electron density waveform from Eq. (160). The time-resolved electron density distribution for the pressure at $p = 11.8$ Torr is presented in Fig. 73. The average value of the electron density from the numerical method was calculated to be $(5.0\pm0.5)\times10^{13}$ cm^{-3} over the interval 0.1-4.0 μs, and is indicated in Fig. 73 with a dashed horizontal line.

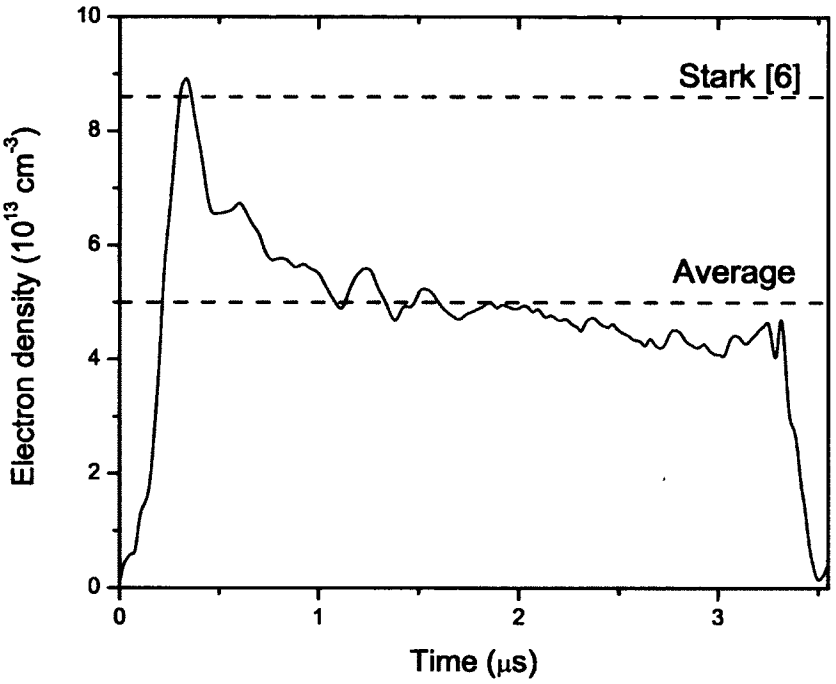

FIG. 73. Electron density waveform evaluated numerically using band intensity waveform and Eq. (160).

As seen in Fig. 73, these values are lower than the results obtained using Stark broadening data from Ref. [41]. There are two reasons for such a discrepancy. First, for the plasma conditions at hand, the deconvolution of the Stark width from the measured Voigt profile was limited by the instrumental resolution of the spectrometer.

Second, the intensity-to-noise ratio of the H_β line was rather low. Those uncertainties led the authors [41] to estimate the spread of the electron density value obtained from Stark broadening of H_β line of $(8\pm3)\times10^{13}$ cm^{-3} which is in fair agreement with electron densities obtained in this work.

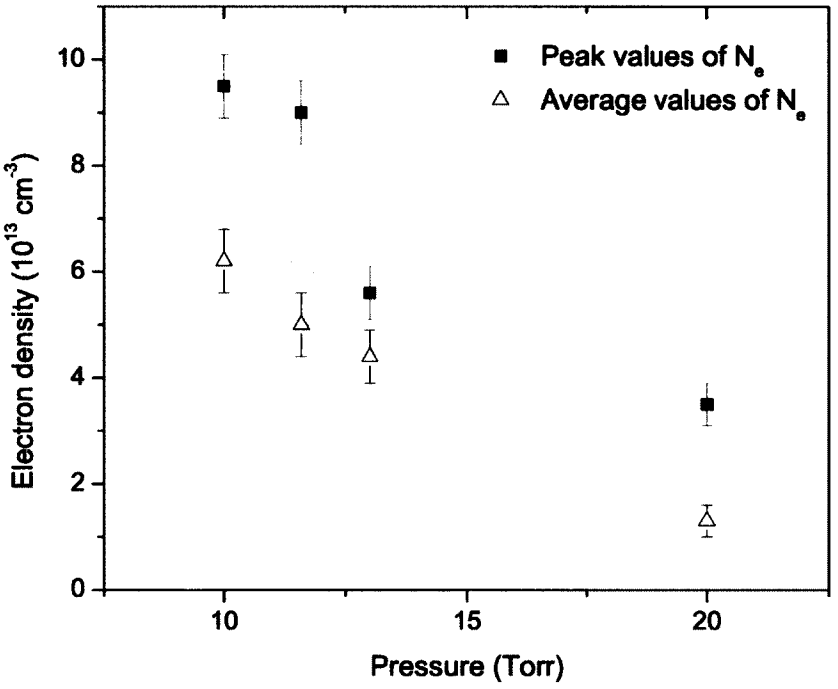

FIG. 74. Pressure dependence of average and peak values of the electron density.

Using the described method, we have performed measurements of electron density at three additional pressure points: at 10, 13 and 20 Torr. The average and peak values of the electron density at four different pressures are given in Fig. 74. It shows that the electron density decreased by a factor of 6, approximately. This sharp drop is explained by the drop of the reduced electric field because the number density of ground state increases by more than a factor of two and the electric field remains the same. Additional contribution to the electron density drop comes from the nonlinear variation of the rate coefficients with the reduced electric field.

5.9 POPULATION DENSITIES OF ARGON METASTABLE AND RESONANT LEVELS

Here we provide information about time-resolved population densities of Ar I metastable and resonant levels, in addition to time-resolved population densities of Ar I p levels described in Section 5.4. Metastable atoms play an important role in characterization of gas discharges. Due to their high energy and long life time they are considered an important energy reservoir, which could be transmitted to the rest of plasma particles by collisional processes.

We have obtained population densities of two Ar I levels:

- Metastable $1s_5$ or $4s[3/2]_2\ ^3P_2$ $J = 2$ state from the spectral line intensity at 706.72 nm
- Resonant $1s_4$ or $4s[3/2]_1\ ^3P_1$ $J = 1$ state from the spectral line intensity at 727.29 nm.

Argon metastable/resonant level population densities were obtained by applying Ar kinetic model, described in Subsection 4.3.1, in the following way. First, we have calculated the difference in intensities of measured Ar I $2p$ states with and without presence of dye laser light beam. Further, we have determined the first derivative of the calculated difference. These results have been used to evaluate time-resolved population densities of metastable/resonant states by employing Eq. (153) stated in Subsection 4.3.1.

Time-resolved population densities of Ar I metastable $1s_5$ level were determined from the kinetic equation of the Ar I $2p_3$ level, derived from Eq. (153)

$$\frac{B_{12}I_\omega}{c}N_{s5} = \frac{d}{dt}(N'_{p3} - N_{p3}) + \Big(\frac{1}{\tau_{s2}} + \frac{1}{\tau_{s4}} + \frac{1}{\tau_{s5}} + k_c^{g,p3}N_n\Big)(N'_{p3} - N_{p3}), \quad (208)$$

where τ_{s2}, τ_{s4}, and τ_{s5} are radiative life times of the Ar I $2p_3$ level to $1s_2$, $1s_4$, and $1s_5$ levels, respectively, shown in Table 10, and B_{12} is the Einstein coefficient for laser absorption given with the Eq. (141). For the statistical weight of the $1s_5$ metastable level of $g_{s5} = 5$ and the transition wavelength $\lambda = 706$ nm, Einstein absorption coefficient is equal to $B_{12} = 8.5 \times 10^{19}$ J^{-1}m^{3}s^{-2}.

Similarly, we have obtained time-resolved population densities of Ar I resonant $1s_4$ level by employing the kinetic equation of the Ar I $2p_2$ level

$$\frac{B_{12}I_\omega}{c}N_{s4} = \frac{d}{dt}(N'_{p2} - N_{p2}) + \Big(\frac{1}{\tau_{s2}} + \frac{1}{\tau_{s3}} + \frac{1}{\tau_{s4}} + \frac{1}{\tau_{s5}} + k_c^{g,p2}N_n\Big)(N'_{p2} - N_{p2}). \quad (209)$$

Einstein B_{12} coefficient for laser absorption was equal to $B_{12} = 4.5 \times 10^{19}$ $J^{-1}m^3s^{-2}$ where statistical weight of the $1s_4$ metastable level was $g_{s4} = 3$ and the transition wavelength was $\lambda = 727$ nm.

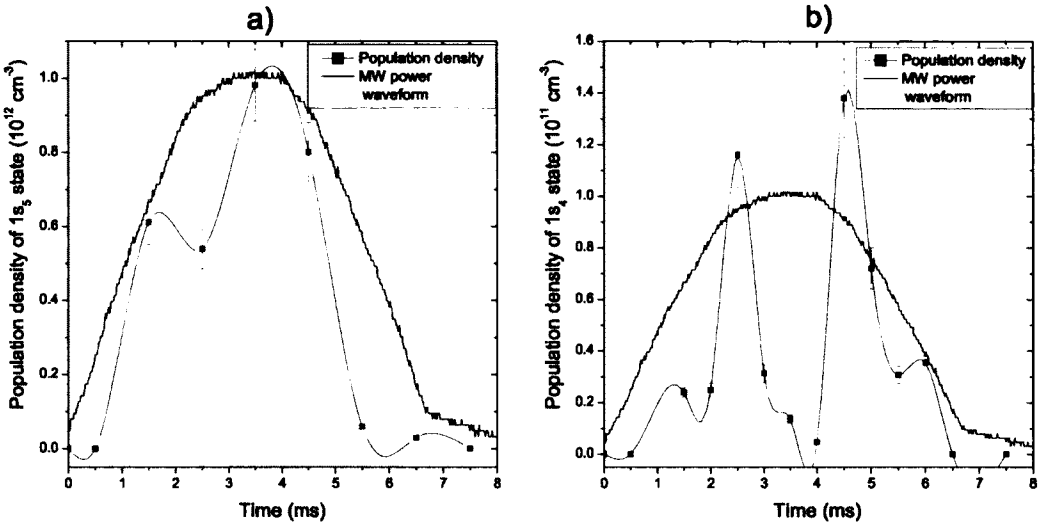

FIG. 75. Time dependence of the population densities inside the power sine signal at 2.3 Torr of the Ar I: a) metastable $1s_5$ state and b) resonant $1s_4$ state. The values obtained from the experimental results are connected with the smoothed fitted line. Experimental errors are indicated with error bars.

Time variation of population densities of these two levels are presented in Fig. 75. Experimental errors presented in the figure were estimated from the experimental errors in obtaining population densities of Ar I $2p_2$ and $2p_3$ levels and corresponding first derivatives. They are determined to be within 10%. It could be seen from the figure that both metastable and resonant states have two peaks within the power signal. It seems as if the population densities oscillate at the twice the frequency of the power signal ($f = 120$ Hz). Similar effect has already been observed in literature in the work of Macdonald *et al* [72] in the case of xenon discharge lamp.

It should be noted that the first derivatives of the Ar I $2p_2$ and $2p_3$ levels showed similar time behaviosr with and without the laser signal. This implies that their

difference can be approximated to zero as the first approximation, and the simplified case given by Eq. (154) can be applied within the 20 % approximation error.

CHAPTER 6

CONCLUSION

In this work, we have developed several methods to explain a low temperature, non-equilibrium gas discharge plasmas used to investigate surface modification processes. The discharge has been generated using microwave (MW) power. Specifically, we have obtained plasma parameters important for a complete characterization of these plasmas. Plasma processing using radio-frequency (RF) and MW power has become an essential part of surface modification processes (plasma etching and cleaning) due to the strong chemical reactivity of plasma particles and the possibility to avoid chemical disposal problems characteristic for the acid-based wet processing technologies. MW discharge plasmas represent a good candidate for environmentally friendly "green" sources for plasma etching and cleaning purposes since they allow work at higher pressures and provide higher plasma densities. Therefore, understanding physical and chemical phenomena that describe these plasmas is required. This includes developing kinetic models for all particles in the discharge (electrons, atoms, molecules, and ions) and obtaining important plasma parameters (gas densities and temperatures, electron densities and temperatures, population densities of excited atoms/molecules, etc).

Plasma parameters were obtained in two different gas discharges operating at pressure range of 1-20 Torr: supersonic flowing MW discharge in argon at frequency $f = 2.45$ GHz and pulse repetitive MW discharge in air at $f = 9.5$ GHz. Optical emission spectroscopy was used to analyze the molecular structure of these plasmas by observing molecular bands of N_2 ($C^3\Pi_u \rightarrow B^3\Pi_g$) Second Positive System (SPS) at 337.1 nm. We have evaluated rotational temperature by comparison between numerically generated synthetic and experimentally obtained rotational spectra of N_2 ($C^3\Pi_u \rightarrow B^3\Pi_g$) vibrational sequence $\Delta v = 2$ from the R_2 branch in pulse repetitive air discharge. The results stood in good agreement with rotational temperature determined from the slope of the Boltzmann distribution. We have revealed that rotational temperature decreases with the pressure increase. Similarly, by observing vibrational spectrum of $\Delta v = 2$ sequence of N_2 ($C^3\Pi_u \rightarrow B^3\Pi_g$), we have determined vibrational temperature and confirmed the Boltzmann distribution of the vibrational

levels. By assuming that the rotational temperature is equal to the gas kinetic temperature, we have been able to calculate ground state populations from the ideal gas equation in pulse repetitive discharge in air. We have found that ground state population densities increased by more than a factor of two when the pressure increased from 10 to 20 Torr, which was expected almost intuitively, even though the gas temperature could perturb this trend.

Time-resolved population densities of the N_2 ($C^3\Pi_u$) state in pulse repetitive air discharge and Ar I $4p$ levels in supersonic flowing argon discharge have been obtained by employing time synchronization device. Population densities of both N_2 ($C^3\Pi_u$) and Ar I $4p$ states vary in time in a similar way. During the discharge breakdown, these population densities peak in their values. After the breakdown, both supersonic argon and pulse repetitive air discharge become quasi-stationary characterized with nearly constant population densities.

In the case of supersonic flowing discharge, time-averaged, spatially-resolved diagnostics was possible by applying two dimensional plasma tomography methods. Several different approaches (Abel inversion, two path method based on measurements at two mutually perpendicular angles, 2D Radon inverse integration) based on plasma tomography methods have been developed and tested in this work. It was found that 2D inverse Radon integration employing filtered back projection technique with Shepp-Logan filter provides the best reconstruction of the internal plasma structure in both cases, qualitatively and quantitatively. Optical emission spectroscopy measurements have been performed by employing an automated measurement system (AMS). The AMS was built to streamline the measurements and to increase the overall precision. The system controls the angle and distance within sub-degree and sub-milimeter angle and distance precision, respectively. Spatially resolved population densities of Ar I $4p$ levels were evaluated at several positions in the afterglow region of the Ar discharge. It was found that the excited species are mainly concentrated close to the inner surface of the quartz tube implying that the discharge is partially sustained with the surface wave. We have also determined spatial distributions of the electron excitation temperatures in the discharge afterglow region by assuming Boltzmann distribution of the Ar I spectra. The excitation temperatures were obtained from the exponential fit of the spectral line intensities versus threshold excitation energies. It appeared that electron excitation temperature values were in contrast to the population distributions. This contrast reflects the complex dynamics

and the structure of the surface wave discharge.

Measuring the time-resolved waveforms of the forward and reflected power signal in the pulse repetitive air discharge allowed us to determine the time variation of the reduced electric field and, consequently, the electron temperature. Both, reduced electric field and electron temperature changed with time in a similar way as population distributions of the N_2 ($C^3\Pi_u$) and Ar I $4p$ levels. They peaked in their values during and immediately after the discharge breakdown and were characterized with almost constant values for the rest of the discharge duration.

We have developed a simple but accurate kinetic model based on the analysis of molecular bands of N_2 ($C^3\Pi_u \rightarrow B^3\Pi_g$) Second Positive System to obtain time-resolved electron densities in pulse repetitive air discharge. It was found that electron density decreased sharply with pressure increase. This increase was expected since the number density of ground state has increased by more than a factor of two while the electric field remained the same when the pressure increased. These electron densities were compared with the electron densities obtained using Stark broadening approach in previous experiments performed under same conditions. It has been found that they were in fair agreement.

By employing the laser induced fluorescence (LIF) technique and the kinetic model based on the analysis of population density rates of Ar I p states, we were able to obtain time-resolved population densities of Ar I metastable $1s_5$ and resonant $1s_4$ levels. For the purpose of LIF measurements, we have built a tunable dye laser that operates in infrared region and is pumped by a pulsed NdYag laser operating at 532 nm. The pump laser was synchronized with the power supply and the detection system using the synchronization device providing the time-resolved measurements on a microsecond time scale. It was determined that population densities of Ar I metastable $1s_5$ and resonant $1s_4$ levels oscillate with the doubled frequency of the power signal, which was indicated with two peak values within the power signal.

We have also described various approaches for obtaining electron energy distribution functions (EEDF) and electron energy probability functions (EEPF) in moderate (Maxwell-Boltzmann, Druyvesteyn, two parameter, and two term approach) and strong electric fields. Comparison between these approaches in moderate electric fields showed that the two term approach provides the most general solution of Boltzmann equation. However, two term approach is not valid for high values of reduced electric field when most collisions are inelastic and EEDF becomes strongly

anisotropic. These conditions are characteristic for the breakdown of the microwave discharge, implying that during this time, the EEDF can not be determined by employing the two term approach. Therefore, evaluation of EEDF at the inception of the MW discharge is an important task for future work. In addition, we have determined rate coefficients for electrical impact collisions by solving numerically the integral based on the product of the cross-sections and distribution functions of colliding particles. Also, we have discussed different methods developed in literature for obtaining collisional deactivation rate coefficients based on rate coefficients' dependence on gas kinetic temperature.

To conclude, we have provided a full characterization of low temperature, non-equilibrium MW discharge plasmas by developing detailed kinetic models of plasma particles, developing and applying non-intrusive, *in situ* diagnostic techniques (laser induced fluorescence and plasma tomography) for obtaining crucial plasma parameters (gas densities and temperatures, electron densities and temperatures, excitation temperatures, rotational and vibrational temperatures, and population densities of excited atoms and molecules) and describing their time and spatial distributions. These promising results allow us to introduce the developed models and diagnostic techniques (plasma tomography, LIF) to investigate RF and MW discharges sustained inside the SRF niobium cavities currently employed for plasma etching and cleaning purposes in our lab.

BIBLIOGRAPHY

[1] J. Freidberg, *Plasma Physics and Fusion Energy* (Cambridge University Press, 2007).

[2] D. B. Graves, AIChE **35**, 1 (1989).

[3] J. W. Coburn, Plasma Chem. Plasma Process. **2**, 1 (1982).

[4] D. M. Manos and D. L. Flamm, *Plasma Etching: An Introduction* (Academic Press, New York, 1989).

[5] M. Konuma, *Film Deposition by Plasma Techniques* (Springer, New York, 1992).

[6] M. A. Liebermann and A. J. Lichtenberg, *Principles of Plasma Discharges and Marterials Processing* (Academic Press, New York, 1994).

[7] M. A. Liebermann and R. A. Gottscho, *Design of High Density Plasma Sources for Materials Processing* (Wiley, New York, 1994).

[8] Y. P. Raizer, *Gas Discharge Physics* (Springer Verlag, Berlin, 1991).

[9] G. J. M. Hagelaar and L. C. Pitchford, Plasma Sources Sci. Technol. **14**, 722 (2005).

[10] J. Boffard, B. Chiaro, T. Weber, and C. C. Lin, At. Data and Nucl. Data Tables **93**, 831 (2007).

[11] J. Boffard, R. O. Jung, C. C. Lin, and A. E. Wendt, Plasma Sources Sci. Technol. **19**, 065001 (2010).

[12] V. M. Donnelly, J. Phys. D: Appl. Phys. **37**, R217 (2004).

[13] H. Amemiya and M. Maeda, Rev. Sci. Instrum. **67**, 769 (1996).

[14] R. Alvarez, A. Rodero, and M. Quintero, Spectrochim. B **57**, 1665 (2002).

[15] J. Radon, IEEE Trans. Med. Imag. **5**, 170 (1986), translated by P.C. Parks from the original German text.

[16] M. P. Freeman and S. Katz, J. Phys. E: Sci. Intrum. **10**, 727 (1977).

[17] M. G. Lapworth and L. A. Allnutt, J. Opt. Soc. Am. **53**, 1172 (1963).

[18] H. Griem, *Plasma Spectroscopy* (McGraw-Hill, New York, 1964).

[19] A. Bogaerts, E. Neyts, R. Gijbels, and J. van der Mullen, Spectrochem. Acta Part B **57**, 609 (2002).

[20] A. V. Phelps and L. C. Pitchford, Phys. Rev. A **31**, 2932 (1985).

[21] B. P. Marinković, V. Pejčev, D. M. Filipović, and L. Vušković, J. Phys. B: At. Mol. Opt. Phys. **24**, 1817 (1991).

[22] A. Chutijan and D. C. Cartwright, Phys. Rev. A **23**, 2178 (1981).

[23] D. M. Filipović, B. P. Marinković, V. Pejčev, and L. Vušković, J. Phys. B: At. Mol. Opt. Phys. **33**, 677 (2000).

[24] D. H. Madison, C. M. Maloney, and J. B. Wang, J. Phys. B: At. Mol. Opt. Phys. **31**, 4833 (1998).

[25] A. Dasgupta, M. Blaha, and J. L. Guiliani, Phys. Rev. A **61**, 012703 (1999).

[26] M. Druyvesteyn and F. Penning, Rev. of Modern Phys. **12**, 947 (1940).

[27] A. V. Gurevich, N. Borisov, and G. M. Milikh, *Physics of Microwave Discharges* (Gordon and Breach, Amsterdam, 1997).

[28] R. S. F. Chang and D. W. Setser, J. Chem. Phys. **69**, 3885 (1978).

[29] X. M. Zhu, a. N. B. Y. K. Pu, and R. Boswell, J. Phys. D: Appl. Phys. **42**, 142003 (2009).

[30] X. M. Zhu and Y. K. Pu, J. Phys. D: Appl. Phys. **43**, 015204 (2010).

[31] B. Brocklehurst and F. A. Downing, J. Chem. Phys. **46**, 976 (1967).

[32] V. A. Godyak, R. B. Piejak, and B. M. Alexandrovich, Plasma Sources Sci. Technol. **11**, 525 (2002).

[33] J. Jackson, *Classical Electrodynamics 3rd Edition* (Wiley, New York, 1999).

[34] H. W. Hayt, *Engineering Electromagnetics* (McGraw-Hill, New York, 1989).

[35] D. B. Atkinson and M. A. Smith, Rev. Sci. Instrum. **66**, 4434 (1995).

[36] J. D. Anderson, *Modern Compressible Flow with Historical Perspective* (McGraw-Hill, New York, 2004).

[37] B. Bachmann, R. Kozakov, G. Gott, K. Ekkert, J.-P. Bachmann, J.-L. Marques, H. Schopp, D. Uhrlandt, and J. Schein, J. Phys. D: Appl. Phys. **46**, 125203 (2013).

[38] F. P. Schafer, *Principles of dye laser operation, 3rd edition* (Springer Verlag, Berlin, 1990).

[39] F. J. Duarte, *Dye Laser Principles: with applications* (Academic Press, New York, 1990).

[40] M. G. Littman and H. J. Metcalf, Appl. Opt. **17**, 2224 (1978).

[41] R. J. Exton, R. J. Balla, G. C. Herring, S. Popović, and L.Vušković (AIAA Paper, 2003).

[42] G. C. Herring and S. Popović, Appl. Phys. Lett. **92**, 131501 (2003).

[43] V. V. Pikalov, *Plasma Tomography* (Nauka, Novosibirsk, 1995).

[44] M. J. Lighthill, *Introduction to Fourier Analysis and Generalised Functions* (Cambridge University Press, 1958).

[45] D. C. Solomon, K. T. Smith, and S. L. Wagner (Bull. Am. Math. Soc, 1977).

[46] G. E. Shilov, *Mathematical Analysis* (Nauka, Moscow, 1965).

[47] A. Rosenfeld and A. C. Kak, *Digital Picture Processing* (Academic Press, New York, 1982).

[48] A. Shepp and B. F. Logan, IEEE. Trans. Nucl. Sci. **NS-21**, 21 (1974).

[49] A. C. Eckbreth, *Laser Diagnostics for Combustion Temperature and Species* (Abacus Press, Massachusets, 1988).

[50] R. Loudon, *The Quantum Theory of Light* (University Press, Oxford, 2000).

[51] G. Herzberg, *Atomic Spectra and Atomic Structure* (Dover Publications, New York, 1944).

[52] G. A. Hebner, J. Appl. Phys. **80**, 2624 (1996).

[53] N. Beverini, G. Cicconi, G. L. Genovesi, and E. Piano, Plasma Sources Sci. Technol. **6**, 185 (1997).

[54] A. Bogaerts and R. Gijbels, Phys. Rev. A **52**, 3743 (1995).

[55] M. W. Kiehlbauch and D. B. Graves, J. Appl. Phys. **91**, 3539 (2002).

[56] J. B. Boffard, C. C. Lin, and C. A. De Joseph Jr., J. Phys. D: Appl. Phys. **37**, R143 (2004).

[57] D. Mariotti, Y. Shimizu, T. Sasaki, and N. Koshizaki, Appl. Phys. Lett. **89**, 201502 (2006).

[58] J. H. Kim, Y. H. Choi, and Y. S. Hwang, Phys. Plasmas **13**, 093501 (2006).

[59] X. M. Zhu, Y. D. Pu, Z. G. Guo, and Y. K. Pu, Phys. Plasmas **13**, 123501 (2006).

[60] S. D. Popa, J. Phys. D: Appl. Phys. **29**, 416 (1996).

[61] F. Cramarossa, G. Ferraro, and E. Molinari, J. Quant. Spectrosc. Radiat. Transfer. **14**, 419 (1974).

[62] S. V. Pancheshnuyi, S. M. Starikovskaia, and A. Y. Starikovskii, J. Phys. D: Appl. Phys. **32**, 2219 (1999).

[63] A. Plain and A. Ricard, Phys. Lett. **95A**, 235 (1983).

[64] A. N. Goyette, J. R. Peck, L. W. Anderson, and J. E. Lawler, J. Phys. D: Appl. Phys. **31**, 1556 (1998).

[65] G. Herzberg, *Molecular spectra and Molecular Structure I: Spectra of Diatomic Molecules* (Van Nordstrand, New York, 1950).

[66] G. Hartmann and P. Johnson, J. Phys. B: Atom. Molec. Phys. **11**, 1597 (1978).

[67] W. Demtroder, *Laser Spectroscopy: Basic Concepts and Instrumentation* (Springer-Verlag, Berlin, 1996).

[68] D. J. Drake, S. Popović, and L. Vušković, J. Appl. Phys. **104**, 063305 (2008).

[69] V. Guerra, P. A. Sa, and J. Loureiro, Eur. Phys. J. - Appl. Phys. **28**, 125 (2004).

[70] N. U. Rehman, M. A. N. F. U. Khan, and M. Zakaullah, Plasma Sources Sci. Technol. **17**, 025005 (2008).

[71] M. Capitelli and M. Dilonardo, Rev. Phys. Appl. **13**, 115 (1978).

[72] N. A. MacDonald, M. A. Cappelli, and W. A. Hargus Jr., Rev. Sci. Instrum. **83**, 113506 (2012).

APPENDIX A

CONVERSION OF PHYSICAL UNITS

Every quantity with the physical dimension is defined by the physical unit that describes it. Values of dimensionless quantities are expressed by pure numbers. Although there exists an internationally recommended unit data base called International System of Units, it is often useful to employ different physical units convenient for specific research area.

In atomic and plasma physics, for example, it is more convenient to express energy in units of electron volts (eV) than Joules (J) with the conversion factor

$$1 \text{ eV} = 1.6 \times 10^{-19} \text{ J}, \tag{210}$$

which represents the amount of energy gained (or lost) by the charge of a single electron moved across an electric potential difference of one volt. Furthermore, since the energy is related to the wavelength of the photon, it can be expressed in the units of wavelength (nm)

$$E = \frac{hc}{\lambda}, \tag{211}$$

where $h = 4.1 \cdot 10^{-15}$ eV·s is the Planck constant and $c = 3 \cdot 10^{8}$ m/s is the speed of light. Hence,

$$E(\text{eV}) = \frac{1239(\text{eV} \cdot \text{nm})}{\lambda(\text{nm})}. \tag{212}$$

This implies that energy of 1 eV corresponds to wavelength of ~1240 nm,

$$E = 1 \text{ eV} \Longrightarrow \lambda \cong 1240 \text{ nm}. \tag{213}$$

When describing transitions between energy levels in atoms/molecules it is common to use units of cm^{-1} instead of eV described as

$$E = 1 \text{ eV} \Longrightarrow \frac{1}{\lambda} = 8065.43 \text{ cm}^{-1}. \tag{214}$$

It should be noted that, in plasma physics, temperature, T, is also often given in electron volts not in kelvin (K). The conversion to kelvin is defined by using the Boltzmann constant $k = 1.38 \cdot 10^{-23}$ J/K $= 8.6 \cdot 10^{-5}$ eV/K as

$$E = kT. \tag{215}$$

Thus

$$E(\text{eV}) = 8.6 \cdot 10^{-5}(\text{eV/K}) \cdot T(\text{K}), \tag{216}$$

implying that energy of 1 eV corresponds to 11604 K,

$$E = 1 \text{ eV} \Longrightarrow T = 11604 \text{ K}. \tag{217}$$

Conversion units discussed above are summarized in Table 12.

TABLE 12. Conversion table for energy units.

Physical units				
eV	J	nm	cm^{-1}	K
1	$1.6 \cdot 10^{-19}$	1240	8065.43	11604

In this work we also expressed pressure in units of Torr rather than Pascals (Pa). Torr is related to Pascal as

$$1 \text{ Torr} = 133.3 \text{ Pa}. \tag{218}$$

In addition, reduced electric field E/N_n is given in units of Townsend (Td) with conversion factor

$$1 \text{ Td} = 10^{-17} \text{ Vcm}^2. \tag{219}$$

APPENDIX B

NUMERICAL CODES

B.1 PLASMA TOMOGRAPHY

Numerical codes for calculating direct and inverse Abel transform and direct and inverse Radon transform described in Section 4.1 are presented bellow. In the case of inverse Radon transform, we have shown both direct integration and filtered back projection method. We have employed previously developed subroutines for numerical integration and derivation together with the subroutines for the data fitting (Lagrange interpolation and spline fitting) and these codes are excluded from the presented work.

B.1.1 ABEL TRANSFORM CODES

```
!*****************************************************************
module physics
  integer, parameter :: nint=21    ! number of abel integrals
  double precision xval(nint+1), f(nint+1)
  double precision yint(nint+1), xint(nint+1)
  double precision a
end module physics
!*****************************************************************

program integal
!=============================================================================================
! Direct Abel Integral
!
! Milka Nikolic    June 2013
!
! input
! Distribution function Er(r)
! output
! Intensities on different radial positions, I(r)
!=============================================================================================
use physics

implicit none

integer k,  nofun
double precision rmin, rmax, r, gauss16
double precision step, e
double precision Er1
double precision abserr, relerr, errest, flag

double precision, parameter :: pi = 3.1415926
parameter (abserr=0.0, relerr=1.0e-16)
external e
```

```
!-------------------------
!reads data from file
!-------------------------
open (unit=7, file= 'xinverse.dat')
open (unit=8, file= 'yinverse.dat')
open (unit=10, file= 'xvalues.dat')
open (unit=11, file= 'yvalues.dat')


do k=1,nint
        read (7,100) xval(k)
        read (8,100) f(k)
end do

do k=1,nint                                          !writes data into file
        write(*,*) xval(k), f(k)
end do

!-------------------------------------------
!evaluate integral
!-------------------------------------------
rmin = 0.0
rmax = 1.6

step = (rmax-rmin)/dfloat(nint-1)

do k=1,nint
        a=rmin+step*dfloat(k-1)
        r = a

        !Er1 = gauss16(e, r, rmax+0.00001)
    call quanc8(e,r+0.00000000000001,rmax+0.000000000000001,abserr,relerr,Er1,errest,nofun,flag)

    yint(k) = 2.0*Er1
        xint(k) = r
end do

do k=1,nint
        write(10,100) xint(k)        ! intensities for the integral
    write(11,100) yint(k)
end do

100   format(f15.4)
end program integal


function e(x)
!================================================
!emissivity
!================================================
use physics
implicit none
double precision x, e, lagint
        e = lagint(x, xval, f, nint, 3)*x/(sqrt(x-a)*sqrt(x+a))
end function e


!*****************************************************************
module physics
  integer, parameter:: n=22
      !size of an array, number of data points
  integer, parameter :: nd=200 ! number of points where derivatives to be calc.
  integer, parameter :: ni=21    ! number of abel inverted integrals
  double precision y(n), xval(n), dy(nd), dx(nd), yint(ni), xint(ni), yr(ni), xr(ni)
  double precision a
end module physics
!*****************************************************************
```

```
program integal
!=============================================================================================================
! Inverse Abel Integral
!
! Milka Nikolic    June 2013
!
! input
! Intensities on different radial positions, I(r)
! output
! Distribution function Er(r)
!=============================================================================================================
use physics

implicit none

integer k,nsimp, j,  nofun
double precision rmin, rmax, r, g, gauss16
double precision step, x, deriv4, deriv3
double precision Er1
double precision abserr, relerr, errest, flag

double precision, parameter :: pi = 3.1415926
parameter (abserr=0.0, relerr=1.0e-16)
external g

!-------------------------
!reads data from file
!-------------------------
open (unit=7, file='xvalues.dat')
open (unit=8, file= 'yvalues.dat')
open (unit=9, file= 'derivative.dat')
open (unit=10, file= 'integral.dat')

do k=1,n-1
        read (7,100) xval(k)
        read (8,100) y(k)
end do

do k=1,n-1                                          !writes data into file
        write(*,*) xval(k), y(k)
end do

100   format(f15.4)

rmin = xval(1)
rmax = xval(n-1)

!=======================================================
! calculates the first derivatives
!=======================================================
step = (rmax-rmin)/dfloat(nd-1)

do k=1,nd
        x = rmin + step*float(k-1)
        !dy(k) = deriv4(x, xval, y, n-1, 5, 1)
    dy(k) = deriv3(x, xval, y, n-1, 1)    !perfect for test functions
        dx(k) = x
    write(*,*) dy(k)
end do


do k=1, nd
        write(9,200) dx(k), dy(k)        ! intensities for the first derivative
end do

200   format(2f15.4)
```

```
rmin = xval(1)          !to avoid divergency
rmax = xval(n-1)

step = (rmax-rmin)/dfloat(ni-1)

do k=1,ni
        a=rmin+step*dfloat(k-1)
        r = a
    nsimp = 2
        !Er1 = gauss16(g, r, rmax+0.001)

    !do j=1,16
    !call simpson(g,r+0.001,rmax+0.001,Er1,n)
    !write(*,*) nsimp, Er1
    !nsimp = nsimp*2
    !end do

    call quanc8(g,r+0.1,rmax+0.1,abserr,relerr,Er1,errest,nofun,flag)
    yint(k) = (-1.0)*Er1/pi
        xint(k) = r
end do

do k=1,ni
        write(10,100) yint(k)        ! intensities for the integral
end do


end program integal


function g(x)
!================================================
!emissivity
!================================================
use physics
implicit none
double precision x, g, lagint
        g = lagint(x, dx, dy, nd-1, 3)/(sqrt(x-a)*sqrt(x+a))
end function g
```

B.1.2 DIRECT RADON TRANSFORM CODE

```
!*****************************************************************************************************
module physics
  integer, parameter:: ng=161     !size of an matrix, number of emisivity data points
  integer, parameter:: ntheta=21  !number of angles to be produced
  integer, parameter:: np=17      !number of measured distance points = number of p points
  integer, parameter:: ns=601

  double precision g(ng,ng), theta(100), p(np), s(ns), si(ns), gi(ns), Emis(ns,ns), Emistest(ns,ns), st
  double precision b(ns), c(ns), d(ns)
  integer tmax

  double precision, parameter :: pi = 3.1415926

end module physics
!*****************************************************************************************************

program directradon
!=====================================================================================================
! Direct Radon Integral for 2D Plasma Tomography
!
```

```
! Milka Nikolic    June 2013
!
!input
! Distribution function Emis(x,y)
! output
! Intensities on different positions and under different angles, I(p,theta)
!=============================================================================================
use physics

implicit none

integer i, j, k
integer m, l, t, nofun
integer mtest, ltest, swap
double precision thetamin, thetamax, dtheta
double precision R, xmin, xmax, dp
double precision smin, smax, ds
double precision xi, yi, dx
double precision value
double precision abserr, relerr, errest, flag, Er1
double precision sitest, gitest
integer test

double precision e
external e

parameter (abserr=0.0, relerr=1.0e-16)

!============
!file names
!============
open (unit=7, file= 'radoninverse.dat')
open (unit=8, file= 'testg.dat')
open (unit=9, file= 'variables.dat')
open (unit=10, file= 'directradon.dat')
open (unit=11, file= 'sampling.dat')
open (unit=12, file= 'theta.dat')
open (unit=13, file= 'variablescheck.dat')
open (unit=14, file= 'integraltest.dat')
open (unit=15, file= 'differences.dat')


!====================
!reads data from file
!====================
do i=1,ng
        read(7,*) (g(i,j), j=1,ng)        ! emisivities for the integral
end do


do i=1,ng                                       ! test writes data into file
        write(8,101) (g(i,j), j=1,ng)
end do


100 format(161(f8.4))
101 format(161(f8.4))


!====================
! variable dimensions
!====================
R = 1.6
xmin = -1.6
xmax = 1.6
dx = (xmax-xmin)/real(ng-1)
dx = int(dx*1000.0)/1000.0
```

```
thetamin = 60*pi/180.0
thetamax = 150*pi/180.0
dtheta = (thetamax-thetamin)/(ntheta-1)

dp = (xmax-xmin)/real(np-1)


!==============================
! evaluate direct radon integral
!==============================
do i=1,ntheta
  theta(i) = thetamin + dtheta*real(i-1)
  write(*,300) theta(i)*180.0/pi
  write(11,300) theta(i)*180.0/pi

  do j=1,np
    if(theta(i)==0.0 .or. theta(i)==pi) then
      p(j) = (-1)*(xmin + dp*real(j-1))
      smin = -R
      smax = R
    else
      p(j) = (-1)*(xmin + dp*real(j-1))
      smin = -(R**2.0-p(j)**2)**0.5
      smax = (R**2.0-p(j)**2)**0.5
    end if

         write(9,310) p(j)

    ds = (smax-smin)/real(ns-1)

    t = 0
    mtest = 0
    ltest = 0

        write(11,310) p(j)

    do k=1,ng

      xi = xmin + dx*(k-1)

      if(theta(i)==90.0*pi/180.0) then
        yi = p(j)
      else
        yi = xi*tan(theta(i)) - p(j)/cos(theta(i))
      end if

      write(9,320) xi, yi, nint(xi/dx)*1.0, -(int(xi/dx)*dx-xi),
                                xi/dx,nint(yi/dx)*1.0, yi/dx, int(yi/dx)*dx-yi

      if((nint(yi/dx)*dx-yi)**2<0.0005 .and. yi.le.xmax .and. yi.ge.xmin)then
        l = k
        m = nint((yi-xmin)/dx) + 1

                if(m.eq.mtest .and. l.eq.ltest) then
                write(*,*) m, l, theta(i)*180.0/pi, p(j)
        else
                        if(theta(i)==90.0*pi/180.0) then
                        st = xi
                value = g(m,l)
                else
                        st = xi*cos(theta(i)) + yi*sin(theta(i))
                value = g(l,m)
            end if
       if(st.le.smax .and. st.ge.smin) then
```

```
                t = t+1
                 si(t) = st !s(k)
            gi(t) = value
            tmax = t
        write(11,*) l,m,t, xi, yi, g(l,m)

    end if
    end if


    write(9,330) xi, yi
    mtest = m
    ltest = l
  end if
  tmax = t
end do      !ends s loop

!================================
!checks the sampling of the points
    !================================
do k=1,ng
  xi = xmin + dx*(k-1)
  yi = xi*tan(theta(i)) + p(j)/cos(theta(i))

  if((nint(yi/dx)*dx-yi)**2<0.00001) then
    write(13,330) xi, yi
  end if
end do

      !==========================
!sorts si(t) in rising order
!==========================
swap = 1
do while (swap==1)
  swap = 0
  do k=1,tmax-1
    if(si(k).gt.si(k+1)) then
      sitest = si(k+1)
      si(k+1) = si(k)
      si(k) = sitest

      gitest = gi(k+1)
      gi(k+1) = gi(k)
      gi(k) = gitest

      swap = 1
    end if

  end do
end do


    if(tmax .gt. 2) then    !checks if there is enugh points to calculate integral
!=========================================
!calls spline to calculate spline coeficients
!=========================================
     call spline (si, gi, b, c, d, tmax)

!====================
!calls quanc8 integral
!====================
call quanc8(e,smin,smax,abserr,relerr,Er1,errest,nofun,flag)
Emis(j,i) = Er1

do t=1,tmax
  si(t) = 0.0
  gi(t) = 0.0
```

```
    end do
    else
      Emis(j,i) = 0.0
      write(*,*) tmax
    end if

    !============================
    !tests integral for g = x*x+y*y
        !============================
    Emistest(j,i) = (2*smax**3)/3 + 2*smax*p(j)**2
    !Emistest(j,i) = sqrt(pi)*exp(-p(j)**2)

  end do     !ends p loop
end do       !ends theta loop

do j=1,np
        write(10,400) (Emis(j,i), i=1,ntheta)            ! line intensities to use in inverse radon
    write(14,400) (Emistest(j,i), i=1,ntheta)        ! test of integral
    !write(15,400) (((Emistest(j,i)-Emis(j,i))*100)/Emistest(j,i), i=1,ntheta)
end do

do j=1,ntheta
        write(12,500) theta(j)        ! theta values to use in inverse radon
end do


200 format(4(f10.4))
300 format('theta =', f10.6)
310 format('p =',f10.4)
320 format(8(f10.6))
330 format('xi =', f10.4, 'yi =', f10.4)
400 format(100(f10.4))
500 format(f10.4)

end program directradon

function e(x)
!============================
!function for e(x) integral
!============================
use physics
implicit none
double precision x, e, lagint, ispline
        e = ispline(x, si, gi, b, c, d, tmax)
        !e = lagint(x, si, gi, tmax, 3)
end function e
```

B.1.3 INVERSE RADON TRANSFORM CODE - DIRECT INTEGRATION

```
!*****************************************************************************************************
module physics
  integer, parameter:: ntheta=21   !number of angles
  integer, parameter:: np=17       !number of measured distance points = number of p points
  integer, parameter:: nx=51      !number of x and y points produced in the integral

  double precision fs(np,ntheta), theta(ntheta), gi(np), p(np), Er(ntheta), m(nx,nx), mtest(nx,nx)
  double precision gitest(np), ptest(np)
  double precision b(100), c(100), d(100)
  double precision p0

  double precision, parameter :: pi = 3.1415926
end module physics
```

```
!*****************************************************************************************************************

program radon
!=================================================================================================
! Inverse Radon Integral for 2D Plasma Tomography -direct integration
!
! Milka Nikolic    June 2013
!
!input
! Intensities on different positions and under different angles, I(p,theta)
! output
! Distribution function g(x,y)
!=================================================================================================
use physics

implicit none

integer i, j, k, l
integer nofun, swap

double precision xmin, xmax, dp
double precision dx, xi, yi
double precision rcal, thetamin, thetamax
double precision abserr, relerr, errest, flag, Em, Er1, Er2, Er3, deriv3
double precision ptest1, gitest1, deriv4
double precision min, proba

double precision g, e
external e
external g

parameter (abserr=0.0, relerr=1.0e-16)


!-------------------------------------------------------------
!file names
!-------------------------------------------------------------
open (unit=7, file= 'directradon.dat')
open (unit=8, file= 'theta.dat')
open (unit=9, file= 'test.dat')
open (unit=10, file= 'nversecalc.dat')
open (unit=11, file= 'nversecalctest.dat')

!---------------------------------
!reads data from file
!---------------------------------
do i=1,np
        read(7,*) (fs(i,j), j=1,ntheta)        ! direct radon intensities for the integral
end do

do i=1,ntheta
        read(8,200) theta(i)
end do

do i=1,np                                       !writes data into file
        write(9,300) (fs(i,j), j=1,ntheta)
end do

do i=1,ntheta
        write(*,*) theta(i)
end do

100 format(50(f8.4))
200 format(f15.4)
300 format(50(f10.4))

!====================
```

```
! variable dimensions
!=====================
xmin = -1.6
xmax = 1.6
dx = (xmax-xmin)/real(nx-1)
dp = (xmax-xmin)/real(np-1)

thetamin = theta(1)
thetamax = theta(ntheta)

proba = 0.00001

!================================
! evaluate inverse radon integral
!================================
do i=1,nx
          xi = xmin+dx*(i-1)
        do j=1, nx
               yi = xmin+dx*(j-1)
        do k=1,ntheta
                  do l=1,np
                              gi(l) = fs(l,k)
                p(l) = (-1)*(xmin + dp*real(l-1))!*sin(theta(k))
                  end do   !ends p loop (in l)

                        !=========================
            !puts p(j) in reverse order
            !=========================
            !do l=1,np
                        !        gitest(l) = gi(np+1-l)
                            !        ptest(l) = p(np+1-l)
                !write(*,*) p(l)
                  !end do

            !do l=1,np
                        !        gi(l) = gitest(l)
                            !        p(l) = ptest(l)
                !write(*,*) p(l)
                  !end do

            !=========================
                    !sorts p(j) in rising order
                    !=========================
                    swap = 1
                    do while (swap==1)
                              swap = 0
                              do l=1,np-1
                                if(p(l).gt.p(l+1)) then
                                          ptest1 = p(l+1)
                                          p(l+1) = p(l)
                                          p(l) = ptest1

                                          gitest1 = gi(l+1)
                                          gi(l+1) = gi(l)
                                          gi(l) = gitest1

                                          swap = 1
                                end if
                              end do
                    end do

            !========================================
                    !calls spline to calculate spline coeficients
                    !========================================
                        call spline (p, gi, b, c, d, np)

            p0 = (-1.0)*xi*sin(theta(k))+ yi*cos(theta(k))
```

```
                    rcal = sqrt(xi*xi+yi*yi)

          min = 0.0

                    if(rcal**2.le.xmax**2) then
              call quanc8(g,proba,xmax,abserr,relerr,Er2,errest,nofun,flag)
              !call quanc8(g,xmin,xmax,abserr,relerr,Er2,errest,nofun,flag)

              Er(k) = Er2 !+ deriv4(p0, p, gi, np, 5, 1)*log(abs((xmax-p0)/(p0-xmin)))
                    else
                            Er(k) = 0.0
                    end if
       end do    !ends theta loop (in k)

       call spline (theta, Er, b, c, d, ntheta)

              call quanc8(e,thetamin,thetamax,abserr,relerr,Em,errest,nofun,flag)

       m(j,i) = (-1.0)*Em/(2*pi**2)
       !mtest(j,i) = exp(-(xi**2+yi**2))

       end do   !ends y loop (in j)
  write(*,*) i, xi
end do      !ends x loop (in i)

do i=1,nx
       write(10,400) (m(j,i), j=1,nx)        ! intensities for the integral
   !write(11,400) (abs(m(i,j)-mtest(i,j)), j=1,nx)
end do


400 format(161(f8.4))


end program radon

function g(x)
!================================================
!function for g(x,y) integral
!================================================
use physics
implicit none
double precision x, g, lagint, ispline, deriv4, deriv3, gtest
       !principal value integral
   !-------------------------
       !gtest = deriv4(x, p, gi, np, 5, 1) - deriv4(p0, p, gi, np, 5, 1)
       !g = gtest/(x-p0)

       !alex formula
   !-------------------------------------------------------------------------------
   gtest = ispline(p0-x, p, gi, b, c, d, np) + ispline(p0+x, p, gi, b, c, d, np)
            -2* ispline(p0, p, gi, b, c, d, np)
       g = gtest/x**2

   !gtest = -deriv4(p0-x, p, gi, np, 5, 1) + deriv4(p0+x, p, gi, np, 5, 1)
   !g = gtest/x

   !g = deriv3(x, p, gi, np, 1)/(x-p0)
       !g = (x+p0)**2*ispline(x, p, gi, b, c, d, np)/((x-p0)*(x+p0)*(x-p0)*(x+p0))
       !g = lagint(x, p, gi, np, 3)/((x-p0)**2)
end function g

function e(x)
!================================================
!function for e(x,y) integral in theta
!================================================
use physics
```

```
implicit none
double precision x, e, lagint, ispline
        e = ispline(x, theta, Er, b, c, d, ntheta)
        !e = lagint(x, theta, Er, ntheta, 3)
end function e
```

B.1.4 INVERSE RADON TRANSFORM CODE - FILTERED BACK PROJECTION

```
!*****************************************************************************************************
module physics
  integer, parameter:: ntheta=21   !number of angles
  integer, parameter:: np=17       !number of measured distance points = number of p points
  integer, parameter:: nx=161      !number of x and y points produced in the integral

  double precision fs(np,ntheta), theta(ntheta), Ptheta(np), Qtheta(np), p(np), gi(nx,nx), mi(nx,nx)
  double precision b(800), c(800), d(800)
  double precision p0

  double precision, parameter :: pi = 3.1415926
end module physics
!*****************************************************************************************************

program filter
!=============================================================================================
! Inverse Radon Integral for 2D Plasma Tomography -filtered back projcetion (Ram-Lak and Shepp-Logan)
!
! Milka Nikolic    June 2013
!
!input
! Intensities on different positions and under different angles, I(p,theta)
! output
! Distribution function g(x,y)
!=============================================================================================
use physics

implicit none

integer i, j, k, l, mx
integer swap!, nofun

double precision xmin, xmax, dp
double precision dx, xi, yi
double precision rcal, tau !,thetamin, thetamax
double precision ptest1, gitest1, Sum, Er
double precision m, h(2*np+2)
double precision ispline, lagint

!---------------------------------------------------------------
!file names
!---------------------------------------------------------------
open (unit=7, file= 'integraltest.dat')
open (unit=8, file= 'theta.dat')
open (unit=9, file= 'test.dat')
open (unit=10, file= '706SheppLogan.dat')
open (unit=11, file= 'analytical inverse')

!---------------------------------
!reads data from file
!---------------------------------
do i=1,np
        read(7,*) (fs(i,j), j=1,ntheta)        ! direct radon intensities for the integral
```

```
end do

do i=1,ntheta
        read(8,200) theta(i)
end do

do i=1,np                                          !writes data into file
        write(9,300) (fs(i,j), j=1,ntheta)
end do

200 format(f15.4)
300 format(200(f15.4))

!====================
! variable dimensions
!====================
xmin = -1.6
xmax = 1.6
dx = (xmax-xmin)/real(nx-1)
dp = (xmax-xmin)/real(np-1)

!thetamin = theta(1)
!thetamax = theta(ntheta)

!=================================================================
! evaluate inverse radon integral using filtered back projection
!=================================================================
do i=1,nx
          xi = xmin+dx*(i-1)
    write(*,*) i
        do j=1, nx
                yi = xmin+dx*(j-1)
                rcal = xi**2+yi**2

        gi(i,j) = 0.0
        mi(i,j) = 0.0

        if(rcal.le.xmax**2.0) then

          do k=1,ntheta     !loop in theta
            tau = dp !*sin(theta(k))
            do l=1,np
                            Ptheta(l) = fs(l,k)
                p(l) = (-1)*(xmin + dp*real(l-1))!*sin(theta(k))
              end do   !ends p loop (in l)

            !==========================
                    !sorts p(j) in rising order
                    !==========================
                    swap = 1
                    do while (swap==1)
                              swap = 0
                              do l=1,np-1
                                if(p(l).gt.p(l+1)) then
                                          ptest1 = p(l+1)
                                          p(l+1) = p(l)
                                          p(l) = ptest1

                                          gitest1 = Ptheta(l+1)
                                          Ptheta(l+1) = Ptheta(l)
                                          Ptheta(l) = gitest1

                                          swap = 1
                                end if
                              end do
                    end do
```

```
            !=======================
            !calculates projection h
                  !=======================

                        !-------------------
            !Ram Lak filter
            !-------------------
            !do l=1,np
            !  m=2*l-np
                        ! h(2*l)=-1/(m**2*pi**2*tau**2)
            !  h(2*l-1)=0.0
                        !end do
                        !h(np)= 1/(4.0*tau**2)

                        !-------------------
            !Shepp Logan filter
            !-------------------
            do l=1,2*np-1
              m=l-np
              h(l) = -2.0/(pi**2*tau**2*(4*m**2-1))
            end do
            h(np) = 2.0/(pi*tau)**2

            !============================
            !calculates Q
            !============================
            do l=np,2*np-1
               Sum=0.0
                        do mx=0,np-1
                        Qtheta(l-np+1)=Sum+Ptheta(mx+1)*h(l-mx)
                  Sum=Qtheta(l-np+1)
               end do
               Qtheta(l-np+1)=tau*Qtheta(l-np+1) !Qtheta(l-np+1)
            end do

                        p0=xi*sin(theta(k))-yi*cos(theta(k))
            call spline (p, Qtheta, b, c, d, np)

            Er = ispline(p0, p, Qtheta, b, c, d, np)
            !Er = lagint(p0, p, Qtheta, np, 3)

            gi(i,j)=gi(i,j)+Er
          end do      !ends theta loop

          gi(i,j) = pi*gi(i,j)/real(ntheta)
          mi(i,j) = exp(-(xi**2+yi**2))

       end if


    end do   !ends y loop

end do     !ends x loop

do j=1, 2*np-1
  write(*,*) j, h(j)
end do

do i=1,nx
        write(10,400) (gi(i,j), j=1,nx)
    write(11,400) (mi(i,j), j=1,nx)
end do

400 format(161(e15.4))

end program filter
```

B.2 SYNTHETIC MOLECULAR SPECTRA

Numerical code for generating synthetic molecular spectra of N_2 ($C^3\Pi_u \rightarrow B^3\Pi_g$) Second Positive System at 337.1 nm described in Section 5.1 is presented here.

```
!*****************************************************************************************************************
module constants
  double precision, parameter :: Bx = 1.9898        !in cm-1
  double precision, parameter :: h = 6.625*10.0**(-27)
  double precision, parameter :: c = 3.0*10.0**10
  double precision, parameter :: k = 1.38*10.0**(-16)
  double precision, parameter :: dopp = 7.16*10.0**(-7)/(2.0*0.83255)
  double precision, parameter :: amu = 14
  integer, parameter :: n = 101                                  !size of an array, number of data points
  integer, parameter :: npoint = 8000      !number of points
end module constants
!*****************************************************************************************************************

!*****************************************************************************************************************
module rotational
  double precision bv(2), yv(2), dv(2)         ! rotational constants
  double precision, parameter :: Lhead = 380.47  !nm
  double precision, parameter :: Trot = 1000 !rotational temp
  double precision, parameter :: a = 375.68085       !initial and final wavelength
  double precision, parameter :: b = 380.68085
  double precision, parameter :: linst = 0.02     !intrumental broadening
end module rotational
!*****************************************************************************************************************

program main
!=======================================================================
! Program for generating syntetic molecular spectra for a PI state of nitrogen
!
! Milka Nikolic    June 2013
!=======================================================================
use constants
use rotational
implicit none

integer i, j
double precision F0(2,105), F1(2,105), F2(2,105)
double precision z1(105), z2(105)
double precision P0(105), P1(105), P2(105), R0(105), R1(105), R2(105)
double precision Q1(105), Q2(105)
double precision LP0(105), LP1(105), LP2(105), LR0(105), LR1(105), LR2(105)
double precision LQ1(105), LQ2(105)
double precision FP0(105), FP1(105), FP2(105), FR0(105), FR1(105), FR2(105)
double precision FQ1(105), FQ2(105)
double precision dopP0(105), dopP1(105), dopP2(105), dopR0(105), dopR1(105), dopR2(105)
double precision dopQ1(105), dopQ2(105)

double precision Pmin, Q, QS, f, ftest(105), I(8005)
double precision intP0, intP1, intP2, intR0, intR1, intR2, intQ1, intQ2, Itest, Int(80005), Imax



!reads data into file
open (unit=7, file= 'fortrat.dat')              !reads the values of rotational consts
open (unit=8, file= 'spectra.dat')

!----------------------------
!defines rotational constants
!----------------------------
bv(1) = 1.8149
yv(1) = 21.5
```

```
dv(1) = 6.7*10.0**(-6)

bv(2) = 1.59218
yv(2) = 26.4
dv(2) = 6.7*10.0**(-6)

!------------------
! other constants
!------------------
Pmin = 100.0
QS = 0.0

!----------------------------
!calculates the terms
!----------------------------
do i=1,2
  do j=1,n
    z1(j) = yv(i)*(yv(i)-4.0)+4.0/3.0+4.0*j*(j+1)
    z2(j) = (yv(i)*(yv(i)-1)-4.0/9.0-2.0*j*(j+1))/(3.0*z1(j))

    F0(i,j) = bv(i)*(j*(j+1)-sqrt(z1(j))-2.0*z2(j))-dv(i)*(real(j)-0.5)**4.0
    F1(i,j) = bv(i)*(j*(j+1)+4.0*z2(j))-dv(i)*(real(j)+0.5)**4.0
    F2(i,j) = bv(i)*(j*(j+1)+sqrt(z1(j))-2.0*z2(j))-dv(i)*(real(j)+1.5)**4.0
  end do
end do

do j=1,n-1
   P0(j+1) = F0(1,j)-F0(2,j+1)
   P1(j+1) = F1(1,j)-F1(2,j+1)
   P2(j+1) = F2(1,j)-F2(2,j+1)

   R0(j) = F0(1,j+1)-F0(2,j)
   R1(j) = F1(1,j+1)-F1(2,j)
   R2(j) = F2(1,j+1)-F2(2,j)

   Q1(j) = F1(1,j)-F1(2,j)
   Q2(j) = F2(1,j)-F2(2,j)

   if(P2(j+1)<Pmin) then       !finds minimum
     Pmin=P2(j+1)
   end if
end do
P0(1) = 0.0
P1(1) = 0.0
P2(1) = 0.0

!----------------------------
! fortrat diagram
!----------------------------
write(7,101)
do j=1,n-1
  LP0(j) = -Lhead**2*10.0**(-7)*(P0(j)-Pmin) + Lhead
  LP1(j) = -Lhead**2*10.0**(-7)*(P1(j)-Pmin) + Lhead
  LP2(j) = -Lhead**2*10.0**(-7)*(P2(j)-Pmin) + Lhead

  LR0(j) = -Lhead**2*10.0**(-7)*(R0(j)-Pmin) + Lhead
  LR1(j) = -Lhead**2*10.0**(-7)*(R1(j)-Pmin) + Lhead
  LR2(j) = -Lhead**2*10.0**(-7)*(R2(j)-Pmin) + Lhead

  LQ1(j) = -Lhead**2*10.0**(-7)*(Q1(j)-Pmin) + Lhead
  LQ2(j) = -Lhead**2*10.0**(-7)*(Q2(j)-Pmin) + Lhead

  write(7,100) LP0(j), LP1(j), LP2(j), LR0(j), LR1(j), LR2(j), LQ1(j), LQ2(j), real(j)
end do

100  format(9f10.3)
101  format(5x, 'LP0', 7x, 'LP1', 7x, 'LP2', 7x, 'LR0', 7x, 'LR1', 7x, 'LR2', 7x, 'LQ1', 7x, 'LQ2', 7x, 'j')
```

```
!=========================
!Intensity distribution
!=========================
Q = k*Trot/(h*c*Bx)

do j=1,n-1
    f = (2*j+1)*exp(-j*(j+1)/Q)
    QS = QS+f
end do

do j=1,n-1
  ftest(j) = exp(-j*(j+1)/Q)/QS
end do

do j=1,n-1
  FP0(j) = (j+1)**2*ftest(j)/(j+1)
  FP1(j) = (j+2)*j*ftest(j)/(j+1)
  FP2(j) = (j+3)*(j-1)*ftest(j)/(j+1)

  FR0(j) = j**2*ftest(j)/j
  FR1(j) = (j+1)*(j-1)*ftest(j)/j
  FR2(j) = (j+2)*(j-2)*ftest(j)/j

  FQ1(j) = (2.0*j+1)*ftest(j)/(j*(j+1))
  FQ2(j) = (2.0*j+1)*4.0*ftest(j)/(j*(j+1))


end do

!---------------------
! Doppler effect
!---------------------
Imax = 0.0

do j=1,npoint
  l(j) = a + j*(b-a)/real(npoint)
end do

do j=1,n-1
  dopP0(j) = linst + dopp*LP0(j)*sqrt(Trot/amu)
  dopP1(j) = linst + dopp*LP1(j)*sqrt(Trot/amu)
  dopP2(j) = linst + dopp*LP2(j)*sqrt(Trot/amu)

  dopR0(j) = linst + dopp*LR0(j)*sqrt(Trot/amu)
  dopR1(j) = linst + dopp*LR1(j)*sqrt(Trot/amu)
  dopR2(j) = linst + dopp*LR2(j)*sqrt(Trot/amu)

  dopQ1(j) = linst + dopp*LQ1(j)*sqrt(Trot/amu)
  dopQ2(j) = linst + dopp*LQ2(j)*sqrt(Trot/amu)
end do
!Itest = 0.0
do j=1,npoint
  Itest = 0.0
  do i=1,n-1
    intP0 = FP0(i)*exp(-(l(j)-LP0(i))**2/(dopP0(i))**2)/dopP0(i)
    intP1 = FP1(i)*exp(-(l(j)-LP1(i))**2/(dopP1(i))**2)/dopP1(i)
    intP2 = FP2(i)*exp(-(l(j)-LP2(i))**2/(dopP2(i))**2)/dopP2(i)

    intR0 = FR0(i)*exp(-(l(j)-LR0(i))**2/(dopR0(i))**2)/dopR0(i)
    intR1 = FR1(i)*exp(-(l(j)-LR1(i))**2/(dopR1(i))**2)/dopR1(i)
    intR2 = FR2(i)*exp(-(l(j)-LR2(i))**2/(dopR2(i))**2)/dopR2(i)

    intQ1 = FQ1(i)*exp(-(l(j)-LQ1(i))**2/(dopQ1(i))**2)/dopR1(i)
    intQ2 = FQ2(i)*exp(-(l(j)-LQ2(i))**2/(dopQ2(i))**2)/dopR2(i)

    Itest = Itest + (intP0+ intP1+ intP2+ intR0+ intR1+ intR2+ intQ1+ intQ2)!*(n-i)
```

```
  end do
  Int(j) = Itest
  if(Int(j)>Imax) then
    Imax = Int(j)
  end if
end do

do j=1,npoint
  Int(j) = Int(j)/Imax
  write (8,200) l(j), Int(j)
end do

!----------------------------------------
! Comparison method - Sum of all peaks
!----------------------------------------
!for(int j=1; j<=8000; j=j+1)
!         {
!            Int[j] = Int[j]/Intmax;
!            linefile<<l[j]<<setw(12)<<Int[j]<<endl
!         }

!  for(int j=1; j<=8000; j=j+1)
!  {
!          if(Int[j]>Int[j+1] && Int[j]>Int[j-1])
!          {
!             Sum = Sum+Int[j];
!             peakcalc<<l[j]<<setw(12)<<Int[j]<<endl
!          }
!  }
!  cout<<Sum<<setw(12)<<trot<<endl

!  sigma = abs(Sum-Sumint)
!  if(sigma<=error)
!  {
!      error = sigma
!  }

200 format(2f10.4)

end program main
```

VITA

Milka Nikolić
Department of Physics
Old Dominion University
Norfolk, VA 23529

EDUCATION

Aug 2013 **Ph.D.**, Physics, Old Dominion University

May 2009 **M.S.**, Physics, Old Dominion University

Nov 2005 **B.S.**, Physics, University of Belgrade, Serbia

HONOURS AND AWARDS

2009/10 and 2011/12 University Fellowship

2009-2012 Student Travel Award - Gaseous Electronics Conference

PUBLICATIONS IN REFEREED JOURNALS

M. Nikolić, A. Samolov, F. Čučkov, S. Popović, L. Vušković, and A. Godunov, "Characterization of the Supersonic Flowing Microwave Discharge using 2D Plasma Tomography," J. Appl. Phys, **113**, 103301 (2013).

M. Nikolić, S. Popović, J. Upadhyay, L. Vušković, R. Leiweke, and B Ganguly, "On a Dielectric-Barrier and a Microwave Cavity Discharge in Synchronized Operation - Case of Helium/Oxygen Mixture," Plasma Sources Sci. Technol. **21**, 015004 (2012).

M. Nikolić, S. Popović, L. Vušković, G. C. Herring, and R. J. Exton, "Electron Density Measurements in a Pulse-Repetitive Microwave Discharge in Air," J. Appl. Phys, **110**, 113304 (2011).

S. P. Kuo, O. Tarasenko, J. Chang, S. Popović, C. Y. Chen, H. W. Fan, A. Scott, M. Lahiani, P. Alusta, D. J. Drake, and M. Nikolić, "Contribution of a portable air plasma torch to rapid blood coagulation as a method of preventing bleeding," New J. Phys. **11**, 115016 (2009).

Typeset using LaTeX.